

“On the Structure of Calciprotein Particles and Fetuin-A and their Interaction”

Von der Fakultät für Mathematik, Informatik und Naturwissenschaften der RWTH Aachen University zur Erlangung des akademischen Grades einer Doktorin der Naturwissenschaften genehmigte Dissertation

vorgelegt von

Diplom-Biophysikerin

Johanna Wald

aus Wiesbaden

Berichter: Universitätsprofessor Dr. rer. nat. Walter Richtering
 Universitätsprofessor Dr. rer. nat. Willi Jahnen-Dechent

Tag der mündlichen Prüfung: 24.10.2013

Diese Dissertation ist auf den Internetseiten der Hochschulbibliothek online verfügbar.

Die vorliegende Arbeit entstand in der Zeit von November 2009 bis Juli 2013 am Institut für Physikalische Chemie der Rheinisch-Westfälischen Technischen Hochschule Aachen.

Teile dieser Arbeit sind bereits veröffentlicht:

J. Wald, S. Wiese, T. Eckert, W. Jahnen-Dechent, W. Richtering, A. Heiss

Formation and stability kinetics of calcium phosphate–fetuin-A colloidal particles probed by time-resolved dynamic light scattering

Soft Matter 7, 2869–2874 (2011)

Reproduced by permission of The Royal Society of Chemistry.

Content

1	Introduction: State of the Scientific Knowledge and Aim of the Thesis	10
2	Theory	12
2.1	Biom mineralization	12
2.2	Fetuin-A	12
2.3	Calciprotein Particles (CPPs).....	13
3	Methods	15
3.1	Basic Principles of Scattering.....	15
3.2	Basic Principles of Light Scattering.....	16
3.3	Dynamic Light Scattering.....	18
3.3.1	Correlation Functions in Dynamic Light Scattering	18
3.3.2	Determination of Particle Size with Dynamic Light Scattering.....	19
3.3.3	Three-dimensional cross correlation Dynamic Light Scattering (3D-DLS).....	21
3.4	Basic Principles of Static Scattering.....	21
3.4.1	The Phase Problem.....	21
3.4.2	The Scattering Function.....	23
3.4.3	The Form Factor	24
3.4.4	Static Light Scattering	25
3.4.4.1	Guinier Approximation and Determination of R_G	25
3.4.5	Small Angle X-Ray Scattering.....	26
3.5	Fluorescence Correlation Spectroscopy.....	26
3.5.1	Fluorescence	27
3.5.2	Basic Principles of Fluorescence Correlation Spectroscopy- Measurements	27
3.5.3	Correlation Function	28
3.5.4	Two-Focus Fluorescence Correlation Spectroscopy (2f-FCS)	28
4	Results	30
4.1	Formation and Stability Kinetics of Calcium Phosphate–Fetuin-A colloidal Particles probed by time-resolved Dynamic Light Scattering	30
4.1.1	Introduction.....	30
4.1.2	Experimental	32
4.1.2.1	Fetuin Preparation and <i>in vitro</i> Mineralization Model.....	32
4.1.2.2	Three dimensional cross correlation Dynamic Light Scattering (3D-DLS).....	32
4.1.3	Results and Discussion	33
4.1.3.1	CPP Detection by time-resolved 3D-DLS.....	33
4.1.3.2	Modulators of CPP Ripening	35
4.1.3.3	Kinetic Analysis.....	35
4.1.4	Conclusion	37
4.2	Determination of Fetuin-A Shape and Structure	39
4.2.1	Introduction.....	39
4.2.2	Experimental	40
4.2.2.1	Common Fetuin-A Preparation	40
4.2.2.2	Enhanced Fetuin-A Preparation in order to receive absolute monomeric Fetuin-A	40
4.2.2.3	Small-Angle X-Ray Scattering Measurements and Data Processing	41

4.2.2.4	Ab Initio Shape Determination.....	41
4.2.2.5	Rigid Body Modeling	42
4.2.3	Results and Discussion	42
4.2.3.1	Small-Angle X-Ray Scattering of commonly purified Fetuin-A.....	42
4.2.3.2	Small-Angle X-Ray Scattering of Fetuin-A after enhanced Purification	44
4.2.3.3	Fetuin-A Model from Experimental SAXS Data	45
4.2.3.4	Fetuin-A in Mineral Environment.....	48
4.2.4	Conclusion	49
4.2.5	Outlook.....	50
4.3	The CPP Transition - A SAXS Study reveals Insight into Shape and structural Changes.....	51
4.3.1	Introduction.....	51
4.3.2	Experimental	52
4.3.2.1	CPP-Solution	52
4.3.2.2	Basic Requirements and Design of Micro Fluidics Cycle for Dynamic Measurements	52
4.3.2.3	Micro Fluidics	53
4.3.2.4	Synchrotron SAXS Measurements.....	54
4.3.2.5	Data Evaluation	54
4.3.2.6	Light Scattering Measurements	56
4.3.3	Results and Discussion: Time-dependent SAXS Measurements.....	56
4.3.3.1	SAXS Curves of the CPPs show time-dependent Characteristics	56
4.3.3.2	Evaluation of Scattering Curves using the <i>Size Distribution Program</i>	57
4.3.3.3	Evaluation of Scattering Curves based on IGOR Pro	63
4.3.4	Conclusion: Time-dependent SAXS Measurements.....	76
4.3.5	Results and Discussion: CPP Measurement under Flow Conditions.....	77
4.3.5.1	Scattering Pattern of the CPP-Solution under Flow	77
4.3.5.2	Analysis of Difference Scattering Patterns	78
4.3.6	Conclusion: CPP Measurement under Flow Conditions	82
4.3.7	Outlook.....	82
4.4	Dynamic Exchange of Fetuin-A with colloidal Calciprotein Particles studied by means of two-color two-focus Fluorescence Correlation Spectroscopy	84
4.4.1	Introduction.....	84
4.4.2	Results and Discussion	86
4.4.2.1	Stability of fractionated second-state CPPs in different Solutions.....	86
4.4.2.2	Temporal Stability of second-state CPPs in a native CPP(2)-Solution	88
4.4.2.3	Temporal Stability of a CPP(2)-Solution containing additional free Fetuin-A	89
4.4.2.4	Preparing a Solution for the Investigation of the Exchangeability of free and CPP-bound Fetuin-A	90
4.4.2.5	Exchange of Fetuin-A bound to the CPP-Surface with free Fetuin-A in Solution.....	92
4.4.3	Summary and Conclusion.....	94
4.4.4	Experimental Section	95

4.4.4.1	Two-Focus Fluorescence Correlation Spectroscopy (2f-FCS)	95
4.4.4.2	Three-dimensional cross correlation Dynamic Light Scattering (3D-DLS).....	96
4.4.4.3	Sample Preparation.....	96
5	Conclusions	98
5.1	Summary.....	98
5.2	Outlook	102
6	Appendix	105
6.1	CPP Preparation.....	105
6.1.1	Fetuin-A Preparation	105
6.1.2	Formation and Transformation of CPPs	105
6.2	Formation and Stability Kinetics of Calcium Phosphate–Fetuin-A colloidal Particles probed by time-resolved Dynamic Light Scattering - Supplemental	106
6.2.1	CPP Size Analysis	106
6.2.2	DLS Data	107
6.3	Determination of Fetuin-A Shape and Structure - Supplemental.....	108
6.4	Influence of X-Ray Exposure on Fetuin-A SAXS Curve.....	109
6.5	Dynamic Exchange of Fetuin-A with colloidal Calciprotein Particles studied by means of two-color two-focus Fluorescence Correlation Spectroscopy - Supplemental	109
6.5.1	Additional Studies on the Stability of fractionated second-state CPPs	109
6.5.2	Stability of the Intermediate Solutions after the single Purification Steps investigated with 3D-DLS	110
6.6	Additional FCS Studies.....	111
6.6.1	FCS Measurements of pure Fetuin-A	111
6.6.2	Fractionated second-state CPPs are not stable in Water	112
6.6.3	Two-color FCS Measurements of fractionated second-state CPPs	113
6.7	Inoculation of Inhibition Mix with CPP(2)-Solution.....	113
6.8	Evolution of pH-value during CPP Transformation	114
6.9	Development of a nanoparticle-based Test measuring overall Propensity for Calcification in Serum	115
6.10	Abbreviations	117
7	References	119
	Acknowledgements	135
	Curriculum Vitae	136

Kurzzusammenfassung

Die Stabilisierung von Kalziumphosphat durch Fetuin-A, das als Inhibitor von Weichgewebekalzifizierungen bei Wirbeltieren bekannt ist, stellt ein Modellsystem in der Biomineralisationsforschung dar. Der inhibitorische Effekt basiert auf zwei gleichzeitig ablaufenden Mechanismen der Bildung von Protein-Mineral-Komplexen. Zum einen stabilisiert Fetuin-A Prenukleationscluster, was als Bildung von *Calciprotein Monomeren (CPMs)* bezeichnet wird. Der zweite, länger bekannte Stabilisierungsmechanismus basiert auf der Bildung größerer *Calciprotein Partikel (CPPs)*, deren Morphologie sich zeitabhängig und reproduzierbar ändert. Seit ihrer Entdeckung im Jahr 2003 waren und sind die CPPs Gegenstand unterschiedlichster Forschungsprojekte. Nach ihrer Bildung sind die amorphen Fetuin-A-Mineral-Partikel (primäre CPPs) mit einem hydrodynamischen Radius von 50 - 80 nm sphärisch. Nach einer Verzögerungszeit wandeln sich die primären CPPs in ellipsoidale sekundäre CPPs um. Diese bestehen aus einem kristallinen Kern, der von einer Monolage Fetuin-A umgeben ist. Sekundäre CPPs haben einen hydrodynamischen Radius von 90 - 120 nm und sind mehrere Tage stabil.

Die Forschung auf diesem Gebiet kombiniert das Interesse von Forschern unterschiedlicher Fachdisziplinen (von Ärzten über Naturwissenschaftler bis hin zu Materialforschern). Die medizinische Relevanz ergibt sich aus der Tatsache, dass CPP-ähnliche pathologische Kalziumphosphatpartikel im Aszites von Dialysepatienten nachgewiesen werden konnten. Weiterhin deuten jüngste Studien darauf hin, dass Dialysepatienten ein reduziertes intrinsisches Vermögen besitzen, Kalzifizierungen zu verhindern, was mit einem erhöhten Morbiditäts- und Mortalitätsrisiko einhergeht. Obwohl die Relevanz des Systems für die verschiedenen Fachdisziplinen bekannt ist, sind die Mechanismen der Mineral-Stabilisierung bisher kaum verstanden.

Der Schwerpunkt der vorliegenden Arbeit liegt auf den CPPs und der Aufklärung der dreidimensionalen Struktur des nativen Fetuin-A Moleküls in Lösung. Dazu wurden insbesondere Streumethoden und Fluoreszenzkorrelationsspektroskopie (FCS) verwendet.

Mittels zeitaufgelöster dynamischer Lichtstreuung konnte der Einfluss unterschiedlicher Parameter (Temperatur, Fetuin-A-, Mineral-Konzentration) auf die Umwandlungszeit und die Radien der CPPs im ersten und zweiten Zustand geklärt werden. Die Messungen zeigten außerdem, dass Änderungen der genannten Parameter den grundlegenden Mechanismus der CPP-Bildung und -Umwandlung nicht beeinflussen. Untersuchungen des Umwandlungsprozesses mit Kleinwinkelröntgenstreuung (SAXS) deuten darauf hin, dass die Umwandlung ein kontinuierlicher Prozess ist; allerdings zeigt sich eine hohe Polydispersität der Partikel.

FCS-Messungen haben gezeigt, dass die Mineralstabilisierung durch Fetuin-A auf unterschiedlichen Gleichgewichten basiert, die sich innerhalb des Systems einstellen. Der dynamische Austausch von an sekundäre CPPs gebundenem Fetuin-A mit freiem Fetuin-A in Lösung konnte eindeutig gezeigt werden.

Die Struktur des Fetuin-A-Moleküls in Lösung wurde mittels eines speziellen SAXS-Aufbaus („BioSAXS“) untersucht, der für Messungen an biologischen Proben optimiert ist. Diese Messungen lieferten das erste 3D-Modell der Fetuin-A Struktur in Lösung.

Insgesamt tragen die Ergebnisse bzgl. der Fetuin-A- und CPP-Struktur und deren Wechselwirkung zu einem tieferen Verständnis der Mineralstabilisierung durch Fetuin-A bei.

Abstract

Calcium phosphate stabilization by fetuin-A represents a model system for biomineralization research. Fetuin-A is well known as inhibitor for soft tissue calcification in vertebrates. The inhibitory effect is based on two simultaneously occurring mechanisms of protein-mineral complex formation. On the one hand, prenucleation clusters are stabilized by fetuin-A. This process is known as formation of calciprotein monomers (CPMs). The second and longer-known stabilization mechanism is based on the formation of larger calciprotein particles (CPPs). CPPs have been object of different research since their discovery in 2003 as they exhibit a reproducible, time-dependent change in morphology. Upon formation, first-state CPPs are spherical particles consisting of an amorphous fetuin-A-mineral-phase with a hydrodynamic radius of 50 - 80 nm. After a distinct lag time, first-state (or primary) CPPs transform into second-state (or secondary) CPPs, that is ellipsoidal particles consisting of a crystalline core surrounded by a fetuin-A monolayer. Second-state CPPs exhibit a hydrodynamic radius of 90 - 120 nm and stability at least for several days.

Research in the field of the CPP-fetuin-A system combines the interests of researchers from different disciplines ranging from medical scientists via life scientists up to material scientists. The medical relevance is given by the fact, that pathological calcium phosphate colloids reminiscent of CPPs have been found in the ascites of a peritoneal dialysis patient. Furthermore, recent studies indicate that hemodialysis patients exhibit a reduced intrinsic property to inhibit calcification accompanied by a higher risk for morbidity and mortality. The mechanisms of mineral stabilization are barely understood so far although the importance of the system for various disciplines is known.

In the present work, different questions concerning the CPP-fetuin-A system were addressed using in particular scattering methods and fluorescence correlation spectroscopy (FCS). The main focus was set on the CPPs. However, a second focus laid on the elucidation of the three-dimensional structure of the native fetuin-A molecule in solution.

Time-resolved dynamic light scattering revealed the influence of different parameters (temperature, fetuin-A- and mineral concentration) on the transformation time and the CPP radii in first and second state. The measurements additionally showed that the basic mechanism of CPP formation and transformation is not influenced by changes in the mentioned conditions. Furthermore, the process of CPP transformation was addressed using synchrotron small-angle X-ray scattering (SAXS) indicating that the transition from first to second state is a continuous process rather than an abrupt change. However, those investigations revealed high polydispersity of the particles.

FCS revealed that the mechanism of mineral stabilization by fetuin-A is based on several equilibria forming in the system. The dynamic exchange of fetuin-A bound to second-state CPPs with free fetuin-A in solution could be unambiguously proven.

The structure of the fetuin-A molecule in solution was investigated using a synchrotron SAXS setup aligned for the investigation of biological samples (*'BioSAXS'*). Those measurements provided the first three-dimensional model of the fetuin-A structure in solution.

Altogether, the findings concerning the fetuin-A and CPP structure and their interaction greatly contribute to a deeper understanding of the mineral stabilization by fetuin-A.

1 Introduction: State of the Scientific Knowledge and Aim of the Thesis

Research on fetuin-A began with its discovery in fetal calf serum by K. Pedersen in 1944.¹ Since then, its structure and function have been investigated by different groups throughout the world. Nevertheless, neither its structure nor its detailed function is fully understood until today. However, substantial progress was made in the field of clarification of the fetuin-A function in the last decade.

In 2003, the generation of fetuin-A deficient mice provided evidence of fetuin-A being an inhibitor for ectopic calcification in vivo.² In the same year, Heiss et al. proposed a mechanism for the fetuin-A mediated calcification inhibition.³ By using dynamic light scattering (DLS) as well as electron microscopy, they could show that a basic principle for the calcification inhibition is the formation of colloidal particles consisting of calcium, phosphate and the fetuin-A itself. Due to the composition of the particles they were given the name *Calciprotein Particles*, commonly abbreviated as CPPs. The same publication showed that the initially amorphous CPPs change their structure towards a more crystalline, less soluble structure. Further studies revealed that the amorphous structure becomes a core-shell structure with the core consisting of octacalcium phosphate (OCP) shielded by a fetuin-A monolayer.⁴

The structural change is accompanied by a morphological change of the particles. A combined approach using DLS and electron microscopy could show that a highly anisotropic outgrowth of the initially spherical particles (primary CPPs or first-state CPPs) leads to elliptical particles in the second state (secondary CPPs or second-state CPPs).⁵ Subsequent investigations gave reason to suppose the processes of CPP formation and transformation as being reproducible and dependent on various environmental conditions, such as temperature and fetuin-A concentration.⁶ Beyond their significance in the field of fetuin-A research, CPPs were shown to have practical clinical relevance: a comparison of electron microscopy pictures of secondary CPPs and particles taken from the ascites fluid from a patient with calcifying peritonitis revealed a distinct similarity.⁵

This background shows the necessity of research in the field of fetuin-A ranging from fundamental research with respect to the biological function of fetuin-A and the CPPs to their clinical relevance. Moreover, CPP research is of great interest for various fields of applications. For example, there is the demand for controlled formation and stabilization of mineral colloids in the fields of material sciences, bionanotechnology and food industry.

Hence, the research presented in this work also aims into different directions. Initially, it is important to elucidate the impact of different conditions, such as temperature and the ratio of fetuin-A and mineral, on the process of CPP transformation as well as on shape and morphology of the CPPs themselves. Detailed knowledge and understanding of the proceeding processes is essential to enable a defined particle generation and use e.g. for applications in the field of material sciences. For that purpose, explicit investigations on the time-dependent changes of CPP shape and morphology during their conversion are additionally necessary.

A second approach leads into the direction of the structure of the fetuin-A molecule. Knowledge of the molecule morphology is indispensable to finally elucidate its detailed

function. Therefore, yet another aim is to investigate its three-dimensional shape and structure in solution.

Furthermore, interaction of Fetuin-A with the CPPs is investigated on single molecule-level to investigate the reversibility of fetuin-A binding to the CPP surface.

Those various approaches are necessary in order to characterize the fetuin-A molecule on the one hand and to understand the mineral stabilization by fetuin-A on the other hand. The present work focuses on the elucidation of the fundamentals. Knowledge of the involved molecular structures and understanding the occurring processes will be indispensable for future application of the described system whether for the selective prevention of ectopic calcification or for the application in the field of the controlled formation of mineral colloids.

2 Theory

2.1 Biomineralization

Biomineralization is a naturally occurring irreplaceable phenomenon. Nevertheless, wide areas are poorly understood up to now. The field of biomineralization connects the interests of natural scientists with that of medical scientists. Thus, it demonstrates very well the need and relevance of interdisciplinary research in order to elucidate the different processes and their relations in more detail. The scope of interest covers a wide range of different hierarchical levels ranging from molecular phenomena to the point of skeletal tissue. Knowledge of biomineralization principles is then suitable e.g. for applications in chemistry, nanotechnology and material science.

A basic step of biomineralization is a chemical precipitation reaction occurring spontaneously in supersaturated or metastable solutions.⁷ An example system is the extracellular fluid of vertebrates, which is supersaturated with respect to calcium and phosphate. Thus, stabilization mechanisms to avoid unwanted ectopic calcifications are required. Such mechanisms exist for example on protein level. One of the most famous proteins in terms of calcification prevention in vertebrates is the protein fetuin-A.

2.2 Fetuin-A

Fetuin-A is a liver-derived serum protein which belongs to a family of four structurally related plasma proteins containing cystatin-like protein domains: the cystatins.⁸ In literature it is also named as α 2-Heremans-Schmid (HS) glycoprotein. This inconsistency results from the discovery of different homologues by different researchers. In 1944, the bovine fetuin was described by Pedersen for the first time.¹ He found that it was the most abundant globular protein in fetal calf serum and therefore named it fetuin, derived from the latin word *fetus*. Heremans, Schmid and Bürgi identified the human homologue in 1960/61.^{9,10} In honor of its discoverers, it was later named α 2-HS glycoprotein.

Fetuin-A is highly expressed in the fetus.¹¹ After birth, its serum level decreases rapidly to reach a physiological serum concentration of 0.58 mg/ml in the adult organism.^{12,13} Additionally, fetuin-A is available in the liver, the location of its synthesis. Due to its high mineral affinity fetuin-A is also abundant in bone¹⁴ and teeth¹⁵.

Fetuin-A consists of three domains. The domains D1 and D2 are cystatin-like while the third domain D3 is rich in proline.¹⁶ Domain D1 contains an array of acidic residues which was found to be responsible for mediating the binding to basic calciumphosphate.^{3,16} The domain D3 could not be elucidated in detail so far.

The human fetuin-A molecule is built up of 349 amino acids. In addition, an 18 amino acids long signal-peptide is found on its N-terminus. Ultracentrifugation studies on bovine fetuin revealed a molecular weight M_w in the range of 50 kDa: While Pedersen found values of $M_w=50.6$ kDa for calf fetuin and $M_w=48.7$ kDa for fetuin from cow's fetus¹⁷, the molecular weight calculated by Spiro on the basis of sedimentation studies is 48.4 kDa¹⁸ for fetuin isolated from pooled fetal calf serum. Fetuin-A undergoes several posttranslational modifications such as glycosylation^{19,20} and phosphorylation²¹.

The binding affinity of fetuin-A for hydroxyapatite has already been reported in 1978.²² In 1996, Schinke et al. could show that fetuin-A is able to inhibit the formation of hydroxyapatite in mineralizing calvaria cells.¹⁶

In 2003, Schäfer et al. successfully generated fetuin-A knockout mice.² Knockout mice are selectively cultured mice lacking the gene(s) encoding for one (or more) specified proteins. In the present case of fetuin-A research, littermice lacking the gene for fetuin-A were investigated. Feeding them with a mineral rich diet led to diverse and considerable calcifications, especially of thorax, kidneys and testes. Those studies revealed the significance of fetuin-A in the prevention of calcification. These results established the basis for further research on the protein fetuin-A, its role in the organism as well as on potential interactions with various molecules.

2.3 Calciprotein Particles (CPPs)

In the context of fetuin-A research, it was found that the protein is able to prevent supersaturated calcium phosphate solutions from precipitation in vitro.³

Adding calcium chloride and sodiumhydrogenphosphate to an aqueous buffer solution leads to an instantaneous mineral precipitation. In contrast, previous fetuin-A addition causes turbidity of the solution but no mineral sedimentation is observed for days. This behavior is due to a formation of colloidal fetuin-A mineral-nanoparticles, denoted as calciprotein particles (CPPs).³

Studies using different measuring techniques such as transmission electron microscopy (TEM) and dynamic light scattering (DLS) revealed two different CPP states which possess different morphologies. The first state can be observed directly after mixing of the different substances. TEM investigations revealed that the CPPs exhibit a spherical shape in this state. DLS measurements provide a hydrodynamic radius in the range of about 50 nm.⁴⁻⁶ This first CPP state is only transiently stable. During a transformation process, CPP morphology changes towards larger prolate ellipsoids with hydrodynamic radii in the range of 100-120 nm.⁴⁻⁶ In TEM pictures, their structure seems to be less compact compared to the first state, their appearance is needle-like.⁵ The semi-axes ratio of second-state CPPs was estimated to be $b/a=0.3$ by analysis of electron micrographs.⁵ In addition to their different radii, the two states can also be distinguished by the internal composition of the CPPs. In the first state, the spherical particles consist of an amorphous phase of fetuin-A and calcium phosphate, whereas secondary CPPs are composed of a core of OCP and a dense shell in the form of a fetuin-A monolayer.⁴ Different investigations showed that fetuin-A can at least be partially replaced by other molecules that exhibit high affinity for calcium and/or apatite, e.g. albumin.^{5,23}

Concurrently with the CPP research Young et al. investigated so-called *nanobacteria*: nanoparticles in the same size range as the CPPs.^{24,25} Initially, those particles were described as putative living entities.²⁴ However, as research progressed, this statement was refuted and the particles were identified as crystallizations of minerals and organic molecules.²³ Hence, parallels to the CPP research can be drawn. The investigations showed that the particle composition depends on the environment they are forming in. It was found that the proteins associated with the nanoparticles reveal their predominance in the used serum samples.²⁴

Obviously, the composition of the nanoparticles can be affected by variations in the formation environment.

The earliest stages of CPP formation were investigated using small angle neutron scattering in combination with a stopped flow setup.²⁶ According to that, the formation of the primary particles occurs within a fraction of a second.

Investigations on CPP topology, morphogenesis and exact composition using SANS with contrast variation showed that only approximately one half of the initially present mineral ions and only 5 % of the total amount of fetuin-A becomes embedded in the CPPs.^{4,27} In this context, a second, complementary mechanism of long-term mineral stabilization was uncovered, which occurs simultaneously with CPP formation. It could be proven that the other half of the mineral ions coalesces to small sub-nanometer-sized mineral clusters stabilized by fetuin-A monomers. The mineral particles linked to the fetuin-A monomers are evocative of *Posner Clusters*.²⁷ Posner Clusters are tiny calcium-phosphate clusters that have been proposed as mineralization precursors and building blocks of amorphous calcium phosphate.^{28,29} According to the CPP nomenclature Heiss et al. named this second type of particles calciprotein monomers (CPMs).²⁷ The interplay of both mechanisms, that is the simultaneous formation of CPPs and CPMs, leads to an immediate stabilization of supersaturated solutions with respect to calcium and phosphate.

Recently, the clearance of *in vitro* generated CPPs from circulation was studied in mice. Those investigations showed that CPPs are effectively cleared from blood by macrophages of the monocytic phagocyte system as immunofluorescence staining revealed CPP accumulation in hepatic (Kupffer cells) and splenic macrophages.³⁰ Both cell types are known to be involved in the clearance of aged blood cells.³¹ It was shown that CPP clearance from circulation is considerably faster than the clearance of mere fetuin-A.³⁰ Those results revealed that beyond mineral stabilization CPPs obviously play an important role in the mineral removal from circulation.³⁰

The difference in cellular uptake of the mere fetuin-A and the CPP-bound fetuin-A reflects the importance of understanding the general connection between the shape and morphology of both fetuin-A and the CPPs and their function within the prevention of unwanted mineralization and calcification. There is obviously the need to elucidate and understand the fetuin-A shape and structure as well as the time-dependent changes in CPP morphology.

3 Methods

3.1 Basic Principles of Scattering

Scattering of electromagnetic waves is a powerful tool to study (bio-)polymers as well as biological complexes such as the CPPs consisting of protein and mineral. In a typical scattering experiment, samples are irradiated with electromagnetic waves e.g. in the form of light or X-rays with known wavelength. The radiation partly passes the sample unaffectedly while another part is scattered. The intensity $I(\theta, t)$ of the scattered light is measured at a scattering angle θ .³²

Two types of scattering experiments can be distinguished: static and dynamic scattering experiments. Static scattering is applied for gaining structural information by investigating the scattering intensity in dependence on the scattering angle. This method provides information on particle shape and intramolecular arrangement of material as well as on the mean molar mass of the particles.³²

In dynamic scattering experiments, the Brownian motion of particles is utilized in order to gain information on the particles' diffusion characteristics. The term *Brownian motion* refers to the random motion of a particle in a fluid (or gas) which is caused by statistical collisions of the particles with the molecules in the surrounding liquid (or gas). The distance between different scattering centers changes with time due to the Brownian motion of the particles. This in turn leads to time-dependent changes in the interference of scattered light from different scattering centers. The resulting time-dependent intensity fluctuations depend on the velocity of particle motion in the sample. The bigger the particles the slower is their motion and with that the measurable intensity fluctuations. Furthermore, the characteristic fluctuation time depends on temperature and viscosity of the surrounding medium which has to be considered for data evaluation. From dynamic scattering experiments it is thus possible to calculate the hydrodynamic radius of the particles and to gain information on time-dependent fluctuations of the particles' configuration and shape. In dynamic scattering, intensity is investigated time-dependently.

In the present study, visible light and X-rays were used to study the system of mineral stabilization by the formation of CPPs in the presence of fetuin-A. In light scattering, intensity fluctuations are associated with changes in the dielectric properties or rather the refractive index.³² In contrast, in X-ray scattering the measured intensity is a function of the electron density in the investigated sample. The scattering power of an atom is thus proportional to its number of electrons. The scattering contrast increases with increasing difference in the electron density of particle and solvent.³³

The biggest challenge in data interpretation consists in circumventing the phase problem which is inherent to all scattering experiments. It results from the fact that the only directly accessible variable is the scattered intensity. The scattered intensity is related to the electric field of the scattered wave by

$$I(\vec{q}) = |E(\vec{q}, t)|^2 \quad (3.1)$$

where \vec{q} is the scattering vector (see section 3.2 for detailed description). Any phase information concerning the scattered light is lost by detection of the scattering intensity.

An additional fact becomes important for data evaluation of static scattering experiments usually performed in order to gain information on the particle structure and shape. The particles are investigated in solution where they exhibit random orientation. Hence, the resulting scattering function is an average scattering function of all particles and all their possible orientations in the detection volume. This problem is called the scattering problem and describes the computation of the angle-dependent scattering function $I(\vec{q})$ for a certain particle.³⁴ Therefore, careful evaluation of static scattering data is necessary to obtain reliable information on the shape and structure of the investigated particles. Details are described in section 3.4.

3.2 Basic Principles of Light Scattering

With regard to the investigation of biological samples, light scattering provides the advantage of being non-destructive. This means that the sample system is neither changed nor disturbed by applying light scattering methods.

In light scattering, the sample is irradiated with coherent, monochromatic light with a wavelength in the dimension of the scattering particle. This enables the investigation of the overall macromolecule rather than to provide information on its microstructure. The electric field $\vec{E}(\vec{r}, t)$ can be described by

$$\vec{E}(\vec{r}, t) = \vec{E}_0 e^{i(\vec{k}\vec{r} - \omega t)} \quad (3.2)$$

with the electric vector \vec{E}_0 polarized perpendicular to the scattering plane.

The propagation vector of the incident light \vec{k} depends on the wavelength λ of the light in the investigated medium and has a magnitude of

$$|\vec{k}| = \frac{2\pi}{\lambda} \quad (3.3)$$

The setup of a typical scattering experiment is shown in Figure 3.1. The same figure shows the expanded view of the scattering volume.

The interaction of the incident electromagnetic wave with the molecules in the sample forces the electrons in the sample to oscillate. According to the occurring quasi-elastic scattering, the induced dipoles are origin of coherent spherical waves of the same frequency. Thus, the magnitude of incident and scattering vector are the same. The scattered light can be detected at an angle θ in the far field (compare Figure 3.1).

Assuming weak scattering, the main part of the incident beam passes the sample unaffectedly while only a minor part is scattered. The incident beam is not significantly influenced by interaction with the sample. The probability of higher order scattering is neglected in normal light scattering experiments. However, if turbid samples need to be investigated, higher order scattering cannot be neglected. In such cases, a special setup (three dimensional cross correlation dynamic light scattering, 3D-DLS) can be used for sample investigation. This method is described in more detail in section 3.3.3.

The scattered light detected by a point detector at position \vec{R} in the far field can be described by

$$\vec{E}_S(\vec{R}, t) = -\frac{\vec{k}^2 \vec{E}_0}{4\pi \vec{R}} e^{i(\vec{k}\vec{r} - \omega t)} \int_V \left[\frac{\varepsilon(\vec{r}, t) - \varepsilon_0}{\varepsilon_0} \right] e^{(-i\vec{q}\vec{r})} d^3r \quad (3.4)$$

where ε_0 is the average dielectric constant of the medium and V is the scattering volume.³² The scattering vector \vec{q} is defined as the difference between the propagation vectors of scattered light \vec{k}_S and the incident light \vec{k}_I (compare Figure 3.1):

$$\vec{q} \equiv \vec{k}_S - \vec{k}_I; \quad q \equiv |\vec{q}| = \frac{4\pi}{\lambda} \sin \frac{\theta}{2} \quad (3.5)$$

In principle, every particle in the sample volume can interact with the incident beam in the form of scattering. Thus, the detected intensity is a superposition of scattered light emitted from various particles in the sample volume with different phase relationship. The particles' Brownian motion leads to a randomized, time-dependent arrangement of dipoles in the sample. Those changes in the local dielectric constant lead to temporal variations within the detected intensity of the scattered light. The electrical field emanating from the scattering volume is the spatial Fourier transform of time-dependent changes in the local dielectric constant. Hence, intensity fluctuations in light scattering are used to gain information on the structure and dynamics of the particles in reciprocal space.³²

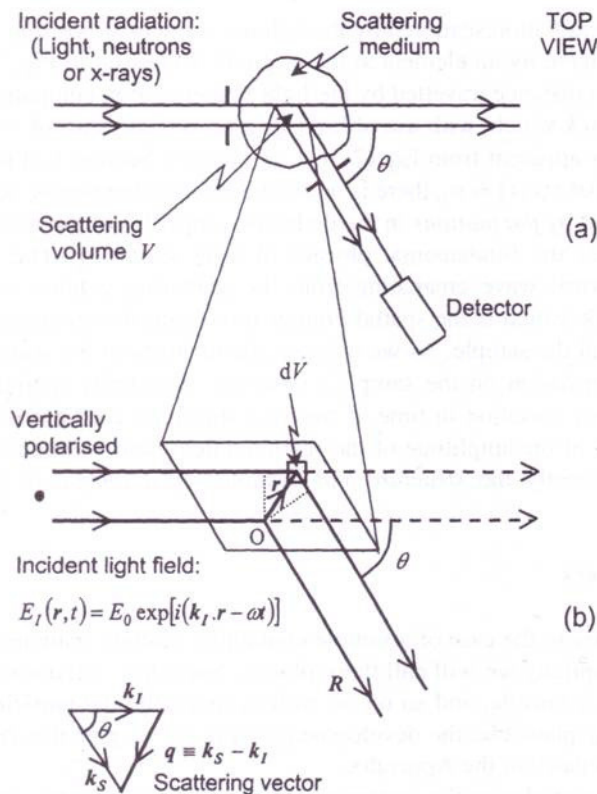


Figure 3.1: (a) Setup of a typical scattering experiment, top view. (b) Expanded view of the scattering volume. (Illustration taken from Pusey^{32a}, bold letters indicate that the variables are vectors.)

3.3 Dynamic Light Scattering

Dynamic light scattering (DLS) is applied to gain information on the diffusion coefficient of (bio-)polymers and corresponding complexes in solution. The method can be used to determine hydrodynamic radii and size distributions of the particles.

3.3.1 Correlation Functions in Dynamic Light Scattering

The scattered light at a given time and position in the far field is the result of constructive and destructive interference of light scattered at different scattering centers in the solution. The relative arrangement of the particles in solution varies time-dependently due to Brownian motion. This in turn leads to time-dependent fluctuations in the intensity of the scattered light as shown in Figure 3.2. These random intensity fluctuations contain information on the particle motion in solution.

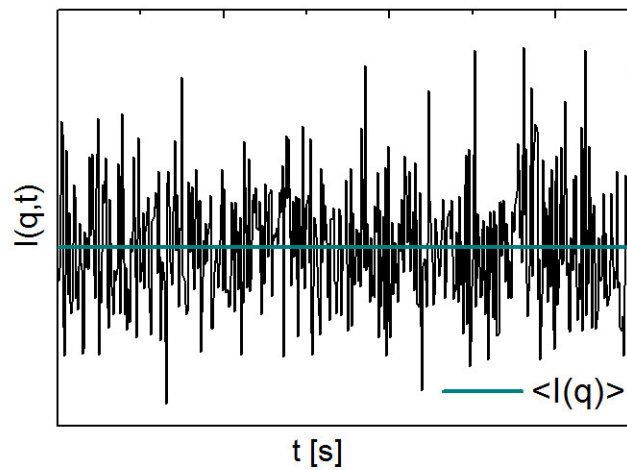


Figure 3.2: Time-dependent intensity observed at a detector in the far field. Intensity fluctuations result from changes in the relative particle configuration due to Brownian motion (graph modified from Eckert)³⁵.

In dynamic light scattering, autocorrelation of the intensity fluctuations is used to extract the diffusion coefficient of the particles in solution. The autocorrelation function of the detected intensity can be described by

$$\langle I(t)I(t + \tau) \rangle \equiv \lim_{T \rightarrow \infty} \frac{1}{T} \int_0^T dt I(t)I(t + \tau) \quad (3.6)$$

where T is the measurement time. The intercept of this function is at the mean-square intensity $\langle I^2(t) \rangle$, it decays to the square of the mean $\langle I(t) \rangle^2$. The characteristic time of this decay is a measure of the typical intensity fluctuation time.

In addition to the time dependency, the intensity I always depends on the scattering vector \vec{q} . For the following derivation it is assumed that measurements are performed at a defined angle so that \vec{q} remains constant. Thus, the intensity I is only considered time-dependently and therefore denoted as $I(t)$ rather than $I(\vec{q}, t)$ in the following.

In a DLS experiment, the normalized intensity correlation function $g^{(2)}$ is determined:

$$g^{(2)}(\tau) = \frac{\langle I(t)I(t + \tau) \rangle}{\langle I(t) \rangle^2} \quad (3.7)$$

For the simplest case of a dilute dispersion, the function decays exponentially from $g^{(2)}(\tau) = 2$ to $g^{(2)}(\tau) = 1$.

For the interpretation of a DLS experiment, the field correlation function $g^{(1)}$ is necessary as it contains information on the diffusion coefficient of the particles as shown in section 3.3.2. It is sometimes also named as *measured intermediate scattering function*:³⁶

$$g^{(1)}(\tau) = \frac{\langle E(t)E(t+\tau) \rangle}{\langle I(t) \rangle} \quad (3.8)$$

The field correlation function is related to the normalized intensity correlation function via the so-called *Siegert relation* under the condition that the electrical field of the scattered radiation exhibits Gaussian statistics:

$$g^{(2)}(\tau) = 1 + \beta[g^{(1)}(\tau)]^2 \quad (3.9)$$

where β is a factor representing the degree of spatial coherence of the scattered light over the detector. β is a constant for the particular used setup and corresponds to the inverse number of coherence areas covered by the detector. In a typical DLS setup, $\beta = 1$. The field correlation function $g^{(1)}$ can be derived from the *measured intensity correlation function* $g^{(2)}$ by inversion of equation (3.9):

$$g^{(1)}(\tau) = \frac{1}{\sqrt{\beta}} \sqrt{g^{(2)}(\tau) - 1} \quad (3.10)$$

Just like the intensity I , the variables E , $g^{(1)}$ and $g^{(2)}$ are not only time-dependent but also depend on \vec{q} , which has been neglected for the derivation due to simplicity. Furthermore, all mentioned relationships were derived by considering a dilute sample containing spherical particles with identical size. However, equations (3.9) and (3.10) are applicable to any fluid system, in which the range of spatial correlations is considerably smaller than the linear dimension of the scattering volume.³⁶

3.3.2 Determination of Particle Size with Dynamic Light Scattering

DLS is usually used to determine the hydrodynamic radius of particles in solution. For that purpose, the diffusion coefficient has to be extracted from the measured intensity correlation function. Therefore, the dependency of the field correlation function on the time-dependent particle arrangement in the solution can be used:

$$g^{(1)}(\tau) = \langle e^{-i\vec{q}[\vec{R}(0) - \vec{R}(\tau)]} \rangle = \langle e^{i\vec{q}\Delta\vec{R}(\tau)} \rangle \quad (3.11)$$

where

$$\Delta\vec{R}(\tau) \equiv \vec{R}(\tau) - \vec{R}(0) \quad (3.12)$$

is the particle displacement in time τ .³⁶

Assuming that the positions of the particles are uncorrelated, the displacement of a particle in Brownian motion is a (real) three-dimensional random variable with Gaussian probability distribution.³⁶ The particle's mean-square displacement in time τ is:

$$\langle \Delta\vec{R}^2(\tau) \rangle = 6D_0\tau \quad (3.13)$$

Via the *Einstein-(Smoluchowski) relation*, the diffusion coefficient of a particle is given as

$$D_0 = \mu k_B T \quad (3.14)$$

where k_B is the Boltzmann constant, T is the temperature and μ is the mobility of the particle.

For small Reynolds numbers (laminary flow conditions), the mobility corresponds to the inverse friction coefficient of a particle. Hence, for spherical particles with a radius r , equation (3.14) turns into the *Stokes-Einstein equation*:

$$D_0 = \frac{k_B T}{6\pi\eta r} \quad (3.15)$$

where η is the solvent viscosity.

Evaluation of the average in equation (3.11) over the Gaussian probability distribution of the particle displacement gives³⁶

$$g^{(1)}(\tau) = e^{\left[-\frac{\bar{q}^2}{6}\langle\Delta\bar{R}^2(\tau)\rangle\right]} = e^{-\bar{q}^2 D_0 \tau} \quad (3.16)$$

Determining $g^{(1)}(\tau)$ via DLS measurement of $g^{(2)}(\tau)$ and equation (3.10) with subsequent fitting to an exponential in delay time τ provides the decay rate $D_0 q^2$. The absolute value of the scattering vector $|\vec{q}|$ can be determined from the detection angle, the laser wavelength and the refractive index of the solution via equation (3.5). Hence, the DLS experiment provides the diffusion coefficient of the investigated particles in solution. Subsequently, their hydrodynamic radius can be calculated from the Stokes-Einstein equation (equation (3.15)).³⁶

Typically, the size distribution of bio-polymers and their mineral complexes is not monodisperse but exhibits polydispersity. In these cases, the field correlation function is a sum of exponentials, each corresponding to a particular particle (type) weighted by the particular scattering intensity.³⁶ Different fitting routines are applicable for data extraction and interpretation of DLS measurements from polydisperse samples.

For samples where $g^{(1)}(\tau)$ can be fitted by a sum of exponentials whose decay rates differ by a factor 10 or more, approaches using Laplace transformation can be used for data fitting in order to determine the hydrodynamic radii. A commonly used fit program based on this approach is CONTIN.³⁶ A detailed description of the algorithm can be found e.g. in the work of S. Provencher.³⁷

A widely used method for fitting DLS data of particles with relatively narrow size distribution is the method of moments (or cumulants) providing limited but well-defined information on the sample system³⁶. In this method, the experimentally determined $g^{(1)}(\tau)$ is compared to a single exponential. Information on particle polydispersity can be derived from the deviation of both functions. Practically the cumulant fit is a series expansion of $g^{(1)}(\tau)$:

$$\ln g^{(1)}(\tau) = -\kappa_1 \tau + \frac{1}{2!} \kappa_2 \tau^2 - \frac{1}{3!} \kappa_3 \tau^3 + \dots \quad (3.17)$$

The first cumulant κ_1 provides the mean diffusion coefficient $\langle D \rangle = \frac{\kappa_1}{q^2}$, from which the mean hydrodynamic particle radius can be derived via Stokes-Einstein equation (equation (3.15)). The second cumulant $\kappa_2 = (\langle D^2 \rangle - \langle D \rangle^2) q^4$ additionally provides quantitative information

on the polydispersity of the particles in the sample. For narrow distributions, terms of higher order than the quadratic are neglected.

3.3.3 Three-dimensional cross correlation Dynamic Light Scattering (3D-DLS)

The theory described for dynamic light scattering in the previous sections holds true assuming that the investigated sample is transparent. In that case, the majority of photons passes through without scattering, while a minority of photons is scattered once and multiple scattering is negligible. However, in the case of CPP research multiple scattering cannot be neglected as the samples turn turbid while CPPs transform from first into second state. If turbid samples are investigated by means of light scattering, the detected light does not only comprise singly scattered photons but also photons which have been scattered several times while passing the sample. Mathematically, those multiply scattered photons contribute to the autocorrelation function with the same weighting as the singly scattered photons. Therefore, extraction of information on particle size and dispersity becomes more difficult. Performing standard light scattering experiments is no longer possible.³⁶

So called three-dimensional cross correlation dynamic light scattering (3D-DLS) has been developed for the investigation of turbid samples.³⁸ The 3D cross correlation scheme effectively suppresses multiple scattering contributions and enables direct analysis of the evaluable single scattering.

The method relies on two focused laser beams crossing in the sample. Both the incident and the detected light paths are placed at an angle $\delta/2$ above and below the plane of symmetry of the scattering experiment.³⁸ Detection of the scattered light is carried out using two detectors whose signal is cross-correlated. Only contributions of singly scattered light evoke correlated intensity fluctuations on both detectors while multiply scattered light leads to uncorrelated intensity fluctuations contributing only to the background. Hence, analysis of the resulting scattering pattern allows to selectively filter and analyze the singly scattered light. A detailed description of the method can be found in the work of Urban.³⁸ The proximate determination of the diffusion coefficient and the subsequent calculation of the hydrodynamic particle radius are performed as described for dynamic light scattering experiments in the previous sections (3.3.1 and 3.3.2).

3.4 Basic Principles of Static Scattering

3.4.1 The Phase Problem

Phase information of the scattered light is lost due to the detection of the scattering intensity in any scattering experiment using electromagnetic radiation (compare section 3.1). This complicates the process of data interpretation. Additionally, the q -dependent intensity of the scattered light is an average scattering function of all particles with random orientation in the detection volume. This problem has already been mentioned in section 3.1. It is called the scattering problem meaning the computation of the angle-dependent scattering function $I(q)$ for a certain particle.³⁴ Thus, scattering functions need to be evaluated carefully to obtain information on the shape and structure of the investigated particles. The evaluation of scattering data is also termed 'resolving the inverse scattering problem' meaning the determination of the shape and structure of a particle from its scattering pattern.³⁴

The most simple approach to solve the occurring problems would be to guess a model, solve the scattering problem and compare the resulting theoretical scattering function with the one obtained from the experiment.³⁴ Unfortunately, the complexity of information contained in this one single function, the scattering function, makes it difficult to use a simple trial-and-error search to obtain the relevant information.

A common approach to solve the problem has been developed by Glatter et al.³⁹ and will be described in the following. Scattering experiments can be described by the *Rayleigh-Debye-Gans (RDG) theory*. A regular and homogenous propagation of the incoming plane wave into and through the particle is assumed implying that the magnitude of the field is the same in all parts of the particle. It describes well *small-angle X-ray scattering (SAXS)* as well as *static light scattering (SLS)* of particles with sizes much smaller than the wavelength.^{39,40}

The scattered field can be expressed by

$$\vec{E}_S(\vec{q}) = \text{const} \int_V \rho(\vec{r}) e^{-i\vec{q}\vec{r}} d\vec{r} \quad (3.18)$$

where V is the illuminated scattering volume and $\rho(r)$ is the density. For the scattering at $\vec{q} \neq 0$, only the density fluctuations contribute to the scattering field, so that (3.18) turns into

$$E_S(\vec{q}) = \text{const} \int_V \Delta\rho(\vec{r}) e^{i\vec{q}\vec{r}} d\vec{r} \quad (3.19)$$

Inhomogeneities of the solvent are usually very small and are taken into account by subtraction of the solvent scattering curve from the scattering curve of the sample.⁴⁰

In the context of RDG theory, it can be shown that the scattering function $I(\vec{q})$ is the Fourier transform of the *pair distance distribution function (PDDF)* $p(\vec{r})$:

$$p(\vec{r}) = \frac{1}{2\pi^2} \int_0^\infty I(\vec{q}) q r \sin qr dq \quad (3.20)$$

For homogenous particles, the meaning of the PDDF can be related to a distance histogram with a height proportional to the number of distances that can be found inside the particle within the interval r and $r+dr$ (see Figure 3.3).⁴⁰

For inhomogeneous particles, $p(\vec{r})$ is proportional to the difference-density length pairs in the interval $r+dr$. Due to spatial averaging, the orientation is unimportant. The PDDF can be used to obtain structural information on homogenous and even inhomogeneous particles.⁴⁰

However, the more complicated the investigated system (e.g. non-spherical, inhomogeneous particles) the more difficult it is to obtain information solely from the PDDF. Apart from that, some characteristics give more pronounced effects in reciprocal space.⁴⁰ Therefore it can be necessary to work with the scattering function $I(q)$. Hence, different approaches to obtain information directly from the scattering function $I(q)$ have been developed or are under development. Examples for data evaluation using the scattering function $I(q)$ can be found in chapter 4.3.

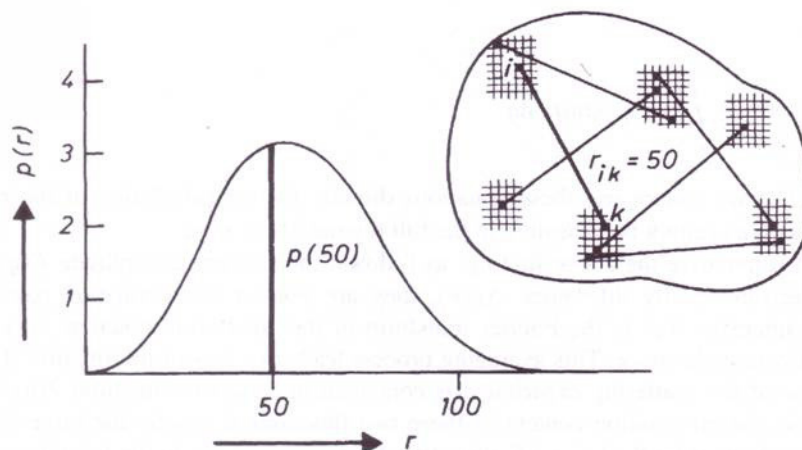


Figure 3.3: Definition of the PDDF (figure taken from Glatter)^{40a}.

3.4.2 The Scattering Function

In a static scattering experiment, the intensity I is measured q -dependently. Thus, after the scattering experiment, the scattering function $I(q)$ can be evaluated to obtain information on the investigated sample. For the case that a 2D detector has been used, radial integration of the intensity over the detector area is necessary in order to receive the typical scattering function.

A scattering function can be divided into four characteristic regimes. Every regime contains different and specific information on the sample, whereby the *Porod regime* as well as the *Guinier regime* play the most important role in the present work. The *Guinier regime* ($q \cdot r \leq 2$) can be used to determine the radius of gyration R_G via the so-called *Guinier plot* (compare section 3.4.4.1).⁴⁰ In the case of a spherical particle, the radius of gyration R_G is connected to the particle radius r via:

$$r = \sqrt{\frac{5}{3}} R_G \quad (3.21)$$

Furthermore, R_G can be used to estimate the spatial dimensions of particles with non-spherical shape and of irregularly formed particles.

The subsequent higher q -range ($q \cdot r > 5$) is called *Porod regime*. This is the regime, in which oscillations caused by the particle size and shape can be found in the $I(q)$ vs. qr plot. In the $\log I(q)$ vs. $\log q$ plot, the envelope of those oscillations follows a power law:

$$I(q) \propto q^{-j} \quad (3.22)$$

The exponent j depends on the particle shape and is 4 in the case of spherical particles and 1 for rods. Therefore, the scattering characteristics in the Porod regime can be used to determine the particle shape.

From the *Bragg regime* at high q , information on the inner structure of the particles can be derived. If the q -range is high enough, it is possible to determine the inter-atomic distance inside the particles. The low q -range is the range of forward scattering. From this regime it is possible to derive the molar mass of the particles. For concentrated samples, this is the regime to investigate possible particle interactions. Those interactions are expressed by the

interference of scattering which can be described by the structure factor $S(q)$ containing information on the particle interaction. For diluted samples, the structure factor $S(q) = 1$.³²

3.4.3 The Form Factor

Biopolymers and corresponding complexes as investigated in the present work exhibit a spatial extension that has to be considered for scattering experiments. This means that the interference of the scattering waves emanating from different scattering centers inside the macromolecules (e.g. the electrons in the case of X-ray scattering) has to be taken into account as the scattering power of the investigated particles becomes angle-dependent. The shape of the particles is considered by the so-called form factor. It is virtually the Fourier transform of the scattering centers of the investigated particle in solution and arises from the interference of scattered light within one particle. For particles without spatial extension, the form factor $P(q, r) = 1$, otherwise $P(q) \neq 1$.

In general, the form factor has to be considered as it influences the scattering intensity $I(q)$. This dependency is shown for homogenous spheres with radius r in the following equation:

$$I(q) = (\Delta\rho)^2 V^2 P(q) = (\Delta\rho)^2 V^2 \left[\frac{3(\sin(qr) - qr\cos(qr))}{(qr)^3} \right]^2 \quad (3.23)$$

with

$$P_{\text{Sphere}}(q) = \left[\frac{3(\sin(qr) - qr\cos(qr))}{(qr)^3} \right]^2 \quad (3.24)$$

being the normalized form factor of a homogeneous sphere. The previous equations (3.23)/(3.24) hold true for the case that the density fluctuations $\Delta\rho$ are not angle-dependent.⁴⁰

Equation (3.24) shows that the form factor $P_{\text{Sphere}}(q)$ simply depends on the product qr . Thus, a universal scattering curve can be obtained by plotting $I(q)$ vs. qr as shown in Figure 3.4. The function is identical for all spherical particles irrespective of their radius; the particle size can be estimated from the zeros of the function at $qr = 4.493, 7.725, 10.904, 14.066, \dots$ ⁴⁰ The form factor minima become more and more diffuse with increasing polydispersity of the spheres.

For particle geometries deviating from the spherical shape (e.g. ellipsoids as investigated in the present work), the characteristic properties of the form factor are less pronounced, so that data evaluation is more complicated. However, fitting approaches as described in chapters 4.2 and 4.3 can be used to obtain information on the investigated sample from the form factor.

In case of the presence of multiple particle types, the form factor determined by a scattering experiment is composed of the form factors of the included particles. This has consequences for the interpretability of scattering data from samples containing multiple particle types as all form factors have to be taken into account (compare chapter 4.3).

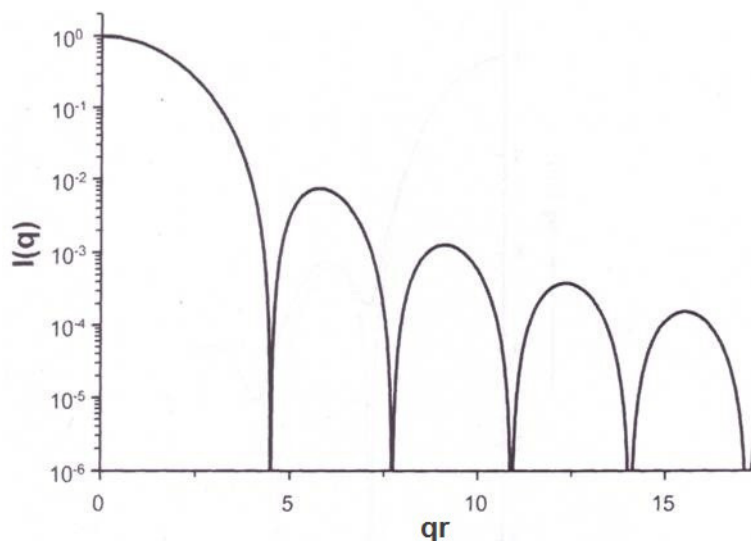


Figure 3.4: Form factor $P(q,r)$ for homogenous spheres (graph modified from Glatter)⁴⁰.

3.4.4 Static Light Scattering

Static light scattering (SLS) experiments belong to the static scattering experiments. The basic principles are described in sections 3.4.1 to 3.4.3. The experiments provide q -dependent scattering functions $I(q)$. The method can be used to determine the radius of gyration of (bio-)polymers and the corresponding mineral complexes. It additionally provides information on the particle shape as described in section 3.4. Usually 1D-detectors are used, so that the scattering intensity has to be measured separately for every scattering angle. With

$$|\vec{q}| = \frac{4\pi n_0}{\lambda} \sin \frac{\theta}{2} \quad (3.25)$$

the scattering vector q can be determined for every detector position (see Figure 3.1). n_0 is the refractive index of the solvent.

In the present work, SLS data were combined with SAXS data to expand the evaluable q -range. The results are described in chapter 4.3.

3.4.4.1 Guinier Approximation and Determination of R_G

The characteristics of the scattering function in the Guinier regime ($q \cdot r \leq 2$) can be described by:

$$I(q) = I(0)e^{-\frac{q^2 R_G^2}{3}} \quad (3.26)$$

(compare section 3.4.2). This approximation can be used to determine the radius of gyration R_G . Therefore, $\ln(I(q))$ is plotted vs. q^2 in a so called *Guinier plot*. The slope of the resulting straight line is proportional to R_G^2 .⁴⁰

This shows that a well-defined parameter of any scattering object - the radius of gyration - can directly be obtained by its small q -scattering. When investigating non-monodisperse, non-spherical samples, the obtained radius of gyration is averaged over the distribution of sizes and shapes.³²

3.4.5 Small Angle X-Ray Scattering

Just like SLS, *small-angle X-Ray scattering (SAXS)* belongs to the static scattering experiments. Similar to SLS it provides q -dependent scattering functions $I(q)$. The applicable size range of SAXS is shifted to higher q -values compared to SLS as smaller wavelengths are used to perform the experiment. A combination of SAXS- and SLS-data is possible to increase the data-containing q -range which can facilitate data interpretation. Unlike in the SLS experiment the detectors used in SAXS are usually two-dimensional. The scattering functions are calculated by radial integration of the 2D-detector intensities. Typically, a beam stop is used to prevent the detector from damage caused by the primary (unscattered) beam. A schematic setup of a SAXS experiment is shown in Figure 3.5.

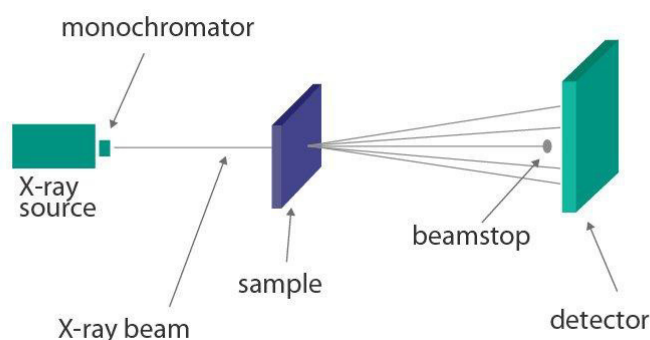


Figure 3.5: Schematic setup of a SAXS experiment.

SAXS can be used to investigate the particle size and shape as done for the fetuin-A molecule and the CPPs in the present work. The experimental results are described in chapter 4.2 and chapter 4.3, respectively. If the SAXS measurements are performed at a synchrotron X-ray source with high flux, measurement times are reduced to several minutes or even seconds providing two clear advantages: On the one hand it is possible to investigate (small) biological samples in a few seconds and prevent any interaction of beam and sample. This is especially interesting for investigations on the protein structure as performed for fetuin-A in the present work. The details are described in chapter 4.2. On the other hand, it is possible to follow time-dependent shape changes of particles, which was done for the CPPs in the present work. Details are described in chapter 4.3.

3.5 Fluorescence Correlation Spectroscopy

Unlike the scattering methods described in the previous sections, fluorescence correlation spectroscopy (FCS) is not an ensemble method. With FCS it is rather possible to study single molecules and interactions of different molecular species on single-molecule level. Therefore, fluorescent labeling of the molecules of interest is necessary.

A considerable feature of the FCS measurements is the possibility to perform two-color experiments. Subsequent cross correlation of signals from differently labeled species provides information on correlated motions of the respective molecules.

3.5.1 Fluorescence

Fluorescence is the process of spontaneous radiation emission of an excited physical system in the visible wavelength regime after excitation. Absorption of the exciting energy results in an electron transition from the electronic ground state S_0 to an excited electronic state S_1 , S_2 , S_3 , ... (depending on the excitation energy). Energy dissipation from higher states to S_1 occurs in the form of internal conversion without radiation emission. Subsequent transition from S_1 to S_0 is accompanied by photon emission known as fluorescence. Fluorescence transition is spin-permitted and fluorescence ends almost simultaneously with the end of illumination. Instead of a direct transition from S_1 to S_0 internal conversion to a triplet state is also possible. The conversion is accompanied by a change in spin multiplicity which prohibits the direct transition from the excited triplet state to the ground state. This leads to extended retention times for the respective photons (phosphorescence). Triplet excitation causes correlated emission on the microsecond scale. This in turn contributes to the correlation functions of the FCS experiment and has to be taken into account for data evaluation of samples carrying fluorescent labels that are subject to triplet excitation. An overview of the occurring transitions can be illustrated in a so-called Jablonski-diagram as shown in Figure 3.6. Usually the emitted energy is smaller than the absorbed energy resulting in larger wavelengths for the emitted fluorescent photons compared to the excitation photons. This phenomenon is known as Stokes shift.⁴¹

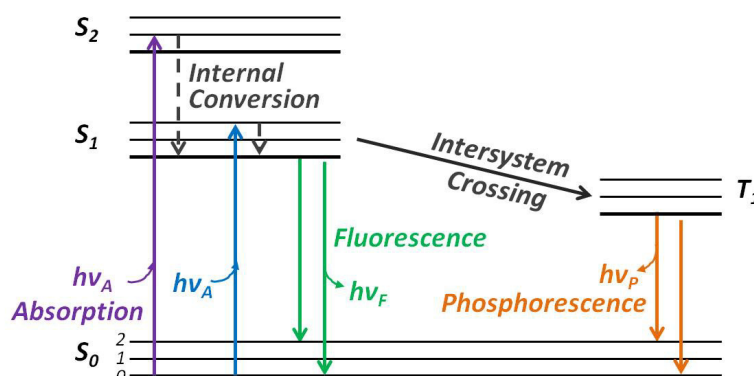


Figure 3.6: Jablonski diagram illustrating the possibly occurring transitions (redrawn from⁴¹).

3.5.2 Basic Principles of Fluorescence Correlation Spectroscopy-Measurements

Similar to dynamic light scattering, intensity fluctuations are the basis for fluorescence correlation spectroscopy measurements. Subsequent data evaluation provides information on diffusion coefficients, concentrations and interactions between different species.

The setup used for fluorescence correlation spectroscopy is based on a confocal microscope. Light of a (pulsed) laser source is focused into a (liquid) sample via an objective illuminating a preferably small excitation volume. Fluorescently labeled particles diffusing into the excitation volume are excited. As a consequence, fluorescent light with a larger wavelength compared to the excitation wavelength is emitted and can be detected. For detection of the single photon events so called SPAD (single photon avalanche detector) detectors are commonly used. Due to their high detection efficiency with very low background only small laser power is necessary for excitation. This in turn reduces the risk of photobleaching the sample and therefore ensures interpretability of the results. Detailed investigations on the

effect of photobleaching and its consequence on the fluorescence correlation spectroscopy experiment are described by Eggeling et al.^{42,43} and Nishimura et al.⁴⁴.

In addition to a small excitation/detection volume, small sample concentrations are necessary. This is in particular advantageous for biological samples as their availability is often limited. The ideal concentration is in a range between sub-nanomolar and micromolar for a confocal volume of about one femtoliter.⁴⁵ If both requirements are fulfilled, only few molecules are detected simultaneously and contribute to the intensity signal at the respective time. This is associated with the fact that the intensity fluctuations are significantly influenced by fluorescent molecules diffusing into or out of the focal volume. Similar to light scattering experiments, the intensity fluctuations are autocorrelated to gain the necessary information on the investigated system (compare section 3.3), in the present case proteins and protein mineral complexes.

3.5.3 Correlation Function

Data evaluation in FCS is based on the same principle as data evaluation in dynamic light scattering: the evaluation of intensity autocorrelation functions (see also section 3.3). In FCS data evaluation, precise knowledge of the detection volume is inevitable. Its size is one of the optical characteristics of the setup described by the so-called molecule detection function (MDF) as described e.g. in the work of Enderlein et al.⁴⁶. The MDF is the position-dependent probability of excitation and detection of a fluorescent photon from a molecule at a defined position \vec{r} . The MDF is non-time-dependent. In classical FCS theory, the MDF is approximated with a 3D-rotationally symmetric Gaussian ellipsoid with radius $r = 1/e^2$ as detection volume.⁴⁷⁻⁵⁰ The dimensions in x - and y -direction (rectangular to the optical axis) are equal while in z -direction they are elongated.

The molecules' motion between two points within a defined time can be described by *Greens probability density function* G . Neglecting intermolecular interactions and uncorrelated background contributions the so-called number density autocorrelation term can be calculated, which contains the diffusion coefficient of the investigated particles:⁵¹

$$G(r_1, t | \vec{r}_2, 0) = \frac{1}{(4\pi Dt)^{3/2}} e^{-\frac{(r_1 - r_2)^2}{4Dt}} \quad (3.27)$$

Therefore, similar to dynamic light scattering, the diffusion coefficient can easily be derived from the characteristic decay of the autocorrelation function.

3.5.4 Two-Focus Fluorescence Correlation Spectroscopy (2f-FCS)

Basis of a reliable data evaluation in FCS is the exact knowledge of the MDF. Unfortunately, it depends on various parameters of the optical setup including mismatches in the refractive index of sample and immersion medium of the objective, variations in the coverslide thickness and laser beam properties. In some cases, these parameters are difficult or even impossible to access. Additionally, the MDF strongly depends on the optical saturation of the fluorescent dye. This in turn depends on the environment of the fluorescent dye which considerably complicates the comparability of different measurements. Basis for all these problems is the missing intrinsic length scale in FCS.⁵²

In 2007, Dertinger et al. introduced an advancement in FCS, the so called two-focus fluorescence correlation spectroscopy (2f-FCS) circumventing the afore mentioned problems.⁵³ The schematics of the 2f-FCS setup is shown in Figure 3.7.

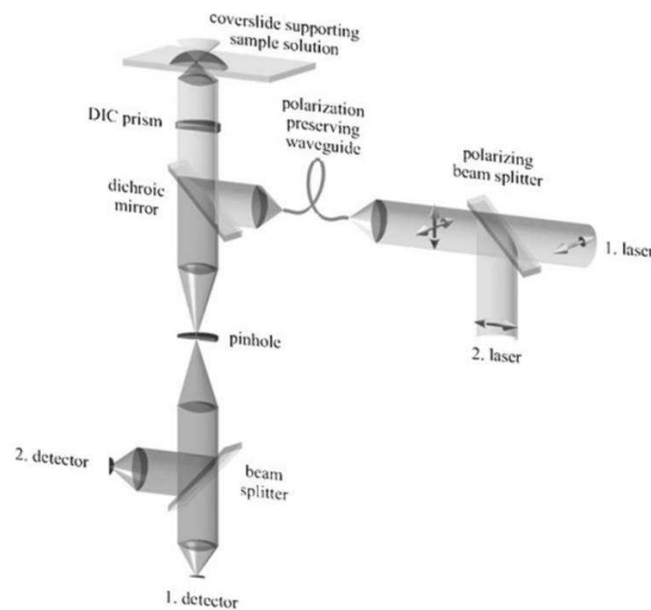


Figure 3.7: Schematics of the 2f-FCS setup.^{53a}

Instead of referencing the determined diffusion coefficient against a known standard, absolute values are measured in 2f-FCS. Compared to original FCS, two fundamental changes are necessary.⁵² First, instead of having only one focus, two laterally shifted but overlapping foci with known dimensions and distinct distance are generated and serve as intrinsic length scale in 2f-FCS. Second, the corresponding MDFs can be well described by a simple two-parameter-model in the ideal case of perfect setup alignment. In this case, accurate absolute diffusion coefficients become measurable.⁵²

For that purpose, autocorrelations are measured in both foci. 2f-FCS additionally provides a cross-correlation curve by correlating the signal of both foci among each other. While the shape of a simple autocorrelation function is completely determined by the underlying MDF, the cross-correlation additionally depends on the foci overlap.⁵² Unfortunately, an analytical solution is not possible in this case. Nevertheless, numerical optimization can be used to obtain the diffusion coefficient. Therefore, the relation between the distance of both foci and the time shift between auto- and cross correlation curves has to be taken into account. It is known that the relative time shift between auto- and cross correlation curves scales with the square of the foci distance divided by the diffusion coefficient. Additionally, the relation of auto- and cross correlation amplitude is a direct measure for the overlap of the foci.⁵² Hence, global fitting of auto- and cross correlation curves in consideration of the known focal distance provides the absolute diffusion coefficient of the measured particles. A detailed description of the theoretical background and in particular the setup used for the present work can be found in the PhD thesis of Claus B. Müller.⁵¹

4 Results

4.1 Formation and Stability Kinetics of Calcium Phosphate–Fetuin-A colloidal Particles probed by time-resolved Dynamic Light Scattering¹

4.1.1 Introduction

Since the mid-sixties of the last century, when biomineralization research started to attract a broader audience, calcium phosphate formation has been the subject of many investigations. According to X-ray diffraction analysis, calcium phosphate freshly precipitated from solution is amorphous to low-crystalline. Following Ostwald's ripening law precursors progressively convert to crystalline octacalcium phosphate (OCP) and finally to hydroxyapatite (HAP), which is the most stable phase at physiologic pH.^{54–56} Starting from these fundamental studies on the maturation of calcium phosphate sediments, protein controlled mineral formation attracted increasing attention. In biomineralization, evolutionary optimized proteins impose specific charge patterns or spatial constraints at the protein-mineral interface that may lead to biocomposites with exceptional properties.

Today, the controlled formation and stabilization of mineral colloids by proteins, peptides or biomimetic polymers has become an important issue in many fields of research. For example: Efforts were made to adapt and to optimise stabilized mineral colloids for applications (I) in bionanotechnology, e.g. bone repair, tooth remineralization, cell activation / transfection / drug delivery and for advanced hybrid materials.^{57–61} (II) In food industry, e.g. calcium phosphate stabilization in dairy products and inhibited ice crystal growth in foodstuffs by anti-freeze proteins.^{62,63} (III) In mammals, a few protein inhibitors are known to play a role in the inhibition of uncontrolled mineral deposition in the soft tissue. Several studies have documented the importance of colloidal protein-mineral composites as precursors of hard tissue formation, as well as their putative role in the safe transport of otherwise insoluble mineral load from the extracellular spaces to putative sites of clearance, like the kidney.^{64–67}

Fetuin-A / α_2 -HS glycoprotein is a 50 kDa serum protein which shows a high affinity for basic calcium phosphates. This property not only results in an accumulation next to the mineral phase in bone but also makes fetuin-A a very effective inhibitor of mineral deposition in the extracellular space.¹⁴ Fetuin-A deficient mice on a calcification sensitive DBA/2 background develop massive calcifications in the soft tissue.² Accordingly, fetuin-A has been identified as an essential inhibitor of soft tissue calcification in humans. Low serum fetuin-A levels in dialysis patients are associated with increased morbidity and mortality most likely due to unwanted mineral deposition in the soft tissue (ectopic calcification) which is a common complication in these patients.^{68,69}

¹ Large parts of the measurements described in this chapter have been performed in the context of the present work. The measurements using high supersaturation (HS) environment have been performed in the context of a diploma thesis.⁶ The article was written by Alexander Heiss.

Structural *in vitro* investigations have shown that a calcium and phosphate ion supersaturation is “buffered” by direct binding of subnanometer sized prenucleation clusters to fetuin-A monomers and by formation of mineral – fetuin-A colloids in the 100 nm range, denoted as calciprotein particles (CPPs) or fetuin mineral complex.^{3,27,70} Initial particles (primary CPPs) are spheres with a heterogeneous internal structure and a diameter in the 100 nm range. After a lag phase ranging from minutes to several hours depending on the balance of concentrations of fetuin-A and mineral ions and temperature, rapid particle growth is observed. Transmission electron microscopy revealed that at the onset of CPP transformation, small needles start to grow on the surface.³ Subsequently, an extensive morphological change of the CPPs was observed in this period resulting in prolate ellipsoidal particles. These secondary CPPs consist of a compact mineral core that is covered by a dense fetuin-A layer.⁴ CPPs are monodisperse and CPP transformation proved to be a highly uniform process. Here, this process of CPP maturation involving growth and structural reorganisation is denoted as CPP ripening in analogy to Ostwald’s ripening.⁷¹

Recent investigations support the relevance of CPP formation at least under pathophysiological conditions *in vivo*: (I) pathological calcium phosphate colloids have been isolated from the ascites of a peritoneal dialysis patient that closely resemble CPPs.^{4,5} (II) Experiments with rats have shown that the induction of a pronounced increase in mineral ion supersaturation in the blood of rats results in a surge of fetuin – mineral particles.^{72,73}

Mineral nanoparticles resembling primary CPPs can even be generated at low mineral ion supersaturation without any additive.^{74,75} However these nanoparticles rapidly aggregate to larger entities. In the presence of fetuin-A, initial prenucleation cluster formation is not affected by the protein but subsequent extensive aggregation is inhibited.²⁶ Even though a direct comparison is not possible due to the different approaches, some other molecules like the amino acid glycine or the tooth proteins amelogenin and dentin matrix protein 1 (DMP 1) seem to mediate the formation of calcium phosphate colloids that are reminiscent of primary and secondary CPPs, respectively.^{76–80} Likewise the presence of polymers also leads to particle morphologies reminiscent of CPPs.^{81–83} It can be inferred that the formation and the ripening of CPP-like particles mediated by acidic proteins or polymers follows universal principles.

However, native bovine fetuin-A (BF) perfectly combines availability, activity, stability and physiologic relevance.¹⁷ Thus, fetuin-A represents a prototypic biomineralization protein which is ideally suited for kinetic analyses of mineral ripening in the presence of an inhibitor or the investigation of protein-mineral interface effects.

In biomineralization research, the use of *in vitro* model systems is often inevitable because a direct investigation *in vivo* is often impossible due to impaired accessibility, high complexity or very slow reaction kinetics. Regarding the investigation of protein - calcium phosphate interactions, a few principal experimental setups have developed. Some experiments are based on *de novo* mineral formation, others include mineral seeds. Besides, numerous variations (mainly regarding the concentrations and temperature) of each setup often exist: (I) constant composition/pH-stat^{84–87}, (II) double diffusion gel^{88,89}, (III) buffered solution^{3,16,70}. A side by side comparison of the results is nearly impossible. The complementary nature of *in vitro* and *in vivo* studies may help to elucidate a macromolecule’s role but in general the applicability of *in vitro* results to more complex systems like in biomedical research or in bionanotechnological applications is often difficult. For example, temperature is obviously a

key parameter as it greatly determines the overall the reaction kinetics. But how does a temperature below body temperature affect mineral nucleation, CPP formation and CPP transformation? Does CPP aggregation occur?

Here we address some of the most relevant parameters driving CPP formation and ripening. We explore the kinetic and thermodynamic controls of CPP formation and ripening. To this end, we monitored CPP growth by time-resolved dynamic light scattering (DLS) under systematically altered conditions regarding temperature, fetuin-A concentration and mineral ion supersaturation. Our model system offers the advantage that all parameters can be adjusted easily. Time-resolved particle detection is non-destructive, fast and precise.

4.1.2 Experimental

4.1.2.1 Fetuin Preparation and *in vitro* Mineralization Model

Lyophilized bovine fetuin-A (BF, Sigma, F3385)¹⁷ was dissolved in Tris-buffered saline (TBS), centrifuged (4°C, 10.000 g, 10 min) and applied onto a Superdex 200 Hi-load16/60 column (4°C; Amersham/GE Healthcare). The protein monomer fractions were pooled and concentrated by 30 kDa molecular weight cut-off ultrafiltration (4°C; Centripreps, Millipore). The BF concentration was assayed photometrically, relying on an extinction coefficient of $\epsilon^{1\%} = 5.3$ at 280 nm.⁹⁰ Aliquots of purified protein were frozen in liquid nitrogen and stored at -20°C until use. A membrane with a pore size of 0.2 μm was used to filter all stock solutions.

The mineralization mixes were prepared according to Table 4.1 at room temperature and then adjusted to the incubation temperature as mixing the stock-solutions already at the incubation temperature had no effect (see results). Mineralization was always started by adding CaCl_2 solution to the freshly prepared mix.

Table 4.1: Scheme of CPP preparations depicting the combinations of fetuin-A concentration, supersaturation and temperature. At high mineral ion concentrations the supersaturation σ (or chemical driving force) can be written: $\sigma = \ln(I/K_{sp})$ with the ion product $I = a(\text{Ca}^{2+})^5 a(\text{PO}_4^{3-})^3 a(\text{OH}^-)$, the ion activity $a = \gamma c$, the activity coefficients at physiologic ionic strength⁹¹ $\gamma(\text{Ca}^{2+}) = 0.36$, $\gamma(\text{PO}_4^{3-}) = 0.06$ and $\gamma(\text{OH}^-) = 0.72$ and the solubility product of hydroxyapatite⁹² $K_{sp}(\text{Ca}_5(\text{PO}_4)_3\text{OH}) = 2.35 \cdot 10^{-59} \text{ M}^9$.

Bovine Fetuin-A (Sigma) [μM]	CaCl_2 (Roth, Germany) Na_2HPO_4 (Merck, Germany)	Buffer	Incubation Temperature [K]
7 - 75	Low supersaturation (LS): 5 mM CaCl_2 , 3 mM Na_2HPO_4 , $\sigma \approx 26$ High supersaturation (HS): 10 mM CaCl_2 , 6 mM Na_2HPO_4 , $\sigma \approx 32$	50 mM Tris pH 7.4 (AppliChem, Germany), 140 mM NaCl (Roth, Germany)	296 - 310

4.1.2.2 Three dimensional cross correlation Dynamic Light Scattering (3D-DLS)

Multiple scattering in solutions with high particle density prevent a characterizations by standard dynamic light scattering methods. Therefore we used a 3D cross correlation dynamic light scattering (3D-DLS) setup for the analysis of turbid calciprotein particle (CPP) samples.^{38,93,94} Measurements were performed using a standard light scattering device (ALV GmbH, Langen, Germany) with He-Ne-laser (JDS Uniphase, KOHERAS GmbH, 632,8nm,

25mW, Type LGTC 685-35), two avalanche photo diodes (Perkin Elmer, Type SPCM-AQR-13-FC) and an ALV 5000 correlator. Scattered light was detected at 90° geometry. The sample temperature was adjusted by an external thermostat equipped with a Pt-100 temperature sensor. The hydrodynamic radius R_h was calculated from second order cumulant fits via the Stokes Einstein equation. Measurements covered a time span of 1400 minutes in 2 minute intervals. Previous TEM investigations revealed that aged, secondary CPPs have an ellipsoidal shape with an axes ratio of approximately $b/a \approx 0.3$. For the sake of clarity, we calculated the hydrodynamic radii, not the semi-axes, to characterize the individual CPP stages.

4.1.3 Results and Discussion

4.1.3.1 CPP Detection by time-resolved 3D-DLS

The present study elucidates the fundamentals of CPP formation and ripening under controlled conditions *in vitro*. CPP kinetics largely depend on three modulators: BF concentration, calcium and phosphate ion supersaturation and temperature. We quantified their individual effects by time-resolved measurements of CPP growth using 3D cross correlation dynamic light scattering (3D-DLS).

Without any inhibitor, the induction of a supersaturation with regard to calcium and phosphate ions resulted in spontaneous mineral formation. Large particles in the micrometer range were immediately detected by 3D-DLS and within a few minutes mineral sedimentation was visible to the naked eye (data not shown). In contrast, bovine fetuin-A (BF) addition inhibited this sedimentation process by mediating the formation of spherical protein-mineral particles, so called calciprotein particles (CPPs).³ A series of CPP ripening experiments depicted in Figure 4.1 is illustrating the principal effects of temperature and BF concentration on CPP formation and ripening: Initial CPPs form within a second after the mineralization start.²⁶ As the solutions were first mixed outside and then inserted into the apparatus, only fully developed particles were detected by DLS. After a lag period, the initially formed primary CPPs spontaneously transformed to larger secondary CPPs. While the two stages corresponding to primary and secondary CPPs were both characterized by nearly constant particle sizes, the short intermediate transformation period (grey shaded area) showed fast and continuous particle growth. Irrespective of the exact conditions CPP ripening is always characterized by a biphasic time course (Figure 4.1). Analogous biphasic patterns have been described previously by time-resolved DLS, SANS, turbidimetry and ion quantification.^{3-5,70}

In this study, we focus on the stability of each CPP stage. A comparison shows that the long-term inhibition of mineral deposition is mainly associated with the secondary CPPs. An increase in temperature accelerates the process causing a shift of the transformation period to earlier time points (Figure 4.1, 296 K vs. 310 K) while the CPP radii were marginally affected.

Regarding the influence of the BF concentration, 7 μ M BF proved to be the threshold concentration under HS conditions (see methods) where the inhibition of mineral sedimentation was barely sustained. At this concentration, the transformation period ended in an apparent “growth-overshoot” which was probably due to the formation of some larger particles that subsequently sedimented. At higher protein concentrations, the

transformation period showed continuous particle growth until the second plateau corresponding to the size of secondary CPPs was reached.

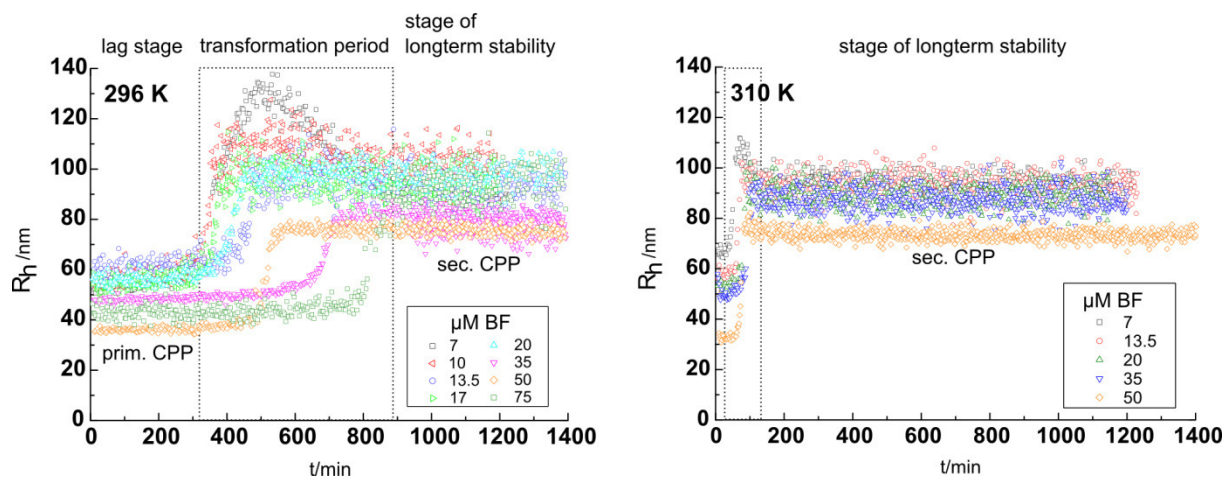


Figure 4.1: CPP ripening of individual samples at 296K (left) and 310K (right) analyzed by time-resolved 3D-DLS measurements. The complete statistical analysis of all samples is included in the supplemental information. All samples were adjusted to high supersaturation conditions (HS, see methods). Initial CPPs are only transiently stable. After a lag period, a transformation process indicated by rapid particle growth was observed (dotted contours). The emerging secondary CPPs proved to be long-term stable, i.e. no further growth or aggregation. An increased reaction rate at higher temperatures is mirrored by a shift of the transformation period to earlier time points. In control experiments without fetuin-A, large micrometer-sized particles were detected immediately (not shown).

In control experiments, we investigated the effect of temperature on the initial step of CPP formation by comparing samples that were first mixed at room temperature and then heated to the incubation temperature versus samples that were mixed at the incubation temperature. We found that the fast formation of the primary CPPs was insensitive to temperature as no difference regarding the subsequent evolution of particle size was observed.

A comprehensive particle size analysis is depicted in Figure 4.2 (see also Figure 6.1 and Table 6.2). Increasing fetuin-A concentrations led to smaller primary and secondary CPPs. Under high mineral ion supersaturation (HS) conditions, CPPs tended to be smaller than under low supersaturation (LS) conditions. Secondary LS-CPPs were particularly large (Figure 4.2, open squares).

The present 3D-DLS measurements do not provide any quantitative information on the effect of protein and ion concentrations on CPP composition and CPP number density. Variations in the composition of the system may affect particle formation and ripening. However, the small variations in CPP size suggest only minor structural changes in the CPPs (Figure 4.2 and Figure 4.3, Table 6.2).

Decreasing the fetuin-A concentration and increasing the mineral supersaturation both accelerated the ripening process without greatly affecting the CPP size. As expected, increasing temperatures also accelerated the ripening process while the CPP size did not change suggesting that the mechanism of CPP ripening was not affected.

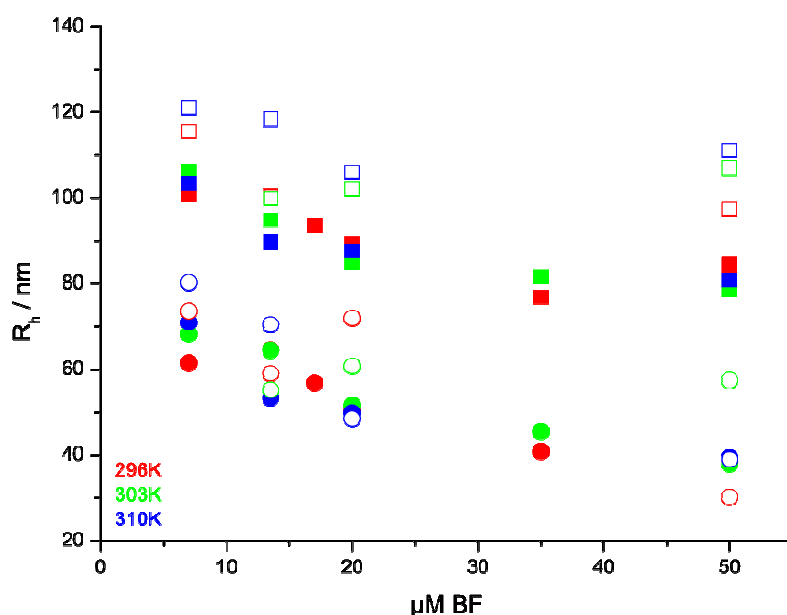


Figure 4.2: Hydrodynamic radii of primary (CPP1, circles) and secondary (CPP2, squares) calciprotein particles as a function of the BF concentration. CPP sizes were studied at three temperatures (296, 303 and 310 K corresponding to 23, 30 and 37°C) and two mineral ion concentrations (HS filled symbols, LS open symbols, see methods). More details are provided in the supplemental information.

4.1.3.2 Modulators of CPP Ripening

The transformation period is a characteristic feature of CPP ripening that can be detected easily by scattering methods. In particular, the CPP transformation half-time t_{trans} is a measure of the reaction rate derived from the scattering patterns (scheme in Figure 4.3) and plotted as a function of the BF concentration (Figure 4.3). At constant temperature, an increase in BF concentration generally resulted in an increasingly delayed t_{trans} until a plateau was reached. In contrast, an increase in temperature and in mineral ion supersaturation, respectively, both accelerated the reaction (reduced t_{trans}).

4.1.3.3 Kinetic Analysis

The inverse correlation of t_{trans} and temperature (Figure 4.3 and Table 6.3) was subjected to a kinetic analysis according to the Arrhenius law $k = A e^{-E_a/RT}$. In Figure 4.4 the logarithmic rate constant $\ln k = \ln(1/t_{\text{trans}})$ was plotted as a function of the inverse temperature $1/T$. Here, the activation energy E_a is proportional to the slope of the regression $\ln k = \ln A - E_a/R \cdot 1/T$. Table 4.2 lists the data derived from the Arrhenius kinetic analysis. We found that E_a tended to be higher under HS conditions, than under LS conditions. This observation may be due to a higher nucleation rate under HS conditions which may result in slightly smaller and probably less ordered primary CPPs. Similar values for E_a have been assessed for diffusion processes involving a structural rearrangement like the conversion from amorphous calcium phosphate to hydroxyapatite.⁹⁵

In conclusion, changes in temperature affected the rate of the CPP ripening but did not change the final CPP size. Lower temperatures neither affected the CPP size nor was CPP aggregation to larger entities ever observed. This is an important finding for future studies showing that it is safe to perform investigations at temperatures other than body temperature. For example, much simpler instrumental setups are possible if a thermostat is dispensable (i.e. room temperature). By cooling the sample it will be feasible to slow down

the ripening process in order to study certain aspects at higher resolution, like the CPP transformation period.

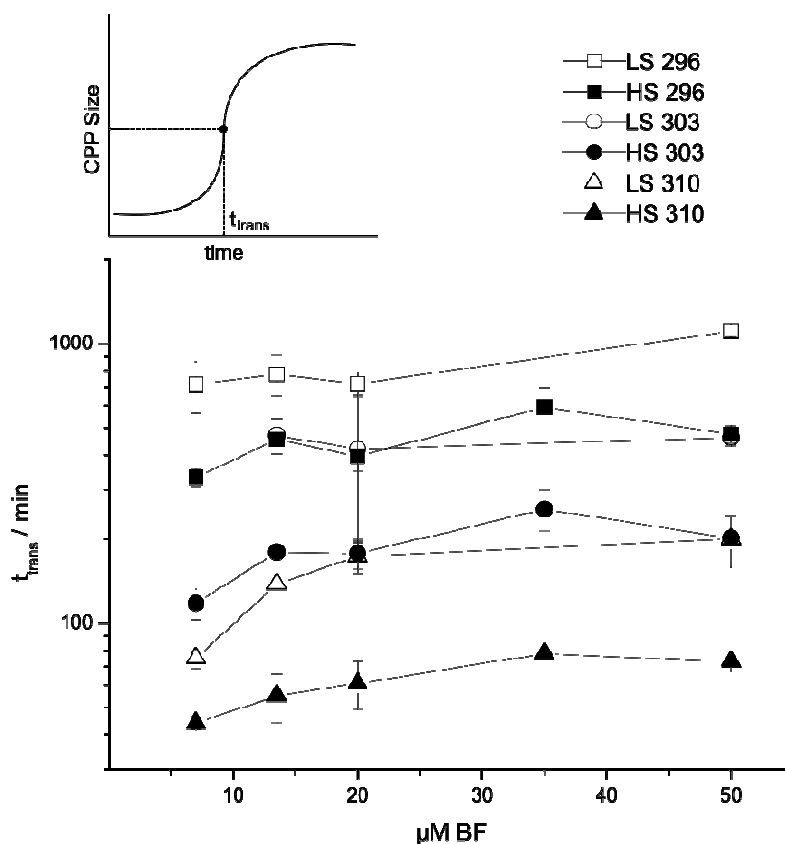


Figure 4.3: CPP transformation half-time t_{trans} plotted as a function of BF concentration at three temperatures (296, 303 and 310 K) and two supersaturation conditions (HS: filled symbols, LS: open symbols). A logarithmic presentation of t_{trans} was chosen for the sake of clarity.

Heating the sample above 37°C reduced the stability of the primary CPP, i.e. the transformation half-time shifted from ~ 778 minutes to 13 minutes at 50°C and to 7.5 minutes at 61.5°C (13.5 $\mu\text{M BF}$, LS), respectively. Both transformation half-times are in good agreement with the kinetic analysis (Figure 4.4 and Table 4.2). Fetuin-A denatures at 59.5°C.⁹⁶ Below this temperature, CPP2 size was not affected: $R_h \approx 102$ nm at 23°C, 118 nm at 37°C and 113 nm at 50°C. Above 60°C an increase in CPP size was observed, which was probably due to the decreasing protein stability. At 75°C, no primary CPP could be detected anymore and we assessed a CPP2 radius of $R_h \approx 175$ nm. Mineral sedimentation slowly commenced within 3.5 hours of incubation, suggesting that full long term stability was not attained.

Table 4.2: Energies of CPP transformation calculated from the slope of the Arrhenius plots shown in Figure 4.4. The ordinate intercept corresponds to logarithm of the pre-exponential factor A.

BF [μM]	Ea [kJ/mol]		ln A	
	LS	HS	LS	HS
7	-	108 \pm 0.5	-	34 \pm 0.2
13.5	83 \pm 29	98 \pm 2	23 \pm 12	30 \pm 1
20	77 \pm 2	98 \pm 12	21 \pm 1	30 \pm 5
50	93 \pm 1	109 \pm 8	27 \pm 0.3	34 \pm 3

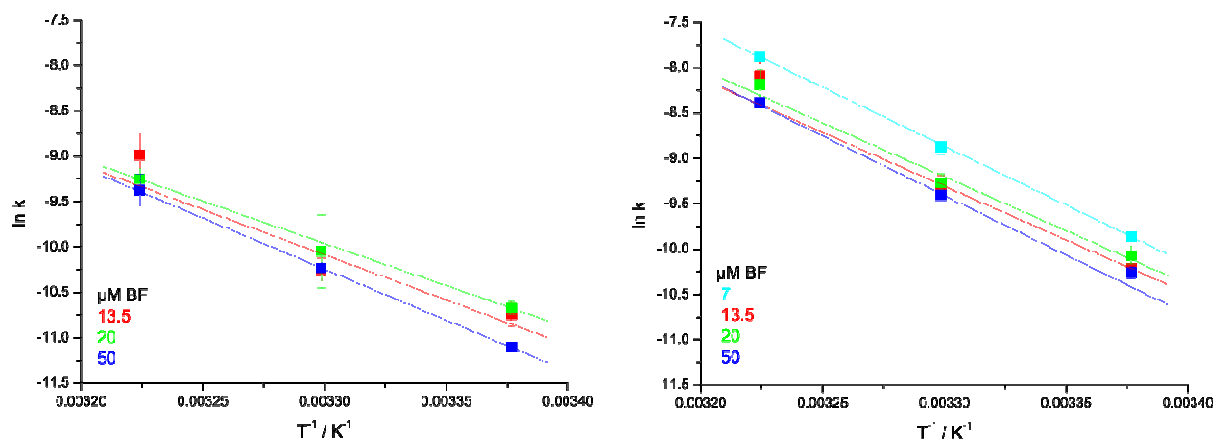


Figure 4.4: Arrhenius plots of CPP ripening kinetics at concentrations between 7 and 50 μM BF, left: low supersaturation (LS) conditions, right: high supersaturation (HS) conditions.

4.1.4 Conclusion

CPP formation and ripening is determined by mineral nucleation, fetuin-A mediated coalescence to CPPs, particle growth and phase transformation. Table 4.3 summarizes the data, depicting the general trends of each parameter regarding transformation half time and CPP size.

Table 4.3: Effect of the parameters (see Table 6.2 and Table 6.3) tabulated as general trends (\uparrow increase, \downarrow decrease, \approx no statistically significant difference).

Increase of	Transition Time	R_h (CPP1)	R_h (CPP2)
$c(\text{Fetuin-A})$	\uparrow	\downarrow	\downarrow
Supersaturation	\downarrow	\downarrow	\downarrow
Temperature	\downarrow	\approx	LS: \uparrow , HS: \approx

(I) Fetuin-A and mineral ion concentration both affected CPP size and rate constant (while previous studies suggested that the CPP morphology is basically not affected) and greatly differs from calcium phosphate particles grown in the absence of fetuin-A.³⁻⁵ Thus, at concentrations above the stability threshold, fetuin-A guides CPP formation and ripening. (II) Incubation temperature greatly affected the rate constant while it had a statistically significant size effect only on secondary CPPs under LS conditions. Besides, the temperature of the stock solutions before mixing had no effect on CPP size. This finding matters regarding the relevance of an abstract model system in comparison to mineralization processes in vivo where especially the temperature effect has always been an issue. It indicates that the mechanism basically remains unaltered and that CPP formation and ripening are two distinct processes. (III) We conducted a kinetic analysis according to Arrhenius law. E_a tended to be lower under LS than under HS conditions. Primary CPPs generated under HS conditions are probably less ordered than CPPs generated under LS conditions. Consequently, transformation to secondary CPPs may involve more extensive structural rearrangements resulting in a higher E_a under HS conditions. (IV) No secondary effects like CPP aggregation were observed under any given condition.

Our study provides elemental insights regarding the principles of fetuin-A mediated inhibition of mineral deposition which will help prospectively to assess the best experimental conditions, to evaluate particle sizes or to optimize the stability of organic – mineral colloids. For instance, it may be applicable in the design and synthesis of organic – inorganic hybrid materials⁹⁷. Furthermore, a profound understanding of the principles of protein - mineral interaction and colloid stabilization holds promise for advanced clinical approaches, like diagnostics or therapies to improve the health status of calcification sensitive patients, as well as for applications in bionanotechnology.

4.2 Determination of Fetuin-A Shape and Structure

4.2.1 Introduction

Fetuin-A (in literature also named α 2-Heremans-Schmid (HS) glycoprotein) is known to act as inhibitor of ectopic calcifications.² Its hydroxyapatite binding affinity is already known since 1978²² while its ability to inhibit the hydroxyapatite formation was shown first in mineralizing calvaria cells by Schinke et al.¹⁶ in 1996. The significant role of fetuin-A in the prevention of calcification was finally proven by Schäfer et al. in 2003.²

Two underlying and simultaneously occurring mechanisms have been identified in the context of the prevention of ectopic calcifications. The longer known process of the formation of calciprotein particles (CPPs) described in various publications^{3–5,7,26,27} is known since 2003. The second, complementary occurring mechanisms of long-term mineral stabilization in form of the formation of calciprotein monomers (CPMs) was discovered in 2010.²⁷ Those investigations showed that fetuin-A monomers stabilize subnanometer-sized clusters of coalesced mineral ions reminiscent of Posner-Clusters in addition to the stabilizing process in terms of CPP formation. Posner Clusters are tiny calcium-phosphate clusters that have been proposed as mineralization precursors and building blocks of amorphous calcium phosphate.^{28,29} Hence, fetuin-A is of utmost importance for the stabilization of calcium-phosphate and therewith in the prevention of unwanted mineralization. Beyond that, fetuin-A exhibits further biological relevance⁷ such as in the context of metabolic syndrome^{98–101} or regarding its anti-inflammatory effect^{102–107}.

The liver-derived serum protein fetuin-A belongs to the cystatin superfamily⁸ and was described in literature for the first time¹ in 1944. It is highly expressed in the fetus.¹¹ In the adult organisms it is predominantly present in serum, liver, bone and teeth.^{12–15} Human fetuin-A is a 349 amino acids protein with an additional 18 amino acids signal-peptide and an overall molecular weight of about 50 kDa.^{17,18} It undergoes several posttranslational modifications such as glycosylation^{19,20} and phosphorylation²¹. The functional protein is a monomer consisting of three domains of which two are cystatin-like (domains D1 and D2) and the third is rich in proline (domain D3). Domain D1 is known to be the most important domain with regard to calcification inhibition as it mediates the binding to basic calciumphosphate.^{3,16}

Altogether, structural details as well as structure-function relations of the native fetuin-A in solution are poorly understood. This is due to the high amount of glycosylations present at the fetuin-A molecule making conventional structure determination rather difficult.^{18,19,108–110} A first approach using homology protein structure modeling has been described by A. Heiss in 2002.¹¹¹ With this method it was possible to model in particular the tertiary structures of fetuin-A domains D1 and D2. The structure and function of domain D3 as well as the quaternary fetuin-A structure could not be elucidated in detail so far.

In the last years, a new approach has been developed and optimized by Svergun et al.^{112–116} which provides the opportunity of protein shape determination using SAXS with subsequent modeling on the basis of a simulated annealing approach. This method has been successfully applied in various cases to elucidate protein structures, structural changes and interactions.^{113,117–121} The method relies on the analysis of scattering curves from a (monomeric) protein solution using ab initio modeling. Established substructures of the

protein can be considered in the process of data evaluation.¹²² Hence, subsequent combination of the tertiary structures determined by homology protein structure modeling¹¹¹ with the experimentally determined shape of fetuin-A can provide further insight into the native structure of fetuin-A in solution.

Up to now the consideration of glycosylations for model-building was hardly possible. The glycosylations are flexibly orientated on the protein-surface causing time- and particle-dependent fluctuations in the protein-shape. This influences the ensemble-signal collected in a SAXS experiment and complicates data interpretation. However, recent developments aim in the direction of enabling the consideration of glycosylations for structure determination. This will make the method more feasible for highly glycosylated proteins such as fetuin-A.

A possible shape change of fetuin-A in the presence of calcium and/or phosphate is of great interest in order to understand the fetuin-A mediated formation of CPPs. A potentially occurring change in fetuin-A shape in the presence of mineral can also be accessed using SAXS with subsequent *ab initio* modeling as described before. This knowledge can help to elucidate the structure-function relation as it is known that the inhibitory effect of fetuin-A is in close connection to its native 3D structure.¹⁶

4.2.2 Experimental

The fetuin-A purification was performed by Steffen Gräber in the group of Prof. Jahnen-Dechent at RWTH Aachen University.

4.2.2.1 Common Fetuin-A Preparation

Lyophilized bovine fetuin-A (Sigma-Aldrich Co., Germany, F2379)¹⁷ was dissolved in Tris-buffered saline (TBS), filtered (pore size 0.45 μ M) and applied onto a Superdex 200 Hi-load16/60 column (4°C; Amersham/ GE Healthcare Europe GmbH, Freiburg, Germany). The protein monomer fractions were collected and concentrated using ultrafiltration with a molecular weight cut-off of 30 kDa (4°C; Centripreps, Merck Millipore KGaA, Darmstadt, Germany). Concentrations were determined photometrically, assuming an extinction coefficient of $\epsilon^{1\%}(280\text{ nm})=4.5$.¹²³

The fetuin-A solution was shock-frozen in nitrogen in aliquots of 1 ml and stored in the freezer. Samples were transported to the beamline on dry ice and defrosted directly before measurement.

Fetuin-A was either measured in a pure TBS buffer or in a mineral-containing TBS buffer. The fetuin-A concentrations varied between 2 and 20 g/l. Ca^{2+} was added in concentrations of 2.5 mM, 5 mM or 10 mM, respectively. PO_4^{3-} was added in concentrations of 1 mM, 3 mM and 6 mM, respectively. Additionally, the low concentration combination of both minerals was used.

4.2.2.2 Enhanced Fetuin-A Preparation in order to receive absolute monomeric Fetuin-A

Lyophilized bovine fetuin-A (Sigma-Aldrich Co., Germany, F2379)¹⁷ was dissolved in a phosphate buffer containing 10 mM PO_4^{3-} and 140 mM NaCl as well as a protease inhibitor („Complete Mini“ protease inhibitor-mix, Roche Diagnostics, Mannheim, Germany) and applied onto a Superdex 200 10/30 column (4°C; Amersham/ GE Healthcare Europe GmbH,

Freiburg, Germany). The protein monomer fractions were collected and in part concentrated using ultrafiltration with a molecular weight cut-off of 10 kDa (Vivaspin 500, Sartorius AG, Göttingen, Germany) to ratios of 1:2, 1:5 and 1:10. Concentrations were determined photometrically, assuming an extinction coefficient of $\epsilon^{1\%}(280\text{ nm})=4.5$.¹²³

The fetuin-A solutions were transported to the beamline in a cooled environment. On-site, samples were stored in the fridge until measurement. Before each measurement, concentrations were determined again using absorption measurement at 280 nm on a nanodrop spectrophotometer (NanoDrop 1000, Thermo Fisher Scientific Inc.). The determined concentrations were averaged from both measurement methods.

4.2.2.3 Small-Angle X-Ray Scattering Measurements and Data Processing

Data were collected at the BioSAXS beamline X33 of the European Molecular Biology Laboratory (EMBL) at DORIS III ring of the Deutsches Elektronen-Synchrotron (DESY) in Hamburg using an automated sample changer and standard procedures. Sample volumes of 60 μl were used. Measurements were performed with a wavelength $\lambda = 0.15\text{ nm}$. Data were recorded on a 2D photon counting Pilatus 1M-W pixel X-ray detector with a pixel size of 0.172 mm, a useful area of 67 x 420 mm² and a frame rate of 3 ms at a sample to detector distance of 2.7 m. This setup provided a q-range between $q_{\text{min}} = 0.06\text{ nm}^{-1}$ and $q_{\text{max}} = 6\text{ nm}^{-1}$.

Data were normalized to the storage ring current. Buffer background was measured both before and after each sample. The averaged background was subtracted from the sample scattering afterwards. Absolute calibration was performed using a reference solution of bovine serum albumin (BSA) with known concentration ($c \approx 5\text{ mg/ml}$). The molecular weight of fetuin-A in solution was estimated by comparison of the fetuin-A forward scattering with that from the BSA reference:

$$MM_P = I(0)_P / c_P \frac{MM_{St}}{I(0)_{St} / c_{St}} \quad (4.1)$$

where $I(0)_P$ and $I(0)_{St}$ are the scattering intensities at zero angle of the studied protein and the standard protein (BSA), respectively. c_P and c_{St} are the corresponding concentrations, MM_{St} is the molecular mass of the standard and MM_P is the molecular mass of the protein (fetuin-A).¹²⁴

The forward scattering $I(0)$ and the radius of gyration R_g were evaluated using the Guinier approximation (compare section 3.4.4.1). Those parameters were automatically calculated and computed for all samples.^{125,126}

4.2.2.4 Ab Initio Shape Determination

The fetuin-A shape in solution was reconstructed by Clement Blanchet from the Svergun group at EMBL, Hamburg, from SAXS data using the ab initio program DAMMIF.¹¹⁵ The program permits rapid ab-initio low resolution shape determination of randomly oriented particles (such as proteins) in solution from SAXS data. The protein is represented by a large number of densely packed beads within a search volume with sufficient size. Shape determination using DAMMIF is based upon a simulated annealing approach starting with an arbitrary particle shape. In the course of computation, the deviation of the theoretical scattering pattern of the bead particle from the experimental scattering pattern is minimized. When the theoretical scattering pattern of the protein model fits the experimental data best

possible, the result of the approach is a compact, interconnected low resolution protein shape model. Further details concerning the implemented algorithm can be found in the work of Franke and Svergun.¹¹⁵

The result is not unique, which is inherent to the fitting approach on the basis of simulated annealing. Therefore, several ab initio models were generated. Subsequently, both the most typical model as well as the average model were calculated using the program DAMAVER.¹²⁷

4.2.2.5 Rigid Body Modeling

Rigid body modeling was performed in order to elucidate the spatial arrangement of the fetuin-A substructures. The quarternary structure of fetuin-A was modeled by Clément Blanchet at EMBL, Hamburg, using the rigid body modeling program SASREF.¹²² Within the program algorithm, simulated annealing is employed to optimize the spatial arrangement of known substructures in a complex against experimental SAXS data. For that purpose, the subunits are selected and randomly moved in an arbitrary direction followed by a random rotation. This procedure is repeated until the deviation between theoretical and experimental scattering pattern does no longer decrease. SASREF provides a model of interconnected subunits under avoidance of sterical clashes. Details concerning the implemented algorithm can be found in the publication of Petoukhov et al.¹²². A final combination of the models received from ab initio modeling and rigid body modeling provides an improved overall model of the investigated protein in solution.

In the present case, models of the N- and O-glycosylations as well as their position in the primary structure of fetuin-A have been considered just like the domain models developed by Alexander Heiss.¹¹¹

4.2.3 Results and Discussion

4.2.3.1 Small-Angle X-Ray Scattering of commonly purified Fetuin-A

In a first approach, fetuin-A was measured at different concentrations in TBS. The received scattering curves are shown in Figure 4.5. All scattering curves show the same characteristics. With increasing fetuin-A concentration the noise of the values in a q-range above $q = 1 \text{ nm}^{-1}$ becomes less pronounced due to better statistics.

Determination of the Molecular Mass

The forward scattering of the sample can be utilized for the determination of the molecular mass. The measured data are comparatively noisy in the range of low and high q-values for low fetuin-A concentrations. Taking that into account, the calculation of the molecular mass was performed on the basis of the scattering intensity of $c = 10.12 \text{ g/l}$ fetuin-A in TBS using the calibration with BSA as standard protein. From those data, the molecular mass of fetuin-A was calculated with $MM_{\text{fetuin-A}} = 32.3 \text{ kDa}$ which is clearly below the value of approximately 50 kDa ^{17,18} determined with ultracentrifugation and sedimentation studies, respectively. The obtained value was checked in the course of modeling as shown below.

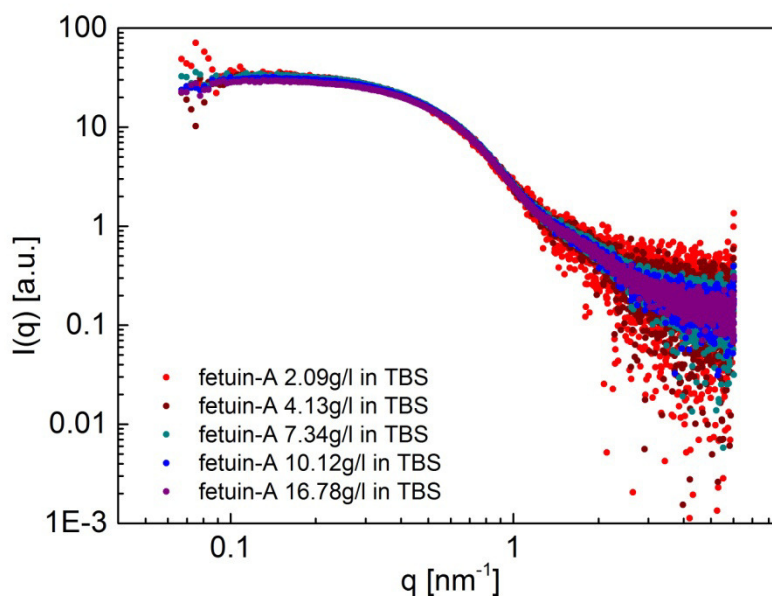


Figure 4.5: Scattering curves of fetuin-A in different concentrations in TBS. The scattering intensity is normalized to the storage ring current and the fetuin-A concentration. TBS scattering is subtracted.

Ab Initio Modeling

Ab initio modeling based on the experimental data shown in Figure 4.5 was done by Clement Blanchet and showed good agreement of fit and experimental data (data for 10.12 g/l fetuin-A in TBS are exemplarily shown in section 6.3). However, the volume computed from the fits provided a molecular mass of approximately 70-80 kDa which is significantly above the value of around 50 kDa determined in earlier studies using ultracentrifugation and sedimentation studies.^{17,18} Furthermore, the value differs clearly from the value of the molecular mass calculated from forward scattering. This result indicated the presence of larger molecules such as e.g. aggregates in the solution. Hence, rigid body modeling was performed and the resulting data were compared.

Rigid Body Modeling

The known substructures of fetuin-A¹¹¹ have been considered for rigid body modeling. In addition to the three independent models for domains D1 - D3, a combined model including D1 and D2 was used. The domain models are based upon the sequence of murine (D1 and D2) and human (D3) fetuin-A while the measurements were performed using bovine fetuin-A due to availability. Murine and bovine fetuin-A exhibit a homology of 63.2 % (alignment of bovine fetuin-A, P12763¹²⁸, and murine fetuin-A, P29699¹²⁹). Human and bovine fetuin-A exhibit a homology of 62.5 % (alignment of bovine fetuin-A¹²⁸, P12763, and human fetuin-A, P02765¹³⁰). The O-glycosylation sites are missing in the murine fetuin-A. Therefore, glycosyl chains were placed in close direction to the missing amino acids (close to amino acid position 271, 280 and 282)¹³¹ in the model. N-glycosylations are known to be attached to asparagine at positions 99, 156 and 176 in the bovine and murine fetuin-A.^{110,132-134}

A model of the N-glycosylations from Alexander Heiss based upon the work of Baenziger and Fiete²⁰ was used for rigid body modeling. The O-glycosylations are based on the sequence published by Spiro and Bhoyroo in 1974¹⁹, so that all necessary substructures could be

considered for rigid body modeling by Clement Blanchet. An overview of the models of all substructures is shown in Figure 4.6.

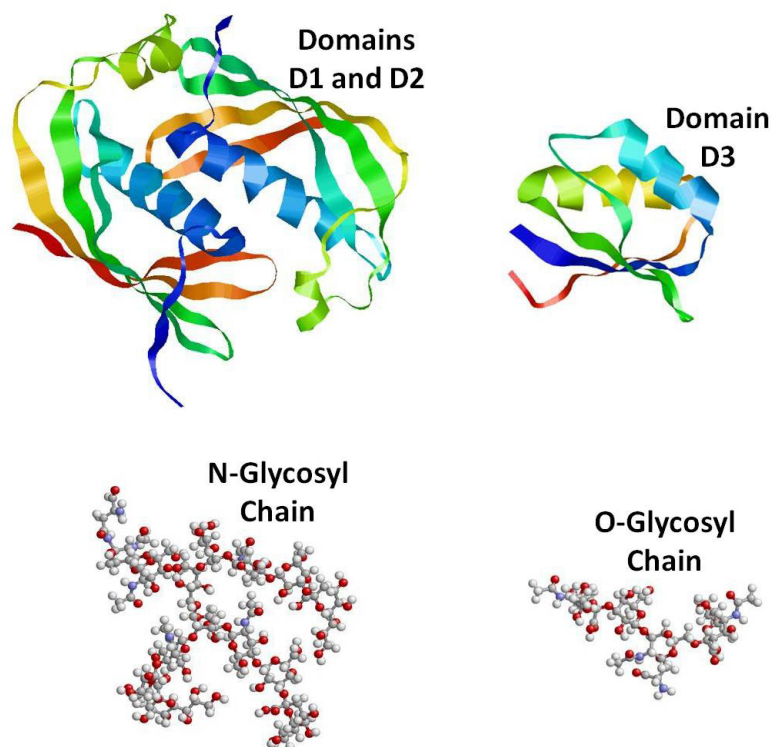


Figure 4.6: Substructures considered for rigid body modeling. Domains D1 and D3 are taken from the work of A. Heiss¹¹¹, the glycosyl chains are based on the work of Spiro et al.¹⁹ and Baenziger et al.²⁰.

Two different modeling approaches were used due to the inconsistency in the obtained molecular mass of fetuin-A and its molecular mass determined earlier^{17,18}: modeling of a monomeric structure and modeling of a dimeric structure. In both cases, fitting was performed with and without consideration of the glycosylations. The three domains were either considered independently or the combined model of domains D1 and D2 was used in combination with the model of domain D3.

The best fit results were obtained for the monomeric model with glycosylations. However, the obtained models were very flexible and contact between the substructures was partly missing. Moreover, fits of similar quality were obtained for the assumption of a dimeric model without glycosylations. Altogether, a reliable model could not be obtained.

Therefore, fetuin-A purification was improved and the scattering experiments were repeated with pure monomeric fetuin-A in order to receive better data for shape determination as shown in section 4.2.3.2.

4.2.3.2 Small-Angle X-Ray Scattering of Fetuin-A after enhanced Purification

The scattering pattern of pure monomeric fetuin-A was measured at different concentrations after refining the fetuin-A purification procedure. Data were collected in a buffer containing 10 mM PO_4^{3-} and 140 mM NaCl. The scattering curves and the respective fetuin-A solution concentrations are shown in Figure 4.7.

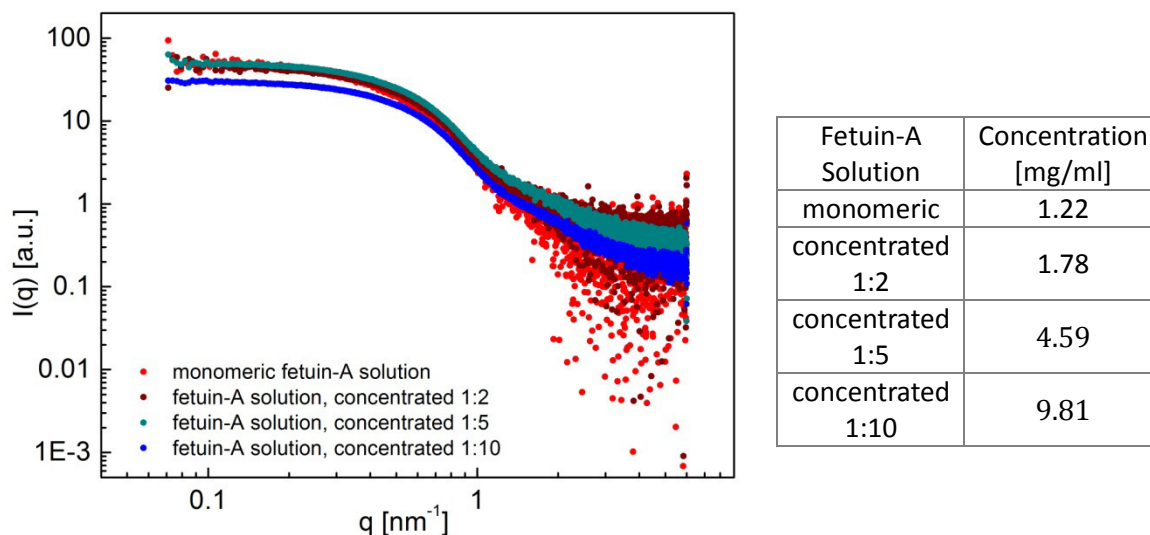


Figure 4.7: Left: Scattering curves of pure monomeric fetuin-A in different concentrations in a buffer containing 10 mM PO_4^{3-} and 140 mM NaCl. The scattering intensity is normalized to the storage ring current and the fetuin-A concentration. TBS scattering is subtracted. Right: Fetuin-A concentrations in solution.

The SAXS curves of the fetuin-A solutions with lower concentration coincide while the highly concentrated fetuin-A SAXS curve exhibits the same characteristics but lies below the other fetuin-A curves. This is probably due to an experimental error during data collection. Hence, this curve was not taken into account for further structure determination calculations. The remaining SAXS patterns were used to calculate low resolution models of the monomeric fetuin-A molecule.

Determination of the Molecular Mass

The molecular mass was automatically calculated during beamtime from forward scattering $I(0)$ of the fetuin-A at different concentrations. This approach provided values between $\text{MM}_{\text{fetuin-A}} = 53$ kDa and $\text{MM}_{\text{fetuin-A}} = 60$ kDa for fetuin-A concentrations between $c_{\text{fetuin-a}} = 1.22$ g/l and $c_{\text{fetuin-a}} = 4.59$ g/l. Hence, the values calculated from experimental SAXS data are consistent with former results determined with ultracentrifugation and sedimentation studies, respectively.^{17,18} The data were used to model the low-resolution three-dimensional fetuin-A structure in solution.

4.2.3.3 Fetuin-A Model from Experimental SAXS Data

The data set recorded from monomeric fetuin-A was used as basis for fetuin-A structure determination. Ab initio modeling as well as rigid body modeling was performed by Clement Blanchet.

Ab Initio Modeling

The typical model received from ab initio modeling is an envelope model of the investigated protein molecule. The most typical model obtained from ab initio modeling of the fetuin-A scattering data is shown in Figure 4.8.

The fetuin-A molecule exhibits a pear-like shape with a bulgy part and a smaller neck. The bulgy part of the ab initio model has dimensions of approximately 8 x 4.5 nm, while the neck

is approximately 5 nm long and 3 - 4.5 nm thick. The longest axis is approximately 10 nm long. Those values lie slightly above the values determined for the hydrodynamic radius with DLS in earlier studies⁵. The shown models are low-resolution models of the fetuin-A shape derived from the scattering of all molecules present in the detected volume, so-called envelope models. Thus, it is reasonable that the dimensions of the obtained envelope model lie slightly above the values determined with DLS.

From the model it is conceivable that the attachment to the mineral takes place in the “neck part” of the fetuin-A and therewith in a protected region towards the middle of the molecule rather than exposed on its surface. In a next step rigid body modeling was performed in order to elucidate the exact spatial distribution of the substructures and to check this hypothesis.

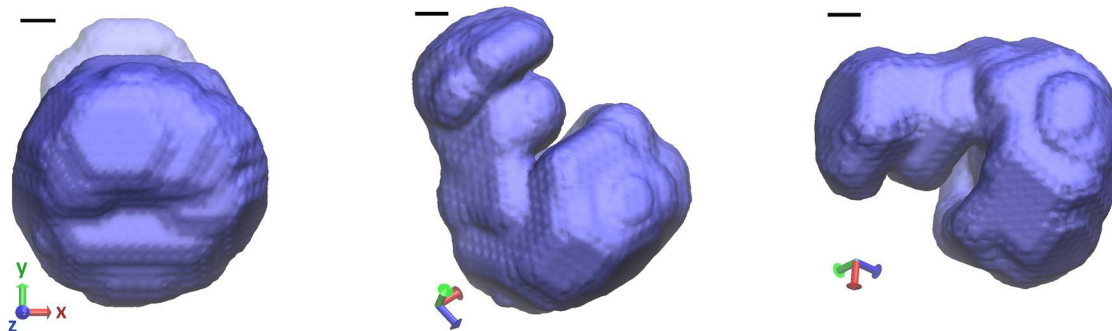


Figure 4.8: Fetuin-A low-resolution ab initio model (envelope model) calculated from experimental SAXS data. The scale bar is 1 nm.

Rigid Body Modeling

Rigid body modeling was used supplementary to the ab initio modeling to provide information on the spatial arrangement of the known substructures within the fetuin-A molecule. The established models of the three domains D1, D2 and D3¹¹¹ were used for this approach just like the models for the N- and O-glycosylations (see Figure 4.6).

The O-glycosylation sites are missing in the modeled domains from murine fetuin-A while they are present in the bovine fetuin-A measured in SAXS. For rigid body modeling, glycosyl chains were therefore placed in close position to the missing amino acids (close to amino acid position 271, 280 and 282¹³¹). The modeling of domain D3 had been performed on the basis of the primary sequence of human fetuin-A.¹¹¹ Similar to bovine fetuin-A, human fetuin-A is (partly) O-glycosylated in the region of D3 (amino acid position 341 in bovine fetuin-A¹³¹, amino acid position 346 in human fetuin-A¹³⁵), which was considered for modeling. N-glycosylations are known to be attached to asparagine at positions 99, 156 and 176 in bovine and murine fetuin-A^{110,132-134}, so that those positions were chosen as additional constraints for rigid body modeling.

A combination of the models obtained from ab initio modeling and rigid body modeling provides the best possible information on the fetuin-A molecule in solution. Thus, the spatial arrangement of the substructures obtained from rigid body modeling is shown together with the envelope function received from ab initio modeling in Figure 4.9. To the best of our knowledge, this is the first 3D structure model of the native fetuin-A in solution.

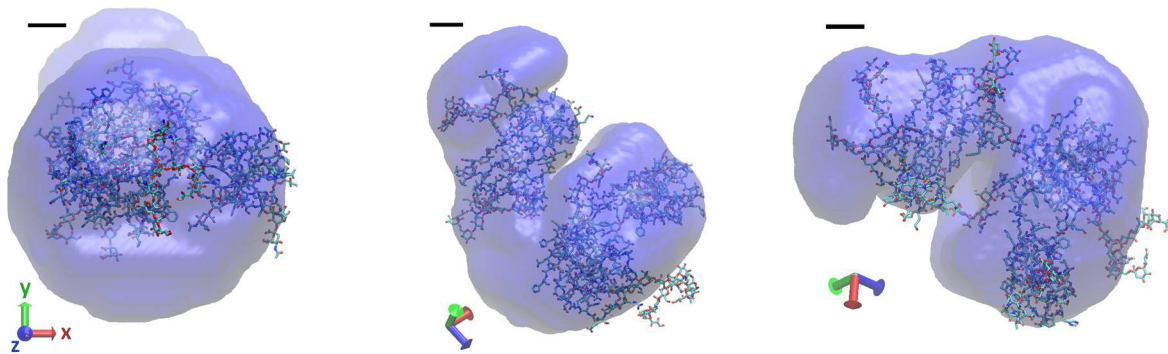


Figure 4.9: Fetuin-A low-resolution rigid body model calculated from experimental SAXS data. The scale bar is 1 nm.

The overlap of the envelope function and the rigid body model is clear but not perfect. On the one hand we assume that those deviations result from the scattering experiment itself. SAXS is an ensemble method. Hence, the scattering pattern includes the scattering of several protein monomers with different orientation. In the present case of research on glycosylated proteins, the existing glycosyl chains additionally contribute to the scattering signal. Thus, the information content included in the scattering pattern becomes more complex and extraction of information becomes more challenging. Furthermore, the fetuin-A used for modeling and measurements belongs to different species as described before. Thus, the fetuin-A molecules are not identical, which can also contribute to the imperfect overlap of the different models.

The contact between the glycosyl-chains and the protein body (consisting of the domains D1-D3) is only mediated via one amino acid in each case. Therefore, the connection is very flexible and the configuration of the glycosyl chains at the protein surface is variable both in time and among different proteins of the same species. This leads to variations within the three-dimensional structures of the protein monomers present in the detection volume. Those different structures are averaged by SAXS measurement just like the orientations of the protein monomers themselves. Hence, the SAXS signal becomes less unique with increasing protein concentration and increasing number of glycosyl chains, respectively. Thus, computation of a reliable structure model becomes increasingly complicated for higher glycosylated proteins.

However, the model provides important information concerning the spatial arrangement of the subunits of the fetuin-A molecule. While the domains D2 and D3 are located in the bulgy part of the pear-like fetuin-A, domain D1 forms the neck. Moreover, the model confirms earlier results from monoclonal antibody mapping (Willi Jahnke-Dechent et al., unpublished results) predicting the amino acids in the regions 265-275 and 302-320 to be turned towards the outside of the molecule. Those regions are found at the bottom of the pear-like fetuin-A structure. The domain D1, which is known to mediate the binding to hydroxyapatite^{3,16}, is located at the cavity of the molecule supporting the hypothesis of the mineral being bound at the protected region of the molecule. The rigid body model provides enough space for mineral being incorporated without considerably affecting the molecular structure.

4.2.3.4 Fetuin-A in Mineral Environment

SAXS patterns of commonly purified fetuin-A were measured in mineral environment, that is in the presence of Ca^{2+} , PO_4^{3-} or both, respectively, to investigate potentially occurring shape changes due to fetuin-A mineral interactions. The obtained scattering curves are shown in Figure 4.10.

All fetuin-A scattering curves show the same characteristics regardless of its environment. Fetuin-A is known to bind to apatite^{3,16} from previous investigations in cell culture and TEM analysis; this binding was found to be mediated by an array of acidic residues in domain D1.³ It was also shown that the binding is caused by fetuin-A interactions with calcium ions rather than with phosphate ions.¹⁶ Therefore, we hypothesized to see changes in the scattering curves of fetuin-A in the presence of Ca^{2+} or both minerals, respectively. However, experimental data do not match those expectations.

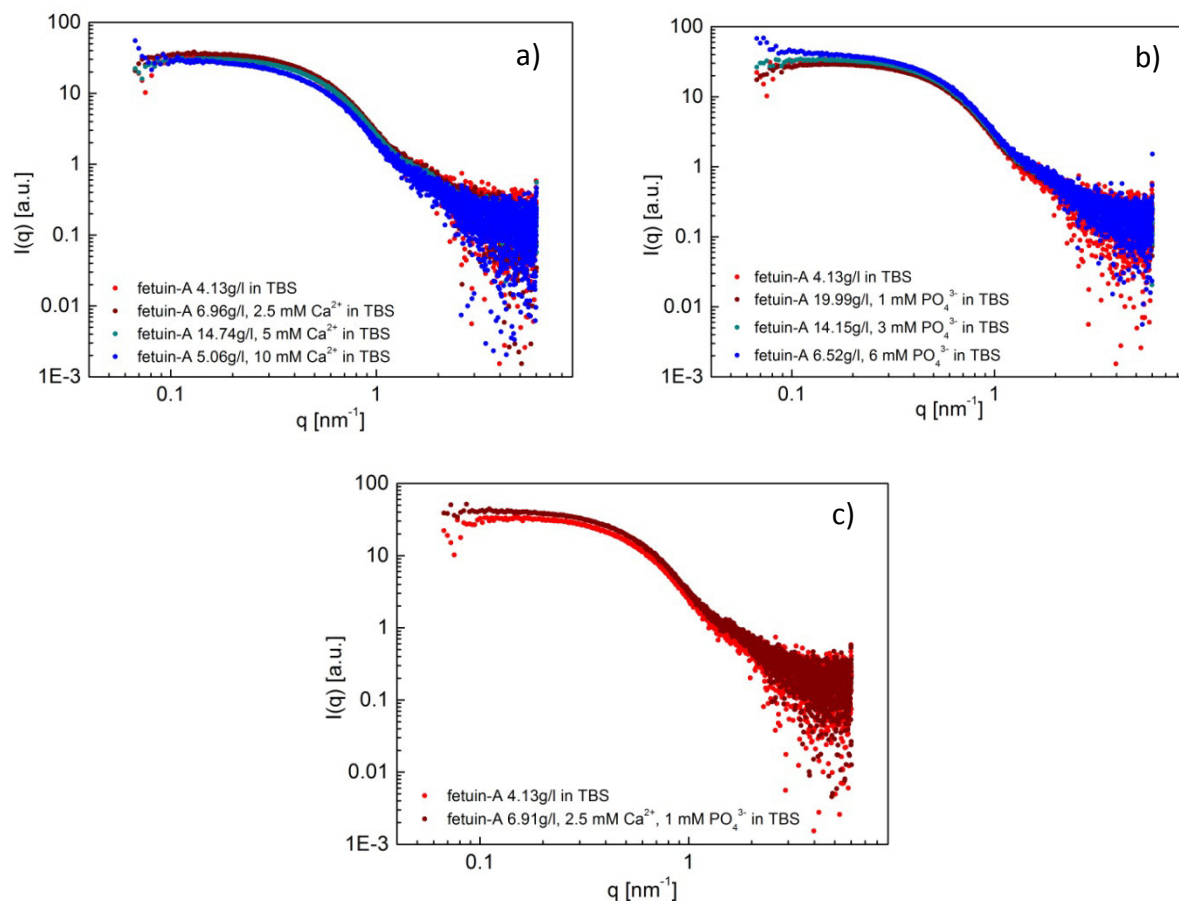


Figure 4.10: Scattering curves of fetuin-A ($c = 4.13$ g/l) in pure TBS compared to scattering curves of fetuin-A (in different concentrations) in TBS in the presence of a) Ca^{2+} , b) PO_4^{3-} or c) both minerals, respectively.

Previous SANS investigations on the role of fetuin-A in calcification inhibition have proven the binding of subnanometer sized mineral clusters reminiscent of Posner Clusters ($\text{Ca}_9(\text{PO}_4)_6$) to the fetuin-A molecule.²⁷ Those measurements were carried out in a similar environment as the measurements shown here. Thus, we assume that mineral binding also occurred in the present case. However, the characteristics of the scattering curves do not significantly change with changing environment.

The impact of the mineral presence on forward scattering cannot unambiguously be clarified from the obtained scattering data. Our data indicate that forward scattering of the sample does not change if only Ca^{2+} is present while an influence cannot definitely be excluded from the received scattering data in the presence of PO_4^{3-} or both minerals, respectively.

Heiss et al. found the fetuin-A calcium-binding capacity to be (15 ± 7) Ca^{2+} ions per fetuin-A molecule.²⁷ This corresponds to a mass increase of only approximately 1%. Thus, pronounced changes in forward scattering are not to be expected in the presence of Ca^{2+} even for the case that mineral uptake occurs. This is consistent with our results (see Figure 4.10 a)).

In the same work, the mineral binding capacity of a fetuin-A monomer was roughly estimated with up to (120 ± 20) Posner clusters.²⁷ A mineral uptake in this order of magnitude would lead up to a triplication in molecular weight. A slight increase in forward scattering can only be assumed due to the fact that the scattering data become increasingly noisy with decreasing q-values (see Figure 4.10 c)).

In case of the presence of PO_4^{3-} , scattering data at low q-values do not indicate a clear trend (see Figure 4.10 b)). Due to the fact that apatite binding of fetuin-A was found to be caused by fetuin-A interactions with calcium ions rather than with phosphate ions¹⁶, we hypothesized that no changes in forward scattering should occur. However, this cannot finally be excluded from the received scattering data.

The unchanged characteristics of the scattering curves additionally indicate that the shape of the fetuin-A molecule remains unchanged within the limits of measurement resolution although mineral binding occurs. Thus, we conclude that the clusters become incorporated in the fetuin-A structure so that mineral uptake can occur without considerable changes in the characteristics of the SAXS pattern of fetuin-A. This is in accordance with the results of previous SANS measurements which indicated that the mineral arranges in a random distribution around the protein core.²⁷

4.2.4 Conclusion

The present SAXS study provides the first 3D low-resolution structure of the native fetuin-A molecule in solution. Reliable data and structure information were obtained although fetuin-A belongs to a group of highly glycosylated proteins. The spatial arrangement of the subunits could be elucidated. The location of specific fetuin-A regions on the outside of the molecule expected from earlier monoclonal antibody mapping studies was verified.

Fetuin-A tends to form aggregates with higher molar mass. Hence, careful purification is necessary in order to investigate the monomeric fetuin-A in solution. Freezing of the fetuin-A solution obviously favors the formation of aggregates.

Fetuin-A measurements in mineral environment showed no changes in the characteristics of the experimentally accessible SAXS pattern. The experiments indicate that the mineral uptake is not accompanied by structural changes within the fetuin-A molecule. The exact impact of mineral uptake on the molecular weight of the protein remain to be clarified.

4.2.5 Outlook

The received structural information is inevitable for further investigations concerning the fetuin-A interaction not only with mineral but also with other molecule types such as lipids^{136–138}, lectin^{139–142} or proteinase^{143–147}. The model provides the necessary basis to elucidate the details of binding. Thus, it will help to clarify the fundamentals of CPP formation.

However, the structure model needs further refinement. It is necessary to calculate the domain models of bovine fetuin-A in order to receive consistent experimental and theoretical data of the same species. In this context, the model of domain D3 needs to be refined as it is least understood up to now. At the moment, the model of D3 is a homology model based on the cystatin structure.¹¹¹ Further knowledge especially of this domain is necessary and will help to improve the fetuin-A model. Moreover, SAXS data analysis is under continuous development. Improvements in the interpretation of SAXS data from glycosylated proteins will improve the fetuin-A model additionally.

4.3 The CPP Transition - A SAXS Study reveals Insight into Shape and structural Changes

4.3.1 Introduction

The fetuin-A mediated stabilization of calcium-phosphate as model system in the context of biomineralization is an important subject of ongoing research. Elucidation of the individual steps in fetuin-A mediated CPP formation and ripening is of great interest for further understanding of biomineralization processes and for the directed assembly of mineral particles with defined size and properties. The focus of the present research lies on the investigation of changes in the structural properties of the CPPs and their dispersity during transition. After investigation of the formation and stability kinetics of the CPPs¹⁴⁸ (see chapter 4.1) the next step is to understand the ongoing processes. Up to now it is known that the initially formed CPPs exhibit spherical shape. The transition into second state is accompanied by a change in size and shape of the CPPs, finally leading to ellipsoidal, needle-like particles as seen in TEM.⁵ Additionally, it could be shown that the process of transition itself remains unaffected by variations in calcium and phosphate supersaturation, fetuin-A concentration and temperature.¹⁴⁸ Those parameters simply influence the transition time.

The investigations on the kinetics provided the necessary information on how to control the process of CPP transformation. With that knowledge, parameters for subsequent investigations can be chosen best possible e.g. in order to obtain ideal time-resolution. For example, the transition process can be decelerated by lowering the temperature, which offers the possibility of enhancing the time-resolution in time-dependent measurements.

SAXS measurements were performed using a synchrotron source which offers the possibility of measuring time-dependently with a resolution of several minutes for further elucidation of the transition process. Questions concerning the fundamentals of the transition are addressed and occurring structural rearrangements are investigated.

In addition to the common measurement of the CPP samples in a capillary, measurements under flow conditions were performed. Therefore we capitalized on a characteristic feature of the CPPs: their different shape in first and second state. Application of a directed flow on a particle-containing solution can be used to force particles to align in flow direction. The enforced largely uniform orientation of anisotropic particles, that is second-state CPPs in the present case, will allow to determine their geometry with unprecedented accuracy using SAXS measurements. With this method, the CPP shape changes during transformation are directly accessible. The scattering intensity is isotropic for the spherical CPPs in first state while it is assumed to become anisotropic for the second-state CPPs. Time-dependent measurements can then elucidate structural rearrangements as well as changes in CPP dispersity during transition. The same method was also used to address the question whether the transformation of CPPs occurs at the same time for all particles or whether it is rather an independent process. An abrupt process induces anisotropy in the intensity at a moment's notice while an independent process leads to a slow change in intensity with time. The determination of the orientation distribution during transition can also help to clarify whether growth or an aggregation process is responsible for the transformation. For those measurements, a micro fluidics cycle was designed in the context of a master thesis in the group of Prof. Klemradt at RWTH Aachen University.¹⁴⁹

4.3.2 Experimental

4.3.2.1 CPP-Solution

CPP-solutions were prepared by mixing the following components: bovine fetuin-A (13.5 μM or 35 μM , respectively), 50 mM Tris, 140 mM NaCl, 6 mM Na_2HPO_4 and 10 mM CaCl_2 . CaCl_2 was always added as last component as its addition starts the process of CPP formation. All stock solutions were filtered (0.45 μm pore size) before use. Reaction mixtures were prepared in 1 ml-volumes to ensure perfectly homogenous mixing of all components. If more than 1 ml of total volume was necessary, several 1 ml reaction mixtures were prepared.

4.3.2.2 Basic Requirements and Design of Micro Fluidics Cycle for Dynamic Measurements

The micro fluidics cycle (*flow-cell*) used for CPP measurements was designed by Olivier De Castro in the context of his master thesis in the group of Prof. Klemradt at RWTH Aachen University¹⁴⁹ and applied at the synchrotron (BW4, DESY, Hamburg) in order to obtain time-dependent measurements of the CPP transformation with high resolution. In the context of the flow-cell design, basic principles of fluid dynamics were considered. The Reynolds number Re was considered in order to measure within the range of laminar flow conditions. It provides an important criterion for the differentiation between laminar and turbulent flows and is defined as

$$Re = \frac{\rho \cdot v \cdot d}{\eta} \quad (4.2)$$

where d is the characteristic length of the system (tube diameter in case of a flow through a cylindrical system), v is the average velocity in the flow field, ρ is the density and η is the dynamic viscosity of the fluid. Below a critical value Re_{crit} , the flow is laminar while the sensitivity to turbulences increases drastically when the critical value is exceeded. In the case of tube flows, the Re_{crit} is typically specified with $Re_{crit} = 2300$.¹⁵⁰ The pump was chosen such that velocities providing laminar flow could be achieved, that is Re was kept below 2300.

An additional requirement for particle alignment besides the laminar flow conditions is that the Brownian motion of the investigated particles is small compared to the forces acting due to the enforced flow. For the consideration of the ratio of advective processes (enforced flow) to diffusive processes (Brownian motion), a second characteristic number was considered during flow-cell design, which is the Péclet number. The Péclet number is defined as

$$Pe = \frac{v \cdot d}{D} \quad (4.3)$$

where D describes the rotational diffusion of the particles.

An exact calculation of the respective parameters, in particular the rotational diffusion coefficient and with that the Péclet number Pe was not possible. On the hand, this is due to the fact that the analytical determination of the rotational diffusion coefficient for particle types different from spheres is not directly possible.^{151,152} Hence, rotational diffusion coefficients are often determined experimentally, e.g. using depolarized dynamic light

scattering.^{153–155} At the moment the experimental determination of the rotational diffusion coefficient is not possible in case of the CPPs, which is due to the known challenges accompanying CPP investigation (especially the presence of CPMs in addition to the CPPs). Detailed knowledge on the exact composition of the CPP-solution or rather an independent analysis of stabilized CPPs would have been necessary for the determination of their rotational diffusion.

Furthermore, preferably the exact size or rather axial ratio of the CPPs is necessary as a comparison of theoretically and experimentally determined values for the rotational diffusion coefficient of gold colloids in a similar size range as the CPPs has shown the considerable influence of changes in the axial ratio on the rotational diffusion coefficient.¹⁵¹ In the case of those gold nanorods with a length of 45 nm, a decrease in the hydrodynamic radius from 22 nm to 11 nm (reduction of the axial ratio with 50 %) decreased the rotational diffusion coefficient with nearly 50 %. The calculations are based on a model describing the gold nanorods as sequence of equal spheres forming an elongated, rod-shaped particle as an analytical determination of the rotational diffusion coefficient was not possible.¹⁵¹

Altogether, knowledge of the exact dimensions or rather the exact axial ratio of the CPPs is inevitable in order to more exactly determine their rotational diffusion coefficient. Hence, an exact calculation of the parameters necessary for CPP alignment under flow conditions is currently not possible. However, the required parameters have been roughly estimated for the CPPs in order to design the flow-cell.¹⁴⁹ It was possible to estimate the necessary flow velocity for an alignment of the CPPs from the product of the local Reynolds number Re_l and the local Péclet number Pe_l . The detailed considerations in the context of the flow-cell design are described in the respective master thesis.¹⁴⁹

4.3.2.3 Micro Fluidics

The micro fluidics cycle used for CPP measurements under directed flow was designed and completed in the context of a master thesis in the group of Prof. Klemradt at RWTH Aachen University.¹⁴⁹ A closed cycle was used in order to minimize the necessary sample volume. The cycle consists of four main parts: a sample reservoir in form of a syringe, a pump allowing for defined flow velocities, a temperature-controllable sample cell and a temperature stabilization. The whole cycle was constructed metal-free to avoid adsorption of fetuin-A and the CPPs, respectively.

The used pump was a micro annular gear pump (mzr-2942-cp M2.1) in combination with the control device S-KG (both HNP Mikrosysteme GmbH, Schwerin, Germany). The pump driving speed was adjusted using a 10 k Ω potentiometer (model PC-16SH07IPO4, Piher International GmbH, Eckental-Brand, Germany).

The measurement cell consists of a copper sample holder with five slots for sample cells located perpendicular to the beam during measurement. In the case of the micro fluidics cycle, the sample cells are thin walled balloon formers made from borosilicate glass (Hilgenberg GmbH, Malsfeld, Germany). The smallest part of the used sample cell has a diameter of 0.6 mm, and a length of approximately 30 mm. The wall thickness is approximately 0.01 mm in the part that is irradiated during measurement to avoid radiation absorption and unwanted capillary scattering effects.

A temperature control and a system assuring heat exchange was used for temperature stabilization. Both parts were constructed in connection with the micro fluidics cycle by O. De Castro. The detailed description of the whole setup can be found in his master thesis.¹⁴⁹ All measurements were performed at $T = 297.15$ K unless otherwise noted.

4.3.2.4 Synchrotron SAXS Measurements

SAXS measurements were performed at the Deutsches Elektronen-Synchrotron (DESY) in Hamburg at HASYLAB (Hamburger Synchrotronstrahlungslabor) beamlines B1 (static measurements) and BW4 (flow measurements) of the DORIS III ring.

At B1, measurements were performed in mark-tubes made of glass no. 50 (80 mm length, 1.5 mm outer diameter, 0.01 mm wall thickness; Hilgenberg GmbH, Malsfeld, Germany). The sample holder was completely filled with five capillaries containing the physically same sample. Thus, it was possible to measure each capillary in turn in order to reduce beam exposure time and with that the risk of radiation damage. Measurements were performed at an energy of 8.9 keV. The beam diameter in the sample was 1 mm x 0.7 mm, the sample to detector distance was 3.583 m. Each measurement took 300 s or 600 s, respectively. A Pilatus 1M (Dectris Ltd., Baden, Switzerland) with 981 x 1043 pixels with a readout time of 3.6 ms was used as 2D-CCD-detector. All measurements were carried out in transmission mode.

At BW4, measurements were conducted under flow using a wavelength of $\lambda = 0.138$ nm. The beam diameter was 300 μm x 300 μm , sample to detector distance was 13.87 m. Scattering intensity was recorded 300 s for every scattering curve. A MAR165CCD (Marresearch GmbH, Norderstedt, Germany) with a maximum resolution of 2048 x 2048 pixels with a readout- and saving time of approximately 5 s was used as 2D-CCD-detector. Again, the measurements were carried out in transmission mode.

4.3.2.5 Data Evaluation

The detected SAXS intensities from static measurements were integrated q -dependently and normalized to the storage ring current. The integration was done in the context of a master thesis in the group of Prof. Klemradt at RWTH Aachen University.¹⁴⁹ Scattering of TBS (Tris-buffered saline) was subtracted for all measurements. Afterwards, the scattering curves were evaluated to receive information on CPP parameters (in particular size, shape and polydispersity). Data were collected throughout the whole process of CPP transformation, so that in principle a characterization of CPPs is possible for the first and second state and -most important- for the time of transformation. The most challenging task in SAXS is the data evaluation. The problem inherent to SAXS data is that necessary information becomes inaccessible due to the measurement of intensities (see section 3.4.1). The problem is known as inverse phase problem. Nevertheless, the developing of the scattering curve depends on particle dispersity, scattering contrast and the form factor describing the shape of the particles. Hence, fitting of the scattering curves can provide information on those parameters. In the present case, two different fitting routines were used to access and compare those parameters.

On the one hand, a program which is under current development in the group of Prof. Klemradt at RWTH Aachen University was used.^{156,157} The second program used for data

fitting was the *SANS and USANS Reduction and Analysis package* provided by the *National Institute of Standards and Technology* (NIST, Gaithersburg, Maryland, USA).¹⁵⁸ Both programs will be described in more detail in the following sections.

The scattering pattern from the detector was used for the interpretation of the data obtained under flow conditions in contrast to the typical evaluation of scattering curves. Every pattern was normalized to the current of the storage ring and the respective measurement time. Those calculations were performed in the context of a master thesis in the group of Prof. Klemradt at RWTH Aachen University.¹⁴⁹ Specific analytical details are described at the respective position in the results part in section 4.3.5.

4.3.2.5.1 Fitting of Free Size Distributions

Scattering curves received from static SAXS measurements were evaluated in the group of Prof. Klemradt using a versatile computer program which is under their continuous development.^{156,157} The program provides the possibility to fit scattering data using free size distribution functions. Therewith, information on shape and dispersion state of the investigated particles hidden in the scattering curves becomes accessible. Fitting of scattering curves from particles with various geometries including the models for spheres and ellipsoids is possible. Therefore, the program is generally applicable to CPP scattering curves, as previous TEM investigations revealed spherical particles in the first and ellipsoidal particles in the second state.⁵ The program of Klemradt et al. allows to fit a free size distribution to the experimentally determined scattering curve. In this context, the particle geometry and the scattering contrast is required in advance and has to be indicated by the user. Afterwards, each fitting parameter is approximated by means of a size distribution by the use of the software. In case of a spherical model, it provides a size distribution for the radius, while for the ellipsoidal particles size distributions for the three semi-axes are determined. The interval width of the respective size distribution is specified by the user. The fitting procedure is an iterative process using a gradient method based on the method of "Interior-Point Gradient Algorithm".¹⁵⁹ The routine of the *Size Distribution Program* is described in more detail in the diploma theses of S. Meyer¹⁵⁶ and M. Servos¹⁵⁷.

4.3.2.5.2 Data Evaluation based on IGOR Pro

In addition to data evaluation by Klemradt et al. we used the *SANS and USANS Reduction and Analysis package* provided by the *National Institute of Standards and Technology* (NIST, Gaithersburg, Maryland, USA)¹⁵⁸ in combination with the underlying program IGOR Pro 6 (WaveMetrics, Portland, Oregon, USA). IGOR Pro is a scientific data analysis software similar to Origin. The additional NIST analysis package was originally developed for the reduction and analysis of small-angle neutron scattering (SANS) and ultra-small-angle neutron scattering (USANS) data.¹⁵⁸ Nevertheless, evaluation of SAXS data is also possible. In the present case, evaluation of the reduced data was carried out by non-linear fitting to structural models provided by the NIST package. Various models for diverse particle geometries are included in the package. Data can be fitted by choosing either one form factor model or a summed model of two different models. This provides the possibility of considering two differing particle geometries in one fit. The *Gaussian Sphere*- and the *Uniform Ellipsoid*-model as well as combinations of both models were used to evaluate scattering curves from all CPP states. In contrast to the *Size Distribution Program* of Klemradt et al., which has the advantage of providing information on the particle size distribution, the

advantage of the NIST program is the possibility to consider a summed model of two form factors.

4.3.2.6 Light Scattering Measurements

Subsequent to the synchrotron SAXS measurements, all investigated samples were characterized by means of SLS and 3D-DLS. In addition to the samples which had been exposed to synchrotron radiation, reference samples were investigated additionally. Both sample types contained the exact same content and were mixed at the same time. However, the reference samples have not been exposed to synchrotron radiation. Using this procedure we were able to identify possible radiation damages.

Two machines with different wavelengths were used for SLS measurements. Subsequent combination of the resulting scattering curves yield a larger overall q -range. On the one hand, a SoFica (SLS-Systemtechnik, Denzlingen, Germany) with a diode laser with a wavelength of $\lambda = 405 \text{ nm}$ was used. Measurements were carried out between 23° and 149° in 1° -steps. On the other hand, a modified Fica (SLS-Systemtechnik, Denzlingen, Germany) with a He-Ne-laser with a wavelength of $\lambda = 633 \text{ nm}$ was used. Measurements were carried out in 2° -steps between 20° and 144° . In both cases, temperature was 20°C , temperature stability was ensured using an external thermostat. Measurements were carried out in borosilicate glass test tubes (grade 3.3, 75 mm length, 10 mm outer diameter, 0.8 – 1 mm wall thickness; VWR International GmbH, Germany).

Furthermore, a 3D-DLS setup was used for the determination of the hydrodynamic radii. All measurements were performed using a standard light scattering device (LS instruments, Fribourg, Switzerland) with He-Ne-laser (JDS Uniphase, KOHERAS GmbH, 632.8 nm, 25 mW, Type LGTC 685-35), two avalanche photodiodes (Perkin Elmer, Type SPCM-AQR-13-FC) and an ALV 7002 correlator (ALV GmbH, Langen, Germany). The scattered light was detected at an angle of 90° . Temperature stability was ensured by an external thermostat equipped with a Pt-100 temperature sensor. Measurements were carried out in NMR sample tubes (borosilicate glass 5.1., 5 mm outer diameter, 0.43 mm wall thickness; VWR International GmbH, Germany) cut to a length of approximately 70 mm. Single measurements run for two minutes, every diffusion coefficient was calculated from at least two measurements. Hydrodynamic radii were calculated using the Stokes-Einstein relation which provides the size of a sphere moving with the same characteristics as the scattering particle (see equation (3.15)). However, in the present case second-state CPPs with ellipsoidal shape⁵ were investigated. In addition to checking the samples for possible radiation damages, those measurements were performed in order to ensure comparability to previous DLS measurements.¹⁴⁸ Thus, for simplicity, the ellipsoidal shape was neglected and relative differences were determined here.

4.3.3 Results and Discussion: Time-dependent SAXS Measurements

4.3.3.1 SAXS Curves of the CPPs show time-dependent Characteristics

We received time-dependent scattering curves of the CPP-solution from integration of the data collected under static conditions after background-correction. The curves differ from each other in dependence of the CPP state as shown in Figure 4.11. We obtained

characteristic curves for the first and second state of the CPPs as well as for the transition state. In particular, their characteristics differ in the high q -range. SAXS data of the CPP-solution in second state could be extended with SLS data measured subsequently to the SAXS measurements to extend the evaluable q -range.

Data were collected alternately from different capillaries containing the same CPP-solution to minimize beam exposure time and with that a possible influence or damage caused by X-ray irradiation. Fetuin-A samples in TBS were checked for radiation damage revealing no influence of X-ray exposure on the scattering curve of the sample as shown in section 6.4. A comparison of the scattering curves from the different capillaries showed that transition did not occur exactly simultaneously. Therefore, the best achieved time resolution during CPP transition is 17 minutes (see Figure 4.11 b)). However, the results show that the different CPP states as well as the transition can be well monitored with SAXS. Moreover, a continuous change of the scattering curves is observable. Hence, the transition from first to second state is a continuous process rather than an abrupt change.

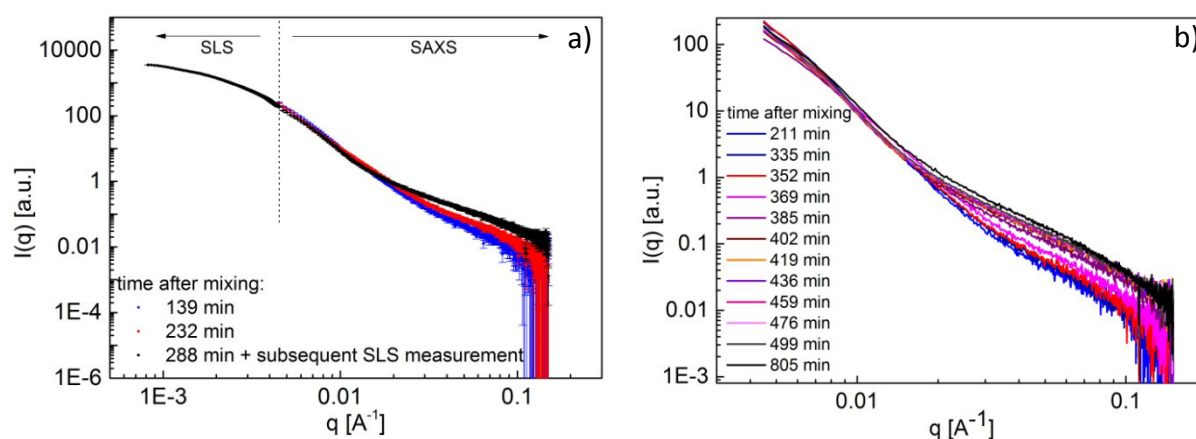


Figure 4.11: SAXS curves of CPPs in different states. Initial solutions contained $13.5 \mu\text{M}$ fetuin-A. SAXS intensity is plotted versus the scattering vector q . The background scattering of TBS was subtracted from the total scattering. a): SAXS curves in first state (blue), second state (black) and during transition (red). SAXS data of second state were extended with SLS data for better interpretability. b): SAXS curves in different time intervals, the best achieved time resolution during transition was 17 minutes. A continuous change of the scattering curves is observable.

4.3.3.2 Evaluation of Scattering Curves using the *Size Distribution Program*

Evaluation of the scattering curves with the *Size Distribution Program* (compare section 4.3.2.5.1) was performed by Olivier De Castro in the context of his master thesis in the group of Prof. Klemradt at RWTH Aachen University.¹⁴⁹ A combination of these results and the results obtained from fitting with the program provided by the NIST on the basis of IGOR Pro (compare section 4.3.2.5.2) should help to elucidate the process of CPP transition.

The more pronounced the characteristics of a SAXS curve are, the more easy is the data interpretation. The occurrence of defined, sharp minima or a characteristic slope are examples for such properties. The SAXS curves shown in Figure 4.11 exhibit indeed a slight minimum, although it is not very pronounced. The curves mainly differ in their slope in the higher q -range at q -values above approximately 0.02 \AA^{-1} for the different states of the CPP-solution. The characteristics of the scattering curve in the low q -range of the SAXS data do not change with CPP transformation but they are rather independent of the state of the CPP-solution. Interestingly, clear pronounced minima are missing in the scattering curves.

Fitting of simulated data for particles with varying polydispersity with the *Size Distribution Program* has shown that the informative value and plausibility of the fit results decreases with increasing polydispersity of the particles.¹⁴⁹ Nevertheless, the routine has been applied to fit scattering data of the CPP-solution in first and second state.

From previous TEM measurements first-state CPPs are known to be spherical while the second-state CPPs are prolate ellipsoids.⁵ Therefore, the form factor models for spheres and ellipsoids were used, respectively. Up to now, the form factor of an ellipsoid of revolution has not been implemented into the fitting routine. Therefore, the form factor of a general ellipsoid has been applied.

Fitting of the Experimental SAXS Data of the first-state CPP-Solution

Data of the first-state CPP-solution with an initial fetuin-A concentration of 13.5 μM have been fitted with the spherical and the ellipsoidal model, respectively. The fits with the corresponding results for the characteristic lengths in the first state are shown in Figure 4.12.

In both cases, the fit matches the corresponding scattering curves well. The high probability for a radius of 1500 \AA in the spherical fit is an artifact. The appearance of a high probability at the biggest permitted value for the radius was already known from the fit of simulated data. The size distribution received from the respective fit was evaluated using a Gaussian profile to determine the mean value of the radius or the respective semi-axis as shown exemplarily for the ellipsoidal model in Figure 4.12. The spherical fit model provides a radius of $R = (90 \pm 1.6)$ nm for the first-state CPPs. The semi-axes of the ellipsoid were determined with $A = (72 \pm 2.5)$ nm, $B = (93 \pm 1.9)$ nm and $C = (113 \pm 0.6)$ nm.

If in the first state only spherical CPPs were present, the determined values for all semi-axes should be equal yielding a spherical structure. In the present case, the values obtained for the semi-axes A and B are comparable. However, the main value determined for semi-axis C is slightly higher. The deviation of the values for the single semi-axes and the deviation of the semi-axes compared to the radius determined with the spherical model can either result from the boundary conditions chosen for the fit or -more likely- mirror the real situation in the CPP-solution. We assume to have spherical CPPs in first state on the basis of TEM pictures.⁵ However, it is possible that the particles are slightly anisotropic or that a fraction of particles is already in the transition state or even in the second state. The second assumption is supported by the radius derived from the spherical fit which is rather in the range of second-state CPPs.¹⁴⁸

It is additionally known that so-called CPMs are formed simultaneously with the CPP formation.²⁷ However, in DLS measurements, the CPPs clearly dominate overall scattering, which was also expected for SAXS measurements. CPPs are clearly bigger than the CPMs so that we expected the characteristics of the scattering curve to be governed by CPP scattering. In addition, the mineral content of the CPPs is much higher compared to the CPMs so that CPP scattering should be more pronounced than CPM scattering.

The chosen boundaries for the fit do not include the size range below 10 nm, so that smaller structures such as the CPMs are not considered in the size distribution. Nevertheless, those smaller structures are assumed to contribute to the characteristics of the overall scattering curve making a concluding explanation of the results rather difficult. This leads to the conclusion that the *Size Distribution Program* has to be extended by an algorithm to fit two

models simultaneously to one scattering curve.¹⁴⁹ The results of a two-model fitting approach on the basis of the NIST package is described in section 4.3.3.3.

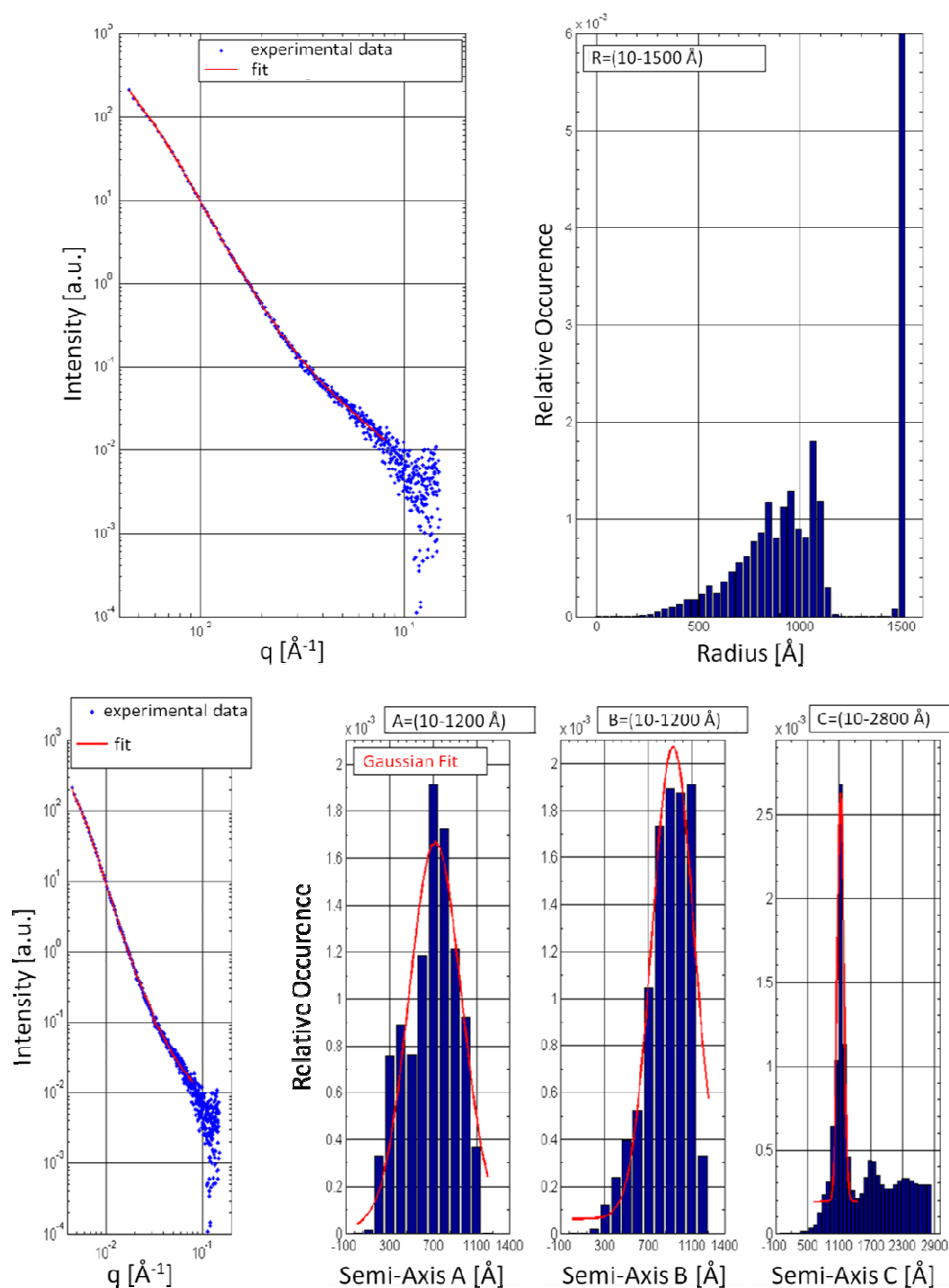


Figure 4.12: Evaluation of SAXS data of a first-state CPP-solution with an initial fetuin-A concentration of $13.5 \mu\text{M}$ using the *Size Distribution Program*. Data were fitted with a spherical (upper diagram) and an ellipsoidal (lower diagram) form factor model. Fits provided specific distributions of the characteristic lengths (radius and semi-axes, respectively). The obtained size distributions were fitted with a Gaussian fit as shown in the lower diagram.¹⁴⁹

The spherical fit has also been applied to the data of a first-state CPP-solution with a higher initial fetuin-A concentration of $35 \mu\text{M}$.¹⁴⁹ Different to the results described before, the fits partially reveal two maxima for the radius in first state. While one of the maxima lies typically in the range of the hydrodynamic radius determined for the first state, the second maximum

typically exhibits values in the size range expected for the second CPP state. These findings support the hypothesis of different particles being in different states at the same time. This in turn supports the assumption that the process of CPP transformation is a continuous process occurring independently for every single particle.

Fitting of the Experimental SAXS Data of the second-state CPP-Solution

SAXS curves of the second-state CPP-solution (CPP(2)-solution) have been fitted using the spherical and the ellipsoidal form factor model, respectively, although TEM pictures of the second-state CPPs showed an ellipsoidal particle shape⁵. The detailed results can be found in the work of O. De Castro.¹⁴⁹ The values for the radii derived from the spherical fits are similar to the results for the first state.¹⁴⁹ For the lower initial fetuin-A concentration, the radius is determined with approximately 95 nm and with that in the same size range as determined for the first state scattering data. For the higher initial fetuin-A concentration, fitting of the second state curves revealed one maximum with a mean value of approximately 87 nm compared to the two maxima determined for the first state. In both cases, the radii are slightly below the values for the hydrodynamic radius determined with 3D-DLS after beamtime ($R_{H,1}$ = 117 nm for the lower fetuin-A concentration, $R_{H,2}$ = 96 nm for the higher fetuin-A concentration). The hydrodynamic radius is typically larger compared to the radius derived by fitting of SAXS data. Hence, the fit results are in a reasonable size range.

The results for the application of the ellipsoidal fit model on the second-state CPP-solution derived from the lower and the higher initial fetuin-A concentration, respectively, are shown in Figure 4.13. In all tested cases, the smaller semi-axes A and B exhibit sizes in the range of the radius expected for the first-state CPPs. This is in good agreement with previous studies describing the secondary CPPs as prolate ellipsoids anisotropically grown from the first-state CPPs.⁵

The results for the third semi-axis C were less unambiguous. In some cases, two maxima appeared, so that a distinct interpretation is not possible. However, fit results were used to calculate the ratio of the semi-axes. From previous TEM measurements, a ratio of $r = b/a = 0.3$ was estimated, where b is the shorter and a the bigger semi-axis.⁵ The values derived from the fitting with the *Size Distribution Program* provide axis ratios in the same range, varying between $r = 0.28$ and $r = 0.46$. Taking into account the difficulties in data interpretation in the present case (appearance of two maxima in some cases), the values are reasonable within the framework of possibilities.

Fitting of the Combined Experimental SAXS and SLS Data of the second-state CPP-Solution

The curves of the second-state CPPs could supplementary be combined with SLS data to enlarge the evaluable q-range to smaller q-values (see Figure 4.11). The gap in between the scattering curves was closed by data interpolation performed by Olivier de Castro in the context of his master thesis.¹⁴⁹ The bigger the evaluable q-range the more information is contained in the SAXS data and with that the easier and more unique becomes data evaluation. With enlarged q-range to smaller q-values, fitting becomes more sensitive for bigger particles. In previous SANS measurements of the CPPs in the different states the evaluable q-range ranged from $2.5 \cdot 10^{-3} \text{ \AA}^{-1}$ up to 0.1 \AA^{-1} .⁴ With the enlargement by SLS data,

the resulting q -range in the present case is slightly bigger ranging from $8 \cdot 10^{-2} \text{ \AA}^{-1}$ up to 0.2 \AA^{-1} .

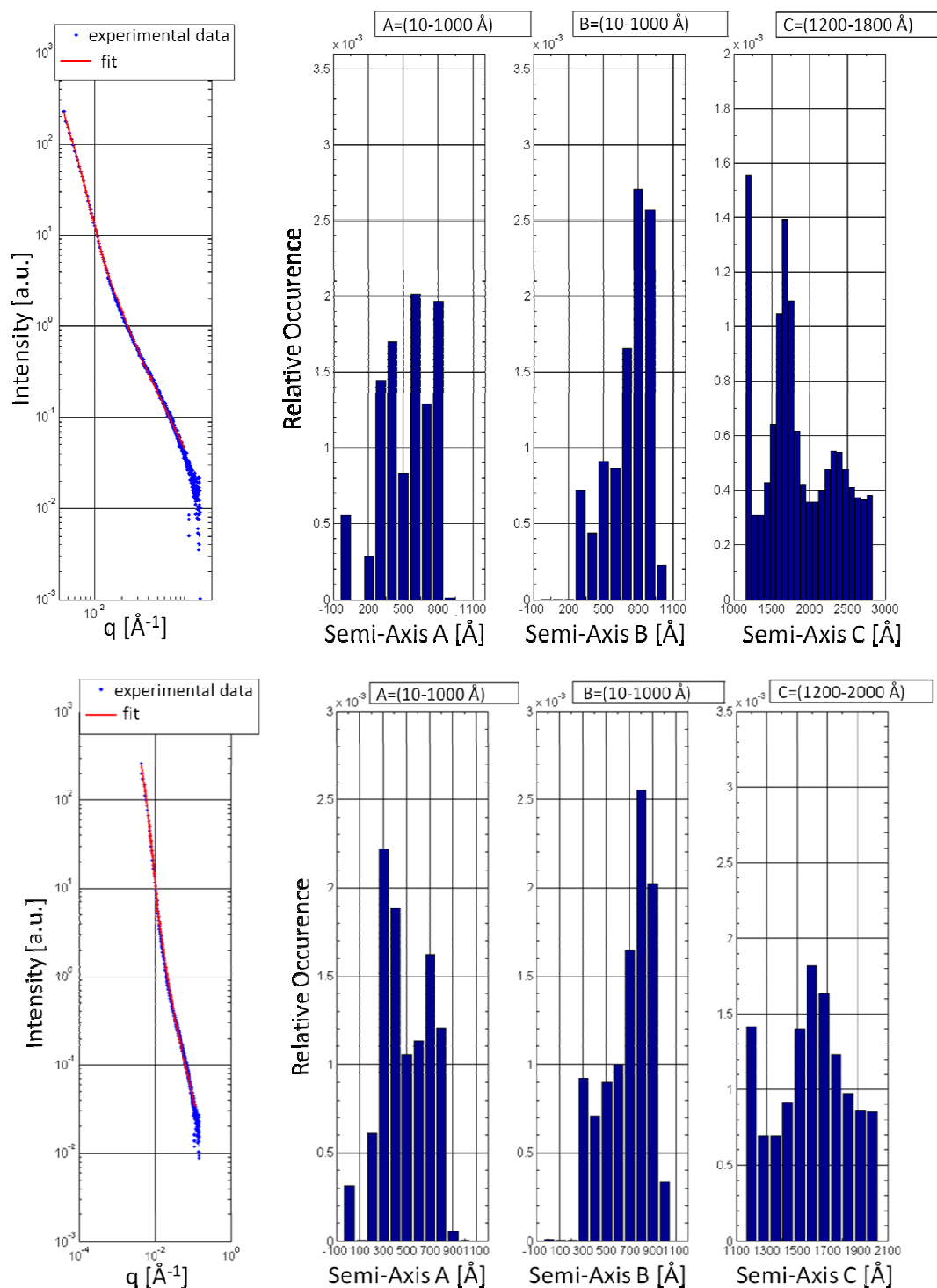


Figure 4.13: Evaluation of SAXS data of a second state CPP-solution with an initial fetuin-A concentration of $13.5 \mu\text{M}$ (upper diagram) and $35 \mu\text{M}$ (lower diagram) using the *Size Distribution Program*. Data were fitted with an ellipsoidal form factor model. Fits provided specific distributions of the characteristic semi-axes. The obtained size distributions were fitted with a Gaussian fit (compare Figure 4.12).¹⁴⁹

Figure 4.14 shows the fits for the SAXS data combined with SLS data measured at $\lambda = 405 \text{ nm}$ using a spherical and an ellipsoidal form factor, respectively.

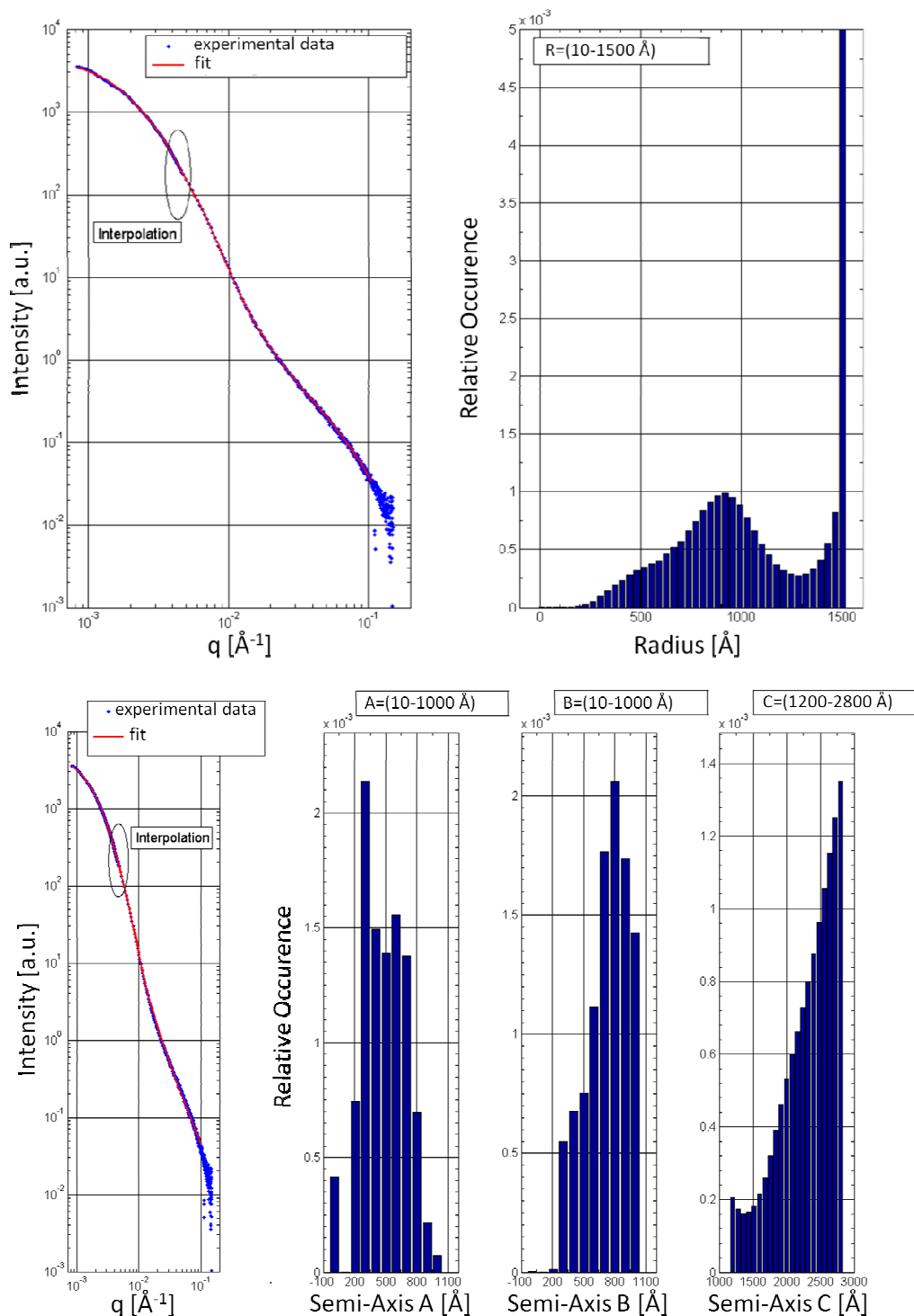


Figure 4.14: Evaluation of combined SAXS and SLS data of a second-state CPP-solution with an initial fetuin-A concentration of $13.5 \mu\text{M}$ using the *Size Distribution Program*. The gap in between SAXS and SLS data was closed by data interpolation in the region labeled with a sphere. Data were fitted with a spherical (upper diagram) and an ellipsoidal (lower diagram) form factor model. Fits provided specific distributions of the characteristic lengths (radius and semi-axes, respectively). The obtained size distributions were fitted with a Gaussian fit (compare Figure 4.12).¹⁴⁹

The enlargement of the q -range leads to a flatter size distribution while the determined sizes for the second-state CPPs are in the same size range as before. The higher sensitivity for bigger particles finds expression in the displacement of the maximum for the larger semi-axis C and the indication of a second maximum in the radius determined with the spherical

form factor. However, a secured conclusion describing the second-state CPPs is still not possible. The size distribution of the radius for the spherical fit for different scattering curves in second state is just as inconsistent as the results for the ellipsoidal fit (mainly semi-axis C). In summary it is not possible to unambiguously characterize the particles in first- and second-state CPP-solution from fitting of the respective scattering data with the *Size Distribution Program*. The provided characteristic lengths are not unique, although the fits match the experimental scattering data of primary and secondary CPPs.

It is known that at least two particle types (CPPs and CPMs) are present in the CPP-solution. Therefore, at least two extensions of the fitting routine are necessary in order to obtain reliable results. On the one hand, the size range used for fitting has to be extended to smaller length scales to consider a probable influence of CPM scattering on the overall characteristics of the scattering curve. On the other hand it is necessary to consider more than one form factor model at the same time in the fitting routine. Up to now, the *Size Distribution Program* is designed for fitting data under consideration of only one form factor model.

Thus, we used a second program for data fitting under the consideration of a model including two form factors. The results are described in the following section.

4.3.3.3 Evaluation of Scattering Curves based on IGOR Pro

A second, independent approach was made in order to fit the scattering data. Therefore we used a widely established fitting routine provided by the NIST¹⁵⁸ on the basis of IGOR Pro (detailed description see section 4.3.2.5.2). The fitted curves are the same as the curves fitted with the *Size Distribution Program* in the group of Prof. Klemradt to achieve comparability.

The challenge of interpreting CPP scattering data lies in the lack of pronounced characteristics (minima) in the scattering curve as described before. From the fits with the *Size Distribution Program* we conclude that the application of only one particle geometry in the fit is probably insufficient. The NIST package offers the advantage to create a summed model including two form factor models to fit the scattering data. We used combinations of two models implemented in the fitting routine: the *Gauss sphere-model* and the model for the *uniform ellipsoid* as TEM pictures of the CPPs have shown the transformation from spherical particles to prolate ellipsoids.⁵ The Gauss sphere model includes the form factor of a sphere with variable polydispersity. The uniform ellipsoid model contains the form factor of a monodisperse ellipsoid of revolution. Detailed descriptions of the respective models can be found in the model help file of the NIST package.¹⁵⁸ We tried all three possible combinations of the two models to fit scattering data of the first and second state as well as data collected during CPP transition.

Different parameters are fitted depending on the chosen model. In the present case, the characteristic variables for each model (radius and polydispersity for the Gauss sphere, semi-axes for the uniform ellipsoid) as well as the scattering length densities (SLDs) of particles and solvent are taken into account.

Typically, the fitting result becomes more reliable with increasing knowledge of the particular parameters as in that case initial values can be chosen more properly. Hence, we estimated the SLDs for the CPP samples before fitting in order to obtain reliable results. Unpublished

ultracentrifuge experiments (Alexander Heiss, Jong Seto, Willi Jahnen-Dechent, Helmut Cölfen, unpublished) provided values for the density of the CPP-solution. No difference was observed for the densities in first and second state. The measurements provided an average of $\rho = (1.27 \pm 0.09) \text{ g/cm}^3$ which we used in order to fit the SAXS data. With a wavelength of $\lambda = 1.22 \text{ \AA}$ we calculated a SLD for octacalcium phosphate and hydroxyapatite, respectively. For both cases we received a SLD value of $\text{SLD} \approx 1.1 \cdot 10^{-5} \text{ \AA}^{-2}$. In addition to the calculated SLD for the particles we used the SLD of water as solvent SLD ($\text{SLD} \approx 9.5 \cdot 10^{-6} \text{ \AA}^{-2}$). The values were calculated with an online SLD calculator.¹⁶⁰ The calculated values were kept fixed during fitting.

From the diffusion coefficient of the second-state CPPs determined with 3D-DLS we calculated the expected semi-axes of the second-state CPPs. The axial ratio was determined as $r = b/a = 0.3$ from previous TEM measurements, where b is the shorter and a is the longer semi-axis.⁵ The hydrodynamic radius which has been taken into account was determined from two samples with an initial fetuin-A concentration of 13.5 \mu M . One of the two samples has been used for SAXS measurements and was therefore exposed to the X-ray beam for several hours. The second sample was mixed at the same time as the first sample but has not been exposed to X-rays (reference sample). For the first sample (after X-ray exposure), we measured a hydrodynamic radius of $R_H = 116 \text{ nm}$, while measurement of the second sample (without X-ray exposure) provided a value of $R_H = 95 \text{ nm}$.

From this result it is imaginable that the difference in the hydrodynamic radius is caused by radiation damages. However, comparing the results for different samples, no clear trend is visible. In some cases the radius of the particles is bigger after X-ray exposure compared to the samples which have not been exposed to X-rays, in other cases this result is reverse. Additionally, our investigations on the influence of X-ray exposure on fetuin-A samples have shown no distinct effects (compare section 6.4). Thus, we assume that sample damages due to X-ray exposure are insignificant and used the determined hydrodynamic radii to calculate the lengths of the semi-axes a and b for a prolate ellipsoid using equation (4.4).

SANS measurements of the secondary CPPs revealed their structure: a mineral core is surrounded by a fetuin-A-monolayer.⁴ In SAXS, the protein exhibits a significantly lower scattering intensity compared to the mineral core. Therefore, the semi-axes of the mineral core were calculated by subtraction of the thickness of the fetuin-A monolayer in a further step. In previous measurements, the hydrodynamic radius of fetuin-A was determined with an approximate value of $R_H \approx 4 \text{ nm}$.³ Hence, considering the full diameter of the protein, 8 nm were subtracted from every semi-axis. All calculated values are shown in Table 4.4.

$$R_H = \frac{a \sqrt{1 - \frac{b^2}{a^2}}}{\ln \left[\frac{1 + \sqrt{1 - \frac{b^2}{a^2}}}{\frac{b}{a}} \right]} \quad (4.4)$$

The size from SAXS data fitting was hypothesized to be smaller than the hydrodynamic radius. Nevertheless, the calculated values allow an estimation of the expected size range. The initial values for data fitting were chosen on this basis. On the one hand, the calculated values provide the size range for the second-state CPPs. On the other hand, the values for the smaller semi-axis can be used to estimate the radius of the first-state CPPs as previous

measurements indicated an anisotropic growth of the first-state CPPs to become second-state CPPs.⁵ Thus, the length of the smaller semi-axis in second state is consistent with the hydrodynamic radius of the first-state CPPs.

SANS measurements revealed that only 3-5 % of the total fetuin-A content and approximately 60 % of the mineral are contained in the CPPs.⁴ In consequence, a second particle species contained in the CPP-solution (CPMs) was found using SANS with contrast variation.²⁷ Hence, the CPP-solutions investigated in the present work do not only contain CPPs but certainly additional CPMs. Up to now, only these two particle types could unambiguously be identified, although the presence of further particle types such as free fetuin-A (and fetuin-A aggregates) and free mineral is assumed and very likely. Data evaluation was thus performed under the assumption of those two species being present.

Table 4.4: Characteristic lengths of the second-state CPPs. The sizes of the semi-axes were calculated for a prolate ellipsoid from the hydrodynamic radius measured with 3D-DLS. The ratio of the semi-axes was assumed as $r = b/a = 0.3$.⁵

Hydrodynamic Radius R_H	Longer semi-axis a	Shorter semi-axis b	Longer semi-axis a after fetuin-A subtraction	Shorter semi-axis b after fetuin-A subtraction
$R_{H,1} = 116 \text{ nm}$	$a_1 = 227.5 \text{ nm}$	$b_1 = 68.2 \text{ nm}$	$a_{1woF} = 219.5 \text{ nm}$	$b_{1woF} = 60.2 \text{ nm}$
$R_{H,2} = 95 \text{ nm}$	$a_2 = 186.6 \text{ nm}$	$b_2 = 56 \text{ nm}$	$a_{2woF} = 178.6 \text{ nm}$	$b_{2woF} = 48 \text{ nm}$

Experimental SAXS data could be fitted for every state of the CPP-solution as shown in the following sections. The estimated SLDs were kept fixed during fitting and the start values for radii and semi-axes were calculated as described (for values see Table 4.4). Furthermore, in the case of using a form factor model consisting of two single form factor models, the incoherent background was set to zero for one form factor model as described in the manual of the NIST package.¹⁵⁸ Hence, the fit provides values for radius and polydispersity (spherical form factor), semi-axes (ellipsoid), scale and background.

However, the results obtained from fitting are at least partially little reliable as will be shown later. Due to the fact that the SLDs can only be estimated from ultracentrifugation experiments, no distinct values for the fractions of CPPs and CPMs are available. This affects the scale factor obtained from fitting as both parameters depend on each other. In other words, the scale of the particular species cannot reliably be obtained as long as the SLD of the single species is not known. Nevertheless, the results of data fitting are shown and discussed below.

Calculation of Theoretical Scattering Curves

Second-state CPPs are long-term stable.⁵ Therefore, this state can be accessed and investigated more easily than the first state and the CPP transformation. Thus, the second state was used as origin for further evaluation of the mineral stabilization by fetuin-A.

Hence, theoretical scattering curves for the second-state CPPs and the CPMs were calculated using the NIST package¹⁵⁸ in combination with IGOR Pro (compare section 4.3.3.3) in a first

step. Those curves were compared to the experimental scattering data of the second-state CPP-solution to make a rough estimation whether the characteristics of the experimental data can be caused by the summed scattering of the two different particle types. For that purpose, a combination of SAXS and SLS-data was used in order to obtain a preferably wide q -range. The comparison is shown in Figure 4.15.

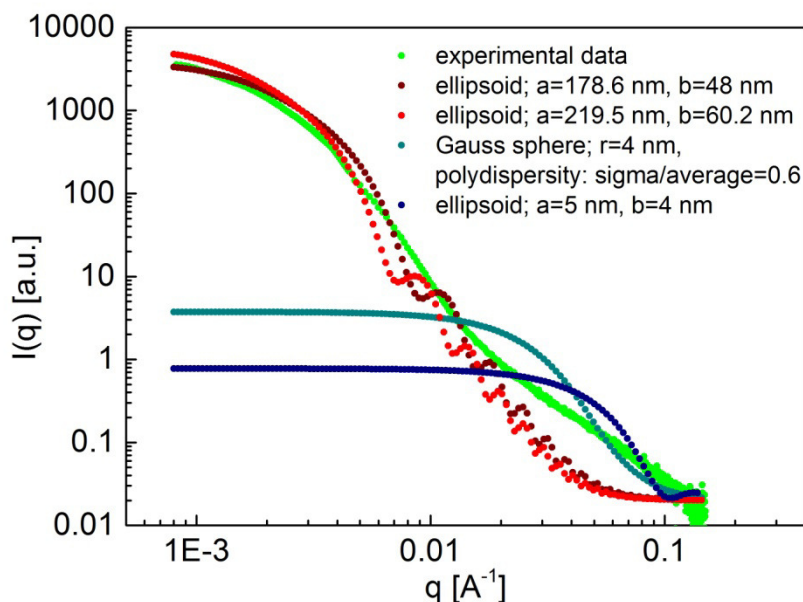


Figure 4.15: Comparison of experimental scattering data (combined SAXS and SLS data with interpolation, initial fetuin-A concentration of $13.5 \mu\text{M}$) of second-state CPP-solution with theoretically calculated curves. The experimental data are assumed to be composed of scattering from different particle types, at least from CPP and CPM scattering. The reddish curves show the theoretical scattering of monodisperse prolate ellipsoids in the size range expected for the CPPs from their hydrodynamic radius measured with 3D-DLS with and without consideration of the fetuin-A monolayer. The bluish curves are theoretical curves as expected for the CPM scattering. Those curves were calculated for a monodisperse prolate ellipsoid with axes length as obtained for the fetuin-A molecule from BioSAXS measurements (see section 4.2.3.3) and a polydisperse Gaussian sphere (60 % polydispersity), respectively.

While the scattering of the large ellipsoids (assigned to the CPPs in the present case) dominates the characteristics in the lower q -range ($q < 0.02 \text{ \AA}^{-1}$), the higher q -range ($q > 0.02 \text{ \AA}^{-1}$) scattering is dominated by the smaller particles (CPMs in the present case). From the comparison shown in Figure 4.15, it is in principle imaginable that a combination of the CPP and the CPM scattering curves could be used to fit the experimental data (at least of the second state).

In a second approach, the average theoretical scattering curve of CPPs and CPMs was calculated using a sum model of two ellipsoids with the respective sizes. The obtained curve was compared to the experimental SAXS data. The comparison is shown in Figure 4.16. In the calculated sum model, distinct minima are visible while no pronounced characteristics are visible in the experimental data. This comparison already indicates that CPPs and CPMs are not the only species present in the CPP-solution in second state.

Nevertheless, data were fitted with similar sum models in the subsequent step. Every SAXS curve was fitted with the three different sum-models, e.g. the model included either the form factors of two Gaussian spheres, of two monodisperse ellipsoids or it included the form factor of a Gaussian sphere in combination with the factor of a monodisperse ellipsoid, respectively. The respective combination which matches the experimental data best is shown

in the next section for the second state, the first state and the transition state of the CPP-solution.

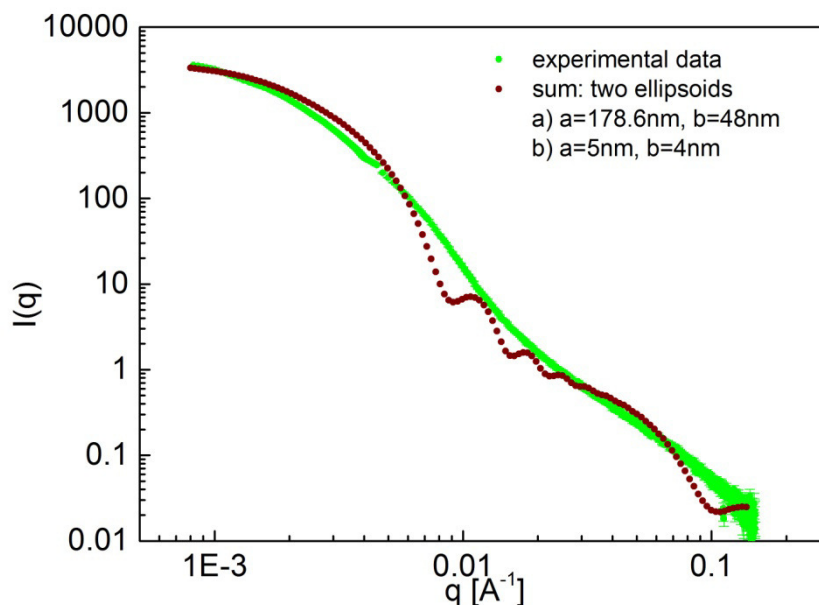


Figure 4.16: Comparison of experimental scattering data (combined SAXS and SLS data, initial fetuin-A concentration of 13.5 μM) of a second-state CPP-solution with theoretically calculated curves. The experimental data are assumed to be composed of scattering from different particle types, at least from CPP and CPM scattering. The calculated curve shows the summed theoretical scattering of monodisperse prolate ellipsoids in the size range expected for the CPPs and monodisperse prolate ellipsoids in the size range expected for the CPMs.

Fitting of the Experimental SAXS Data of the second-state CPP-Solution

In a first step, SAXS data of the second-state CPP-solution were fitted on the basis of our considerations concerning the composition of this solution. The best fit was achieved using the sum model of two ellipsoids. The result is shown in Figure 4.17.

It is possible to derive information on the characteristic sizes of the particles from fitting. The obtained axes are $R_{a,1} = a_1 = 24.3 \text{ nm}$ and $R_{b,1} = b_1 = 56.4 \text{ nm}$ for the larger ellipsoid. Those values correspond to the values derived for the ellipsoidal particles in the first-state CPP-solution as shown below. However, it does not match previous 3D-DLS results.^{5,148} The semi-axes calculated from 3D-DLS measurements lie above the values determined with SAXS in the present case. A direct comparison of the values determined with SAXS and 3D-DLS using the same sample (3D-DLS results see Table 4.4) shows that the lengths of the semi-axes determined from DLS are two- to fivefold higher than the lengths of the semi-axes determined from SAXS data fitting. Furthermore, the axial ratio of $b/a = 2.3$ deviates from the axial ratio reported in earlier studies using TEM, where $b/a = 0.3$ was determined under the assumption of second-state CPPs being prolate ellipsoids.⁵ In contrast to that, the fits in the present case provide an oblate ellipsoid. This is due to the q^{-2} -decay at low q -values, whereas prolate ellipsoids typically exhibit a q^{-1} -decrease at low q -values (NIST analysis package¹⁵⁸, function help, Uniform Ellipsoid). However, the term ‘low q ’ given in the function help of the NIST package¹⁵⁸ is rather nonspecific. Depending on what is regarded as ‘low q ’, the characteristics of the CPP scattering curve decrease with q^{-1} (transition into the plateau) or q^{-2} , respectively. Altogether, this result cannot be explained at the moment. Even if the exact shape of the ellipsoidal particles is neglected and the elementary ratio between largest

and smallest axis is considered, the determined values for the axial ratio deviate with about 23 %.

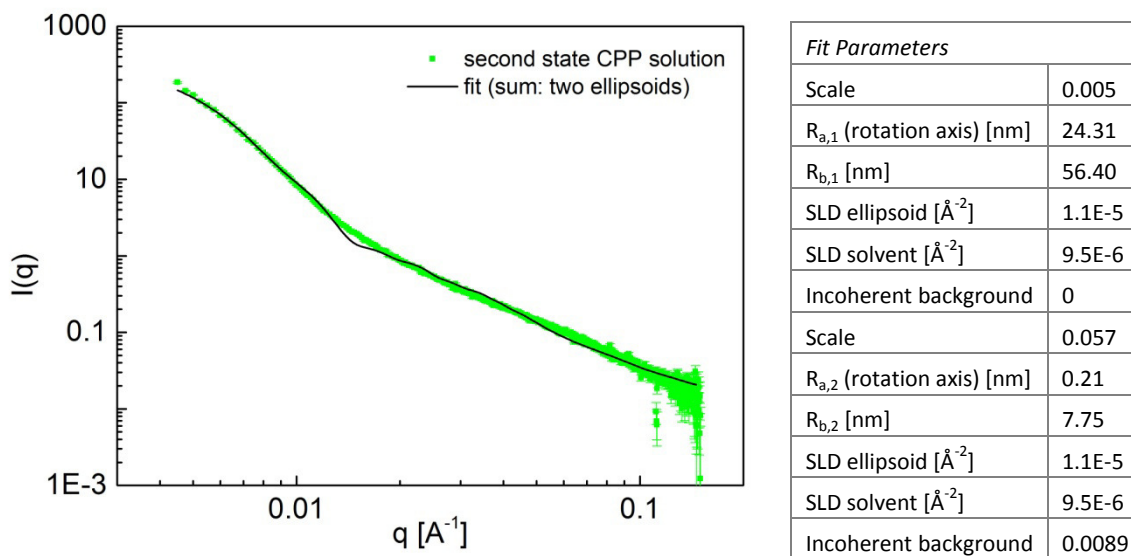


Figure 4.17: Left: Experimental result and related fit of SAXS data from a second-state CPP-solution with an initial fetuin-A concentration of $13.5 \mu\text{M}$. The fit shows the same minimum as the fit for the first state CPP-solution at $q \approx 0.015 \text{\AA}^{-1}$ missing in the experimental data. Apart from that the fit matches the experimental data relatively well. Right: Fit parameters. All SLDs as well as one of the two background parameters were fixed during fitting in order to obtain the most reliable fitting result. The remaining parameters shown in the box were obtained from fitting.

The values for the second ellipsoidal particle type obtained from the fit are $R_{a,2} = a_2 = 0.2 \text{ nm}$ and $R_{b,2} = b_2 = 7.8 \text{ nm}$. The length of the axis a_2 is a tenfold smaller than expected for the CPMs. The length of axis b_2 is approximately twice the size supposed for the CPMs. Sizes in the range assumed for the second-state CPPs could not be obtained by fitting under consideration of the known parameters.

Similar to the fits with the *Size Distribution Program*, fitting does not provide distinct values in the size range of the CPPs and/or the CPMs and does therefore not match our hypothesis although the fit matches the experimental data quite well. However, the comparison of experimental data and the theoretical summed scattering curve of CPPs and CPMs shown in Figure 4.16 has already indicated the appearance of discrepancies between hypothesis and experimental data. The form factor minima seen in the theoretical curve are not visible in the experimental data. It is possible that the high concentration of particles smaller than the CPPs and/or a high polydispersity of the particles influences the average scattering of the solution in a way that the form factor minima vanish. The scale factor values obtained from fitting have to be regarded with suspicion as described before. However, it is a tenfold higher for the smaller particles compared to the bigger particles. From SANS measurements it is known that only 3-5 % of the total fetuin-A content and approximately 60 % of the mineral are contained in the CPPs.⁴ Hence, a big percentage of both fractions forms CPMs or remains in the solution, respectively, and contributes to the average scattering. Obviously, the remaining fetuin-A and mineral not incorporated in the CPPs do not form monodisperse particles as the scattering curve does not show distinct characteristics.

Up to now, the CPP species is the best investigated particle type contained in the CPP-solution.^{4,5,148} The rest of the solution composition is less well understood. Hence, the

evaluable q -range was extended to lower q -values by combining the SAXS data with SLS data of the same solution. In this lower q -range, CPP scattering should be dominant. Fitting of the combined data can help to better understand the SAXS curves and the composition of the second-state CPP-solution. The results are shown below.

Fitting of the Combined Experimental SAXS and SLS Data of the second-state CPP-Solution

Using the NIST software, the same combined data of SAXS and SLS measurements were fitted as in case of fitting with the *Size Distribution Program*. The result is shown in Figure 4.18.

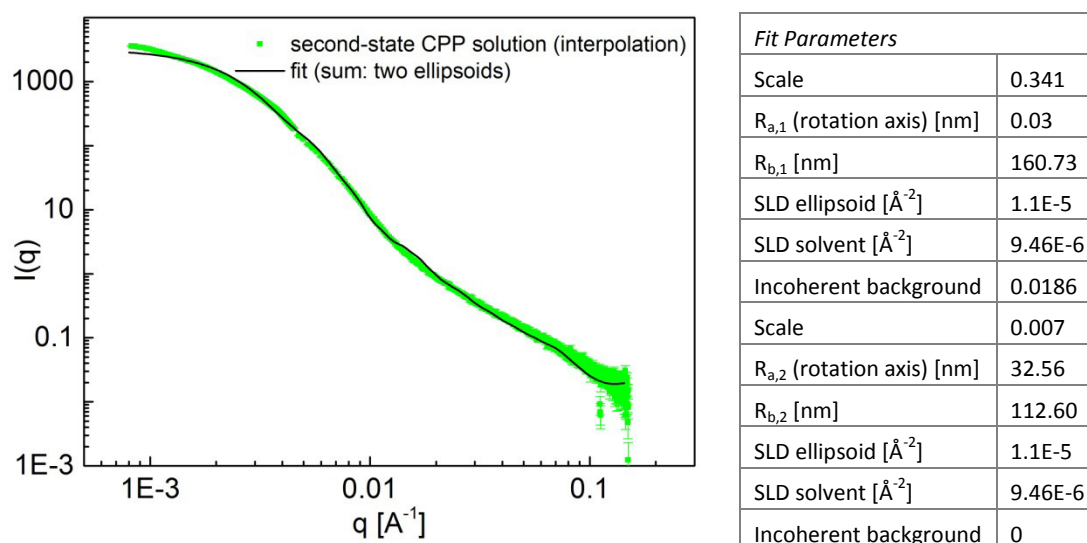


Figure 4.18: Left: Combination of experimental SLS and SAXS data and related fit from a second-state CPP-solution with an initial fetuin-A concentration of $13.5 \mu\text{M}$. The fit matches the experimental data. The minimum in the fit of the SAXS data alone does not appear here. Right: Fit parameters. All SLDs as well as one of the two background parameters were fixed during fitting in order to obtain the most reliable fitting result. The remaining parameters shown in the box were obtained from fitting.

The best fit result under consideration of the known parameters was again obtained using the sum model of two ellipsoids. This is consistent with the fitting of the SAXS data without extension by SLS data. The fitting quality is also similar in both cases. A comparison of the values for the specific axes is shown in Table 4.5.

Table 4.5: Comparison of semi-axes obtained from fitting of SAXS data of a second-state CPP-solution with and without q -range extension by SLS data using the combination of two ellipsoidal form factor models.

	$R_{a,1}$ [nm]	$R_{b,1}$ [nm]	$R_{a,2}$ [nm]	$R_{b,2}$ [nm]
SAXS	24.3	56.4	0.2	7.8
SAXS + SLS	0.03	160.7	32.6	113

The obtained values differ substantially from each other, although the fit quality is similar. Three of the four determined lengths of the semi-axes shift to higher values, which is due to the extension of the q -range to smaller values and thus the consideration of larger length scales. However, the scattering in the lower q -range cannot uniquely be assigned to only one of the two obtained particle types as at least one axis shifts to higher values for both particle

types, respectively. Simultaneously, the small axis length of one particle type shifts to a significantly lower, little reliable value, which cannot be explained by the extension of the q -range to lower q -values.

The fit of the unexpanded data provides an ellipsoid in a size range below 10 nm and another ellipsoid in a medium size range (around 35 - 40 nm), whereas the fit of the combined data provides totally different values. In addition to an ellipsoid with a very high axial ratio above 5000 it provides an ellipsoid with axes in a size range expected for the CPPs ($R_{a,2} = a_2 = 32.6$ nm, $R_{b,2} = b_2 = 113$ nm) with an axial ratio of 3.5. This value is in accordance with the ratio of the semi-axes previously determined from electron micrographs.⁵ But again, an oblate ellipsoid is obtained rather than a prolate ellipsoid as reported from previous TEM measurements.⁵ This correlates to the result obtained from fitting of the mere SAXS data described before. The deviation cannot be explained at the moment.

Nevertheless, in comparison to the fit of the mere SAXS data, the combined data of SAXS and SLS measurement obviously provide a more reliable result as they provide at least one species that exhibits axes lengths in the size range expected for the CPPs. This matches our hypothesis as the extension of the evaluable q -range to lower values should increase the q -range in which CPP scattering is predominant.

However, the result is not fully consistent with the results obtained from fitting with the *Size Distribution Program*. In that case, the data combination led to a flatter size distribution while the obtained values for the axes stayed in the same size range. Obviously, an elucidation of the occurring mechanisms within mineral stabilization by CPP formation based on static scattering data alone is very difficult.

Comparison of Results from SAXS with Results from Previous 3D-DLS Measurements

Besides SAXS and SANS, especially time-dependent 3D-DLS measurements have been applied to characterize the different CPP states up to now.^{4,5,26,27,148} The hydrodynamic radii of the CPPs in first and second state determined by 3D-DLS typically possessed a relatively small size distribution (compare Figure 4.1). Some - but not all - measurements also show a slight maximum in the size range of the CPMs and fetuin-A, respectively. The autocorrelation curve is generally smooth. Hence, only two particle species can be identified from 3D-DLS measurements. However, the results obtained from SAXS measurements with subsequent data fitting show that the CPP-solution is not composed of only monodisperse CPPs and CPMs. It has to be clarified whether the characteristics of the SAXS curves are only determined by polydisperse CPPs and CPMs or whether a wide size distribution of (different) yet uncharacterized particles is present.

Particle dispersities can be considered in order to find a possible explanation for the deviating results in DLS and SAXS. In polymer science, the polydispersity of particles is described by the distribution of their molar mass. A similar approach was used in the present case to gain additional information on the dispersity of particles present in the second-state CPP-solution. The polydispersity of the particles was estimated by calculation of the polydispersity index *PDI* from cumulant analysis of 3D-DLS data via

$$PDI = \frac{2\kappa_2}{\kappa_1^2} \quad (4.5)$$

where κ_1 and κ_2 are the first and second order cumulants (compare section 3.3.2). This analysis provided polydispersity indices in the range of 0.2 - 0.6 for the second-state CPP-solution. These values are very high compared to earlier measurements providing values below 0.1 for the second-state CPPs using the same method.⁵ Unfortunately, the significant differences between the present measurements and the lower values obtained previously cannot adequately be explained. However, the signal to noise ratio in 3D-DLS is rather low so that the polydispersity values obtained from 3D-DLS measurements have to be treated with caution.

The determination of the polydispersity of the smaller CPMs is actually not possible from 3D-DLS data as the maximum for those particles is either not present or unincisive. This weak occurrence of the CPM peak cannot be reconciled with the fitting using the NIST package. Those fits usually provide at least one axis in a size range below 10 nm indicating the presence of small structures which have considerable influence on the overall scattering pattern of the CPP-solution. Furthermore, it is very likely that free fetuin-A and mineral is present additional to the CPMs. Those particles are either too small (mineral) or exhibit only weak scattering (fetuin-A), so that they are nearly invisible in 3D-DLS.

The Presence of Small Particles must not be neglected in Data Evaluation from CPP-Solution Scattering

Up to now, the presence of structures in a size range below 10 nm or even below 1 nm apart from the CPMs could not be verified. It is known that the CPPs consist of an amorphous protein-mineral phase in first state and a rather crystalline phase (octacalcium phosphate, OCP) with a surrounding fetuin-A monolayer in second state.⁴ Therefore, it is possible that the smaller structures influencing the scattering characteristics are no additional small particles but rather structural details (e.g. of the CPPs) which significantly influence the signal in static scattering experiments. None of the two possibilities can finally be excluded from the obtained SAXS data.

Furthermore, from SANS measurements it is known that only 3-5 % of the total fetuin-A content and approximately 60 % of the mineral are contained in the CPPs.⁴ Additionally, it was found that the amount of calcium contained in the CPPs increases with 50 % from first to second state.²⁷ Hence, at least a time-dependent rearrangement of mineral takes place. Therefore, it seems likely that additional (free) mineral and possibly also (free or aggregated) fetuin-A is present at all states of the CPP-solution. Such an occurrence of smaller mineral and protein particles could explain the obtained results.

Altogether, by now we know that the small structures have to be considered for elucidation of the mechanisms responsible for mineral stabilization by CPP formation for two reasons. On the one hand it was found that the presence of particles below 10 nm influences the characteristics of SAXS data. Moreover, from FCS measurements it is known that different equilibria are forming in the CPP system in solution (compare chapter 4.4). Possibly, the scattering data are influenced by the process of equilibration and the exchange of individual molecules between different particle types in the solution. Up to now, no information on the time scale or the time dependence of those equilibria is available so that a distinct explanation of the connection between equilibration and scattering data is currently not possible.

The results obtained in the context of the present work lead to the assumption that the polydispersity of the CPPS and CPMs solution is either higher than expected up to now or that mineral-/protein-particles and aggregates with a broad size distribution are additionally present. However, data do not clearly indicate which hypothesis is true as both a broad size distribution and high polydispersities of a small number of present species can complicate data interpretation like observed in the present case.

Comparison of Results from SAXS with Results from previous FCS Measurements

The polydispersity of the second-state CPPs can also be addressed by means of FCS as shown in chapter 4.4 and section 6.6.3. FCS measurements of pure fractionated second-state CPPs revealed variations in CPP size of approximately 18 % (compare section 6.6.3). This indicates that polydispersity of the CPPs (and CPMs) cannot be the only reason for the difficulties in SAXS data interpretation. Hence, it can be assumed that the CPP-solution contains more than the two identified species (CPPs and CPMs) which for their part exhibit different polydispersities.

Different measurements additionally revealed that particle interaction with surfaces plays an important role in the investigated solutions. Adsorption phenomena could not only be observed for the cover slides used in FCS but for the glass surface of the *NanoSight particle analyzer* (NanoSight Ltd., Amesbury, Wiltshire, UK) as well. It must be assumed that at least a fraction of the particle types present in the CPP-solution can also adsorb to the glass surface of the measurement vessels used for SAXS, SLS and DLS. The ratio of surface to solution is much higher in the mark tubes used for SAXS compared to the NMR tubes used for 3D-DLS. Assuming that the amount of adsorbed particles depends on the surface area, different measurement vessels could affect the solution composition to different degrees. This in turn can influence the present equilibria and lead to varying solution compositions in different types of measurement vessels. A direct comparison of results from different measurement methods might therefore be problematic.

Small Particles/Structures significantly influence the Characteristics of the SAXS Form Factor

Despite all difficulties and remaining questions, data fitting using the NIST analysis package provided important evidence concerning the CPP-solution composition in second state: CPMs as well as potential additional small particle types or structures present in the CPP-solution must not be neglected in data interpretation although they are clearly smaller compared to CPPs. This can be explained by the large proportion of up to 97 % of the total fetuin-A and up to 50 % of the total mineral which is not incorporated in CPPs.⁴ The characteristics of the SAXS form factor is obviously considerably influenced by the small particles even though smaller structures seem not to affect 3D-DLS data in a significant manner. Currently, the fit results indicate the presence of small particles or additional structures in and below the size range of the CPMs. Particles and aggregates with different sizes consisting of protein and/or mineral are for example conceivable.

Fitting of the Experimental SAXS Data of the first-state CPP-Solution

In case of the CPP-solution in first state, the best fitting result under consideration of the known parameters was obtained by a combination of the spherical and the ellipsoidal form factor model. The experimental data and the related fit are shown in Figure 4.19.

Semi-axes lengths of $R_{a,1} = a_1 = 24$ nm and $R_{b,1} = b_1 = 56$ nm were obtained for the ellipsoid. Those values correspond to the values for the bigger ellipsoidal particles derived from fitting of the SAXS data of the second-state CPP-solution as shown above. A comparison of SAXS data of the first- and second-state CPP-solution showed that the characteristics at lower q are nearly independent of the CPP state (compare Figure 4.11). The reoccurring fitting result from this q -range is therefore reliable. However, it does not match previous 3D-DLS results, which provided significantly higher values (compare Table 4.4). The obtained values also lie below the values obtained from fitting with the *Size Distribution Program* (compare section 4.3.3.2).

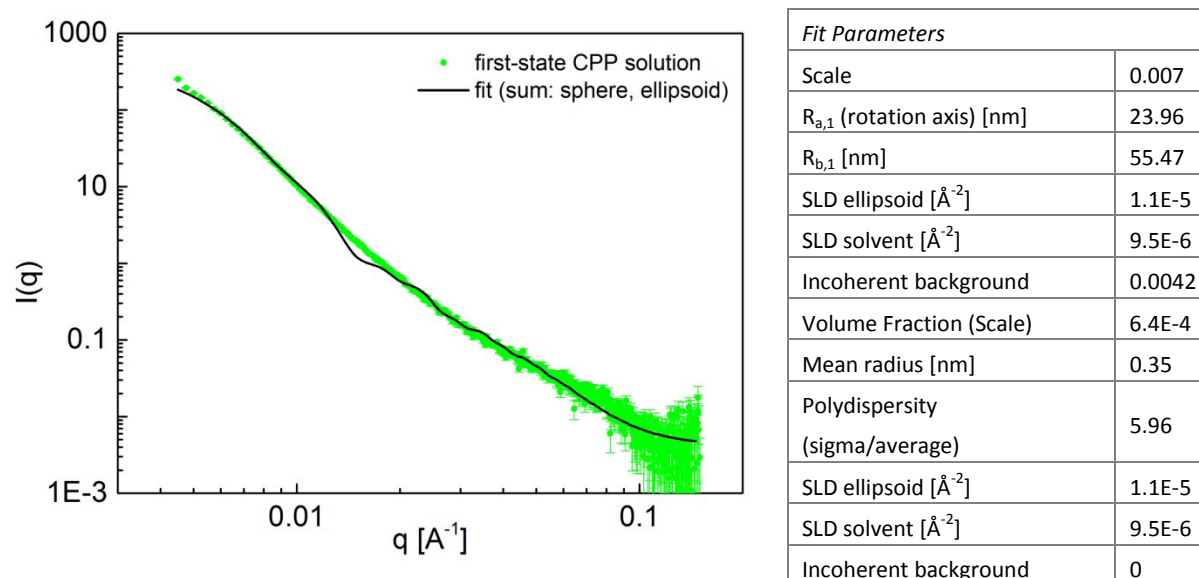


Figure 4.19: Left: Experimental data from a first-state CPP-solution with an initial fetuin-A concentration of $13.5 \mu\text{M}$ and related fit. Apart from the minimum at $q \approx 0.015 \text{\AA}^{-1}$ missing in the experimental data, the fit matches the experimental data relatively well. Right: Fit parameters. All SLDs as well as the background of the spherical particles were fixed in order to obtain the most reliable result. The remaining parameters shown in the box were obtained from fitting.

The obtained length of the rotation axis a is the smaller one implying that the ellipsoids have an oblate shape. This is in accordance with the fits of the second-state CPP-solution. Up to now, first-state CPPs were assumed to be spherical from TEM measurements.⁵ Hence, the result cannot satisfyingly be explained at the moment. Data evaluation using the *Size Distribution Program* has already shown that the interpretation of the results is not unambiguously possible at the moment. Obviously, the same holds true for the evaluation with the NIST package.

Previous measurements of CPP-solutions have shown the coexistence of CPPs and CPMs as mentioned before.²⁷ Hence, we hypothesized that the fits provide sizes in the range of the first-state CPPs ($50 \text{ nm} < R < 100 \text{ nm}$) and/or in the size range of the CPMs²⁷ (approximately around 3 nm). Neither the ellipsoidal nor the spherical particle characteristics derived from the fit match this hypothesis. While the values of the ellipsoidal particles lie in between both

species, the determined radius for the spherical particles is a tenfold smaller than expected for the CPMs. The fit provides a radius of only 0.35 nm instead of 3 nm for the spherical particles. In addition, the provided polydispersity of those particles is extremely high with a value of $\frac{\sigma}{\text{average}} \approx 6$. The scale factor indicates a tenfold higher amount of the bigger particles compared to the smaller particles. This can be excluded as SANS measurements showed that approximately one-half of the mineral and up to 97 % of the fetuin-A is not included in the CPPs.⁴ However, the scale results from fitting are not reliable as explained before.

Altogether, the results from fitting with the NIST analysis package do not match our hypothesis. Similar to the fitting with the *Size Distribution Program* no distinct particle size could be derived. The fit results indicate a broad size distribution of particles present in the first-state CPP-solution which is in accordance with what was found for the second state. Either the CPPs and CPMs contained in this state exhibit high polydispersity or the solution contains additional species exhibiting different polydispersities for their part. A high CPP polydispersity would contradict previous results from investigations on the polydispersity by means of dynamic light scattering.⁵

This is probably due to the differences in the measurement procedure and weighting in 3D-DLS and SAXS. In general, 3D-DLS measurements were exclusively performed at a scattering angle of 90° while SAXS measurements covered a broad q-range as shown above. Furthermore, the signal to noise ratio in 3D-DLS is worse compared to SAXS, so that 3D-DLS measurements are not expected to provide a more distinct size distribution even when measuring at different angles. Usual DLS provides a better signal to noise ratio. Anyhow, CPP measurements in usual DLS is complicated due to sample turbidity. Thus, CPP samples could only be measured in a diluted state. Up to now 3D-DLS measurements have shown that the overall diffusion coefficient of the CPP(2)-solution is not influenced by dilution. However, impacts on the transition process cannot certainly be excluded.

Furthermore DLS and SAXS measurements differ in the evaluated q-range. DLS measurements were performed at a q-value of 0.002 Å⁻¹, while SAXS measurements covered a q-range of 0.003 Å⁻¹ up to 0.15 Å⁻¹. Hence, in SAXS the evaluated q-range lies at higher q-values compared to DLS. The contribution of smaller particles to the average scattering signal decreases with decreasing q-range, so that the proportion of CPP scattering compared to the scattering of smaller particles is enhanced at low q-values. This difference explains the predominance of the CPP signal in DLS and its decreased contribution in SAXS, where the smaller particles significantly influence the characteristics of the form factor. This difference in q-range also contributes to the different results obtained from 3D-DLS and SAXS.

Altogether, a concluding characterization of the first-state CPP-solution on the basis of SAXS data and the available fitting routines is not yet possible.

Fitting of the Experimental SAXS Data of the CPP-Solution in Transition State

Scattering data of the CPP-solution in first and second state could not provide satisfying results. However, fitting of the SAXS curves from transition state was performed in the same manner. Fitting of a theoretical curve to the experimental data was also possible in this case. The best fit was received for the sum model combining the Gaussian sphere form factor and

the form factor of the uniform ellipsoid, which is the same combination as for the first-state CPPs. The data and the related fit are shown in Figure 4.20.

Fit and experimental data match quite well which is similar to the fits for the first and second state. The noise around $q=0.03 \text{ \AA}^{-1}$ is an artifact of the numerical integration, which can occur when large length scales are present in the system. It does not affect the results. The specific lengths obtained from the fit differ a lot from what has been obtained for fitting of first- and second-state CPP data. For the axes of the ellipsoid fitting provides values of $R_a = a = 0.02 \text{ nm}$ for the rotation axis and $R_b = b = 139.8 \text{ nm}$. In this case, the axes ratio would be approximately 7000, which is not reasonable. The mean radius of the Gaussian sphere was determined as $R = 0.2 \text{ nm}$ with an extremely high polydispersity of 155. This is also not very reliable.

The obtained values are dominated by small length scales below 1 nm. Again, fitting indicates that either small particles are present or small substructures within the characterized particles (CPPs, CPMs) have a strong influence on the characteristics of the experimental scattering data. The scale factors are again little reliable.

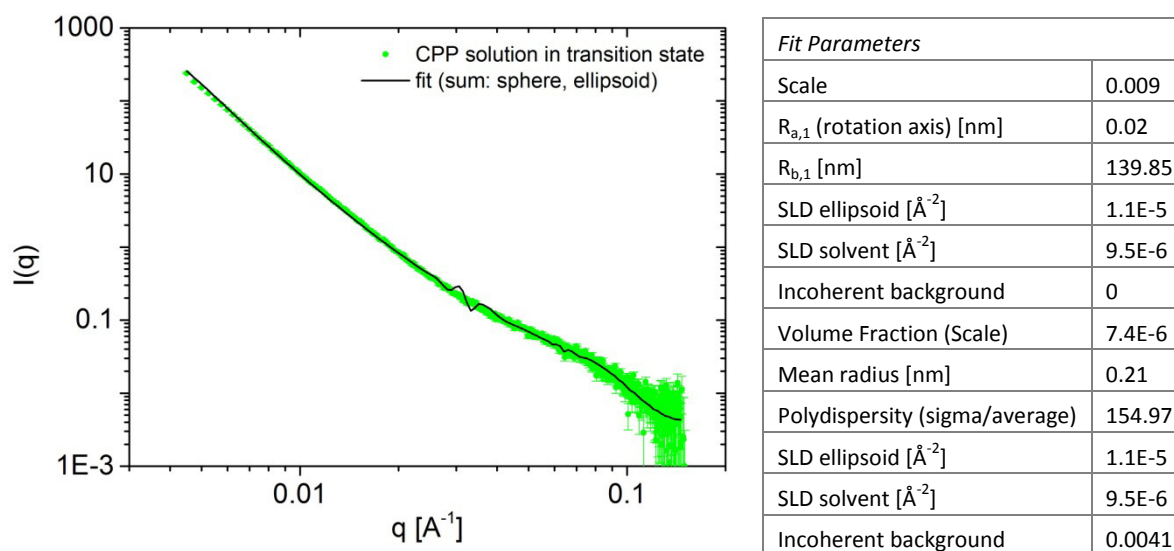


Figure 4.20: Left: Experimental result and related fit of SAXS data from a CPP-solution in transition state (initial fetuin-A concentration: $13.5 \mu\text{M}$). The fit matches the experimental data. The spikes around $q \approx 0.03 \text{ \AA}^{-1}$ can arise by combination of different models. They are therefore an artifact and do not affect the results of the fit. Right: Fit parameters. All SLDs as well as one of the two background parameters were fixed during fitting in order to obtain the most reliable fitting result. The remaining parameters shown in the box were obtained from fitting.

Analysis with the NIST software could not provide detailed insight into the CPP-solution content in the different states. This is similar to the analysis with the *Size Distribution Program*. With neither of the two fitting routines was the interpretation of the experimental scattering data satisfyingly possible. The obtained length scales were not consistent although the data in first and second state and even for the transition state were well fitable with the NIST package. Hence, an overall interpretation leading to the explanation of the occurring mechanism during CPP transformation is still not possible.

4.3.4 Conclusion: Time-dependent SAXS Measurements

Time-dependent scattering curves of the CPP-solution were recorded using SAXS. Time-resolution was adequate for tracking the CPP transition. The experimental data could be fitted using the *Size Distribution Program* as well as the NIST package based on IGOR Pro.

Neither of the two fit approaches used to fit the experimental data could provide detailed and reliable information on the occurring particle sizes and their distribution in the different states. It was not possible to obtain a reliable time-dependent developing of particle sizes and polydispersities. Currently available fitting routines are not sufficient to elucidate the fundamentals of transition on the basis of SAXS data. Structural rearrangements can only be assumed by the combination of the SAXS results with observations made with different additional methods. From fluorescence correlation spectroscopy (FCS) (see chapter 4.4) it is known that equilibration plays a major role within the CPP system. However, it can be assumed that several intermediate states can occur as various particles sizes are measureable in all investigated CPP states. This can be interpreted as indication for the transition from first to second state being a continuous process rather than an abrupt change. However, it is not clear whether the different particle types are solely present due to the transformation process. SAXS measurements of the CPP-solution in second state does just as little exhibit distinct characteristics as in the states before. Thus, it is additionally conceivable, that a distinct polydispersity of particles is present at all times. This remains to be clarified.

At present, it looks like the size distribution of the particles and their polydispersity plays a bigger role than hypothesized so far. Our measurements indicate that the polydispersity of the CPPs is relatively high, which is in contrast to what was supposed up to now. Additionally, polydispersity of the CPMs or the occurrence of smaller particles such as mineral-/protein-aggregates with different sizes is obviously non-negligible. It has to be clarified in which amount smaller structures are present in the CPP-solution and in which amount their composition and their proportion can vary as they seem to considerably contribute to the characteristics of the experimental scattering data. Furthermore, they probably play an important role in the occurring equilibration mechanisms. These mechanisms can also be influenced by particle adsorption onto the surface of the measurement vessels. This means that measurements using different vessels could potentially provide different results. However, it is not yet clear whether only smaller particles contribute to the small sizes provided by the fit or whether this result is (also) caused by the internal structure of the bigger particles (in particular the CPPs).

Fitting with the NIST package indicates that second-state CPPs are rather oblate than prolate as indicated from previous electron micrographs.⁵ This result remains to be checked and explained.

Altogether, the static SAXS measurements were not sufficient to explicitly describe the different CPP states and the particular particle sizes present in the different states. Just as little did the elucidation of the fundamentals of CPP transition succeed with the chosen approach. Up to now, a major part of findings concerning the CPP structure and the composition of the CPP-solution in the different states was obtained using small-angle scattering in the form of SANS with contrast variation. This offers the possibility of increasing or decreasing the scattering ratio of selected fractions present in the solution. In the present

case, SAXS was chosen to elucidate the transformation process with a high time resolution which is unavailable with SANS. However, the proportion of small structures, particles and/or aggregates of protein and/or mineral obviously influences the form factor so dramatically, that the advantage of high time-resolution cannot be utilized. The exact solution composition is obviously not accessible with conventional SAXS alone. Hence, an additional approach was chosen measuring the CPP samples under flow conditions rather than in a static capillary. The results of those measurements are described in the following (section 4.3.5).

4.3.5 Results and Discussion: CPP Measurement under Flow Conditions

We measured the CPP-solution in a micro fluidics system under flow conditions in addition to the approach described before. The idea was to use enforced orientation of the CPPs to investigate the changing geometry of the CPPs with time.

Particles align within the flow direction depending on flow velocity and particle shape, provided that the flow forces exceed the intrinsic rotation of the anisotropic particles. The intrinsic rotation of a particle depends on the solvent viscosity, the temperature and the axial ratio in case of ellipsoidal particles. Hence, it decreases with decreasing temperature and decreasing axial ratio and increases with decreasing solvent viscosity (detailed calculations are described in the work of O. De Castro¹⁴⁹).

Alignment and therefore anisotropic scattering shall in principle become visible as soon as the CPPs become anisotropic. The bigger the particles the smaller velocity is necessary for enforced orientation. Therefore, CPP alignment should occur at smaller velocities compared to the alignment of smaller particles like CPMs, so that an independent investigation of the CPPs is in principle possible. The determination of the orientation distribution during transition can be used as basis to clarify the underlying mechanisms responsible for transformation.

4.3.5.1 Scattering Pattern of the CPP-Solution under Flow

In a first approach, the normalized scattering pattern of a second-state CPP-solution with an initial fetuin-A concentration of 13.5 μM measured at a flow velocity of $l_V = 17$ ml/min was compared to the scattering pattern of itself measured with the pump switched off ($l_V = 0$ ml/min). For the flow velocity of $l_V = 17$ ml/min the Péclet number was roughly estimated with $Pe = 60$ while the Reynolds number was $Re \approx 650$ at a temperature of $T = 297.15$ K and a diameter of the measurement cell of 0.6 mm. The Reynolds number was clearly below the critical Reynolds number of $Re_{crit} = 2300$ to ensure laminar flow conditions (compare section 4.3.2.2). The values calculated for different velocities and temperatures can be found in the master thesis of O. De Castro.¹⁴⁹ The scattering patterns obtained for the second-state CPP-solution at a velocity of $l_V = 0$ ml/min and $l_V = 17$ ml/min are shown in Figure 4.21.

The reflexes in both pictures are artifacts caused by X-ray scattering at the walls of the capillaries used for measurement. Those reflexes were detected for all measurements performed with the micro fluidics setup. However, the reflexes occur in the area in which scattering of the anisotropic particles should become visible with particle alignment. Hence, the reflexes impede an exact data evaluation. Irrespective of the exact reasons, the

scattering patterns obtained under flow and without flow do not show any distinct differences. Anisotropy is not visible in either of the simple scattering patterns. The same holds true for the CPP-solution in first state as no significant difference in the scattering pattern of the CPP-solution in first and second state was visible to the naked eye.

This result led to another approach of data treatment described in the following section. Difference scattering patterns were calculated and used for further analysis instead of analyzing the mere scattering patterns.

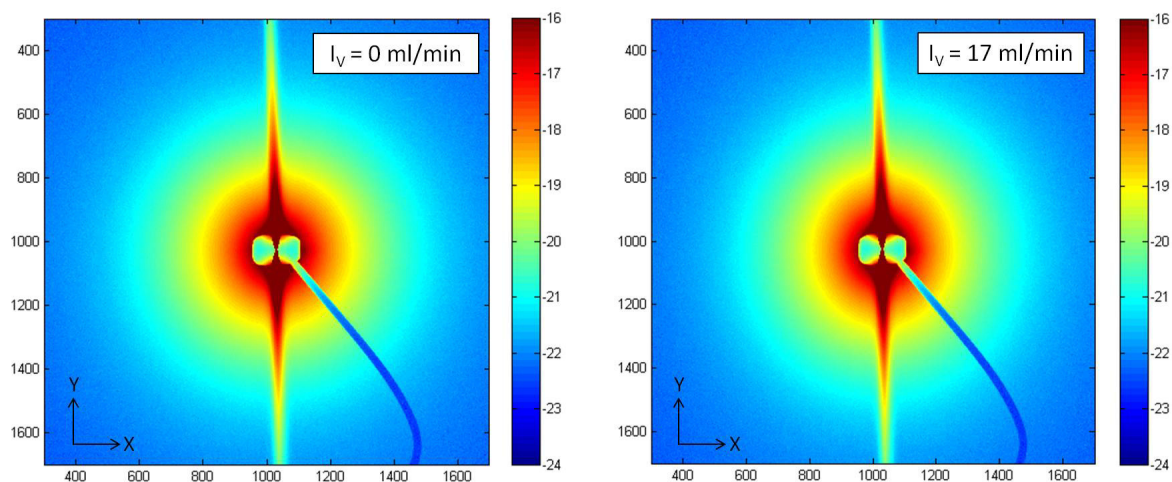


Figure 4.21: Normalized scattering patterns of second-state CPP-solution with an initial fetuin-A concentration of $13.5 \mu\text{M}$. Left: Measurement in micro fluidic setup with switched off pump ($I_V = 0 \text{ ml/min}$). Right: Measurement in micro fluidic setup with a flow velocity of $I_V = 17 \text{ ml/min}$.

4.3.5.2 Analysis of Difference Scattering Patterns

Due to the fact that the individual scattering patterns did not exhibit distinct differences, difference scattering patterns were calculated in order to check CPP alignment and to investigate time-dependent changes in CPP morphology. In a first step of the analysis of difference scattering patterns, the normalized scattering pattern of a second-state CPP-solution with an initial fetuin-A concentration of $13.5 \mu\text{M}$ measured at a flow velocity of $I_V = 17 \text{ ml/min}$ was corrected with the scattering pattern of itself measured at $I_V = 0 \text{ ml/min}$ (both are shown in Figure 4.21). The resulting difference scattering pattern calculated by O. De Castro¹⁴⁹ is shown in Figure 4.22.

The difference scattering pattern shows an anisotropic pattern clearly indicating that at least a fraction of the particles is aligned at a flow velocity of $I_V = 17 \text{ ml/min}$. Based on previous TEM results⁵ we conclude that the anisotropic particles aligned in the micro fluidic setup are the second-state CPPs. Further analysis of those data including the computation and comparison of the resulting scattering curves is currently done in the context of a PhD thesis in the group of Prof. Klemradt at RWTH Aachen University (Mark Servos, PhD thesis, in progress). Nevertheless, these measurements show the first promising results in elucidating the particle development during CPP transition under flow conditions.

In a next step, CPP-solution was transferred into the micro fluidics cycle directly after mixing of all components. Hence, all CPP states from the initial state via transformation to the second state were measured time-dependently under flow conditions in the micro fluidics

setup. For those measurements, two different approaches of calculating difference scattering patterns were performed.

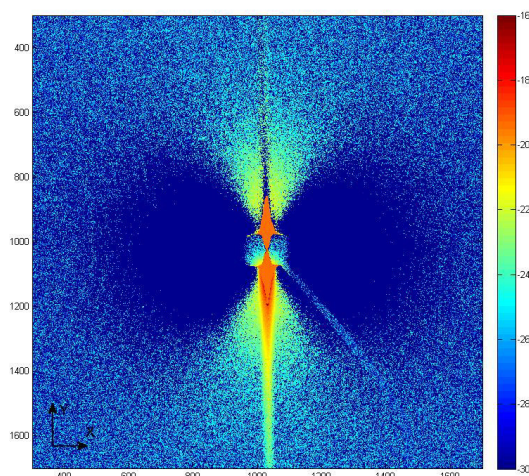


Figure 4.22: Difference scattering pattern of second-state CPP-solution with an initial fetuin-A concentration of $13.5 \mu\text{M}$. The scattering pattern measured in the micro fluidic setup at $l_v = 0 \text{ ml/min}$ was subtracted from the scattering pattern measured in micro fluidic setup with a flow velocity of $l_v = 17 \text{ ml/min}$.

In the first approach, the scattering pattern of the first-state CPPs was subtracted from the scattering pattern of the CPP-solution at different points in time. Hence, a change in particle anisotropy and simultaneous particle alignment would lead to a time-dependent change of the difference scattering patterns. The moment of beginning alignment and with that the moment of beginning CPP elongation should be determinable with that procedure. All scattering patterns were recorded at a flow velocity of $l_v = 17 \text{ ml/min}$. The calculated scattering patterns are shown in Figure 4.23.

The most important difference provided by comparing the difference scattering patterns measured at different time-points before, during and after CPP transformation is the increasing overall intensity. This phenomenon was already known from the static measurements performed at beamline B1. From 3D-DLS measurements it was additionally known that the scattering intensity of the CPP-solution increases with proceeding transformation.

The area of no intensity within the small q -range below approximately $q = 8 \cdot 10^{-3} \text{ \AA}^{-1}$ (marked with the red circle in Figure 4.23, picture B) evolves from the subtraction of the patterns. For the respective q -range the intensity of the ellipsoidal second-state CPPs is expected to lie below the intensity of the spherical first-state CPPs. This was estimated from the theoretical scattering curves of a spherical particle with a radius of 60 nm and an ellipsoidal particle with $a = 133 \text{ nm}$ and $b = 40 \text{ nm}$ (Figure 4.23, picture I). The values for the calculation of the theoretical curves were chosen on the basis of typical CPP axes lengths calculated from 3D-DLS measurements.^{5,148}

The theoretical curves also show that the expected intensities for the primary and the secondary CPPs are similar over the whole investigated q -range, which complicates data interpretation. Another difficulty in data interpretation is the again appearing capillary reflexes. Particle anisotropy is not detectable with that procedure of difference scattering pattern calculation, although an intensity increase is visible in the shown data.

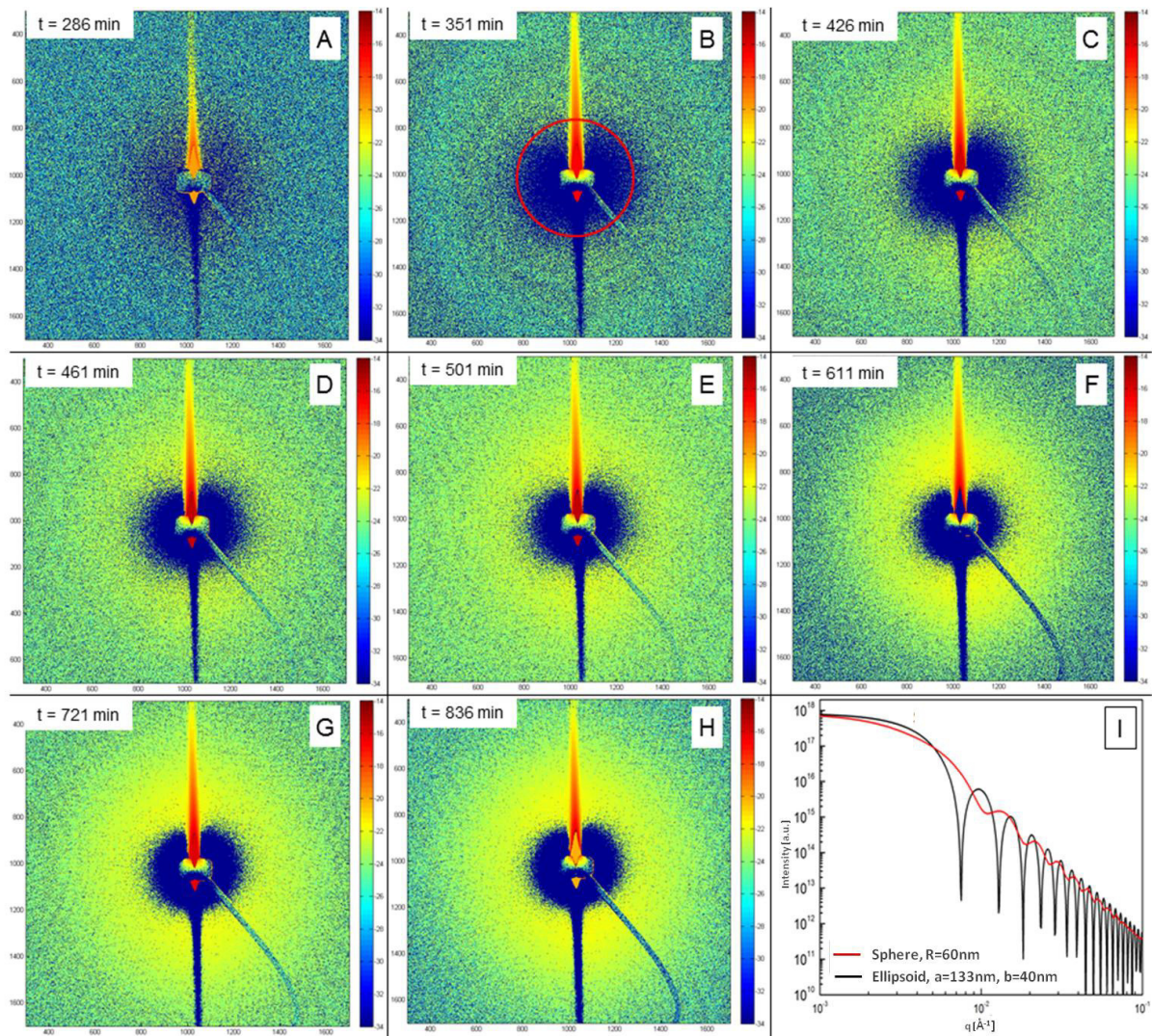


Figure 4.23: Scattering patterns from measurement with a flow velocity of $I_v = 17$ ml/min. A: Reference scattering pattern of CPP-solution in first state with an initial fetuin-A concentration of $13.5 \mu\text{M}$. B-H: The difference scattering patterns were obtained by subtraction of scattering pattern A from scattering patterns measured at different time-points before, during and after CPP transition. The red circle in picture B shows the q -range of smallest intensity after subtraction of the patterns. This low intensity is caused by the subtraction of two patterns exhibiting similar intensities in the respective q -range. I: Theoretical scattering curves of spheres with a radius of $R = 60$ nm (black) and ellipsoids with $a = 133$ nm and $b = 40$ nm (red) for particles with isotropic orientation.

As a consequence, another approach of difference scattering pattern calculation was applied. Therefore the scattering pattern of a second-state CPP-solution measured in the microfluidics cycle with a flow velocity of $I_v = 4$ ml/min was subtracted from the scattering patterns measured at different time points with a flow velocity of $I_v = 17$ ml/min. Particle alignment generally increases with increasing velocity (in the laminar region which was ensured in the present case). Hence, this second approach of calculating difference scattering patterns was chosen in order to reduce the scattering signal of unaligned particle fractions present in the detection volume. The resulting scattering patterns are shown in Figure 4.24. For the calculations, the same scattering patterns were used as for the calculation shown in Figure 4.23.

The increased intensities around the beamstop especially in the pictures A-F in Figure 4.24 have the same reason as the extremely low intensities at the same area described for the

subtraction method before. In the present case, the opposite happens: the smaller intensity of the subtracted pattern in the respective q -range leads to a high overall intensity in the corresponding detector region (compare to Figure 4.23, picture I).

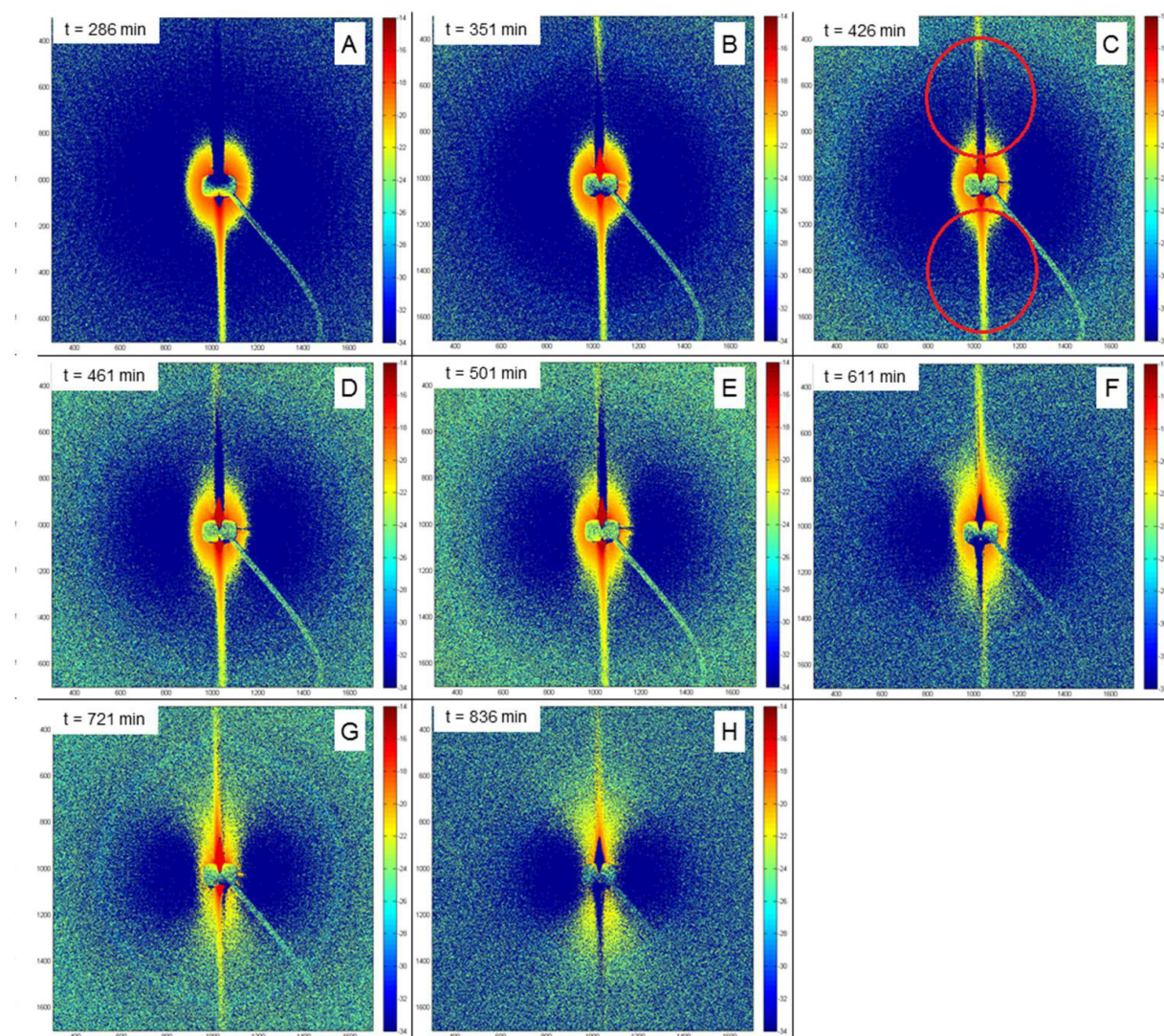


Figure 4.24: A-H: Difference scattering patterns of a CPP-solution in different states with an initial fetuin-A concentration of $13.5 \mu\text{M}$. Difference scattering patterns were obtained by subtraction of the scattering pattern of the second-state CPP-solution measured at a flow velocity of $I_V = 4 \text{ ml/min}$ from the scattering patterns measured at different time-points before, during and after CPP transition with a flow velocity of $I_V = 17 \text{ ml/min}$. The red circles in picture C mark the area in which the difference scattering pattern significantly changes with time starting at a time of $t = 426 \text{ min}$.

However, a comparison of the difference scattering patterns at different times reveals a considerable time-dependent change in intensity. Those changes are particularly pronounced in the area highlighted with the red circles in Figure 4.24, picture C. Starting in picture C (426 minutes after sample preparation), the anisotropic scattering intensity increases with increasing time. Especially towards the end of the measurement, that is in second-state CPP-solution, the anisotropic scattering is very pronounced (pictures G and H). This is due to the (at least partial) alignment of the CPPs with increasing anisotropy. Similar to the analysis approach subtracting the measurement without flow (shown in Figure 4.22), it is also possible to calculate significant difference scattering patterns by subtraction of the scattering pattern of a second-state CPP-solution measured in the micro fluidics cycle with a flow

velocity of $v_V = 4$ ml/min. This velocity is considerably below $v_V = 17$ ml/min but beyond the static conditions without enforced flow. Both methods of calculating difference scattering patterns are promising for further elucidation of the CPP transformation process. Therefore, the existing data are under current analysis in the context of a PhD thesis in the group of Prof. Klemradt at RWTH Aachen University (Mark Servos, PhD thesis, in progress).

A modification in measurement is also imaginable apart from the analysis of existing data with the calculation and subsequent analysis of difference scattering patterns. A decreased temperature leads to a decrease in fluid viscosity on the one hand. On the other hand, the rotational diffusion of the particles counteracting the particle alignment by enforced flow is also temperature-dependent (compare considerations in the context of the flow-cell design by O. De Castro¹⁴⁹) and decreases with decreasing temperature. The decrease in both factors leads to an increase in the product of the local Reynolds number Re_l and the local Péclet number Pe_l and thus to an enhanced alignment of the particles with the flow. The decreased temperature has the additional advantage of a deceleration of the transition process leading to a better time-resolution for the investigation of the whole CPP transformation under flow conditions.

First tests with a decreased temperature of 287.15 K instead of 297.15 K have already been performed but did not show considerable effect on the scattering patterns. Hence, further measurements with varying temperature are necessary to elucidate the temperature effect. In this case, the exact knowledge of the solution composition and the CPP shape could also help to calculate more exact values of the rotational diffusion and the respective parameters (Péclet number, product of the local Reynolds number Re_l and the local Reynolds number Pe_l) in order to choose the best possible conditions for CPP alignment.

4.3.6 Conclusion: CPP Measurement under Flow Conditions

SAXS measurements of the CPP-solution in the micro fluidics setup under flow conditions show time-dependent changes in CPP anisotropy. However, further data analysis is necessary to reliably elucidate the anisotropy development during CPP transformation. It was shown that the calculation and analysis of difference scattering patterns is very promising for that purpose. The existing data are currently analyzed in the context of a PhD thesis in the group of Prof. Klemradt at RWTH Aachen University (Mark Servos, PhD thesis, in progress). Detailed evaluation of the transformation process will be the basic step for understanding the fetuin-A mediated mineral stabilization by the formation of CPPs.

4.3.7 Outlook

Altogether, the mechanism of CPP transformation and the underlying mechanisms for mineral stabilization by fetuin-A remain incompletely explained, although several approaches in the direction of elucidation of the morphological CPP changes have been made.

An extremely promising approach is the measurement of the CPP-solution under flow conditions. The results indicate that the proper choice of the flow velocity followed by an adequate analysis method (in particular the calculation of difference scattering patterns) can be applied to monitor anisotropy changes in the CPP-solution. An elucidation of the time-dependency of those changes will help to comprehend the morphological changes of the

CPPs during transformation. Thus, a detailed evaluation of the existing scattering patterns will be an important step in order to understand the mechanism of mineral stabilization by fetuin-A.

The detailed composition of the CPP-solution at different times and for different fetuin-A to mineral ratios has to be clarified for future investigations and data fitting. A possibility for approaching the question of solution composition is the performance of gel filtration chromatography similar to the procedure described in chapter 4.4. Fractionation of the CPP-solution is possible with gel filtration chromatography. Hence, SAXS curves of the single fractions can be recorded if gel filtration chromatography is coupled to a synchrotron SAXS setup. The synchrotron setup is necessary as it enables short measurement times and thus the consecutive measurement of all fractions present in a CPP-solution at a given time. Subsequently, the solution composition can be elucidated in detail from those data. An unambiguous evaluation of the SAXS data from the whole CPP-solution will be feasible once the SAXS curves of the single fractions will be established. This is by now at least possible for the analysis of the more stable second-state CPP-solution.

Another approach using gel filtration chromatography can be to separate the second-state CPPs from the rest of the CPP-solution. If the scattering curve of the remaining solution is recorded, it can be subtracted from the scattering curves of the entire CPP-solution in order to obtain the mere CPP scattering. In principle, this procedure is possible at any time providing that the solution measurement is fast enough so that equilibration and with that a change in the solution composition cannot occur.

The described measurements are for example possible at so-called BioSAXS beamlines enabling the measurement of small amounts of (relatively weak-scattering) biological material in a relatively short time as used for the fetuin-A shape determination (compare chapter 4.2). A facility enabling this type of measurement is the new BioSAXS beamline P12 at the PETRA III (Positron Elektron Tandem Ring Anlage) storage ring at DESY, Hamburg. The final clarification of the detailed composition of the CPP-solution at different times should be in principle possible with those measurements.

Furthermore, investigations on the adsorption behavior of fetuin-A and the additional components present in a CPP-solution are necessary in order to clarify the influence of particle adsorption on solution composition and equilibration. For those measurements, it is possible to use methods like AFM (atomic force microscopy), fluorescence methods, ellipsometry or mass spectrometry such as ToF-SIMS (time of flight secondary ion mass spectrometry).

It will be possible to understand the different states of the CPP-solution from the described approaches. This knowledge will help to clarify the fundamentals of transition and thereupon to explain potential structural rearrangements as well as the underlying processes. Those information will finally lead to the elucidation of the fetuin-A mediated mineral stabilization by the formation of CPPs.

4.4 Dynamic Exchange of Fetuin-A with colloidal Calciprotein Particles studied by means of two-color two-focus Fluorescence Correlation Spectroscopy

4.4.1 Introduction

The plasma protein fetuin-A is a potent systemic inhibitor of soft tissue calcification in vertebrates.^{7,16} The extracellular fluids exhibit calcium and phosphate supersaturation, thus stabilization mechanisms are required to avoid unwanted ectopic calcifications.

In vitro studies have shown that fetuin-A prevents mineral precipitation by forming protein-mineral complexes. On the one hand, mineral prenucleation clusters become captured by fetuin-A monomers while on the other hand formation of bigger colloidal particles occurs. According to their composition, the latter were named Calciprotein Particles (CPPs).^{3,27,161} Reference measurements using the same supersaturated system lacking fetuin-A show almost instantaneous mineral precipitation.^{3,16}

CPPs change their morphology with time. Time-resolved small-angle X-ray scattering (TR-SAXS) with stopped-flow analysis revealed that the formation of the initial particles, called primary or first-state CPPs, occurs in a fraction of one second.²⁶ Primary CPPs are spherical colloids with a hydrodynamic radius in the range of 50-80 nm. Their internal structure is amorphous, consisting of calcium phosphate and fetuin-A.²⁶ After a distinct lag time, which greatly depends on temperature and the mineral to protein – ratio, primary CPPs undergo a morphological change towards larger prolate ellipsoids with radii in the range of 90-120 nm.^{4,148} Parallel to the change in size and shape, the heterogeneous structure converts into a core of octacalcium phosphate (OCP) surrounded by a fetuin-A monolayer.⁴ Secondary or second-state CPPs are stable for at least two days. The same studies showed that a lower limit of 7 μM exists for the fetuin-A concentration, below which stabilization of the supersaturated solution is insufficient to prevent mineral precipitation.⁵

Nevertheless, Small-Angle Neutron Scattering (SANS) revealed that even close to this stability threshold only approximately 50 % of the mineral and only 5 % of the fetuin-A are contained in the CPPs.²⁷ This study uncovered a second, simultaneously occurring stabilization mechanism involving monomeric fetuin-A (see Figure 4.25). Fetuin-A monomers were found to associate with prenucleation clusters reminiscent of Posner clusters forming Calciprotein Monomers (CPMs).²⁷

In vitro findings can help to better understand biomineralization processes in vivo. The relevance is given by the fact that pathological calcium phosphate colloids reminiscent of CPPs have been shown to form in the ascites of a peritoneal dialysis patient.^{4,5} The results of a recent study likewise suggest that sera of hemodialysis patients might possess reduced intrinsic properties to inhibit calcification.¹⁶² The relevance of calcifications for patient morbidity and mortality shows the importance of elucidation and understanding mineralization processes and inhibition mechanisms.

Moreover, as proteins like fetuin-A involved in biomineralization processes became optimized for the interaction with the mineral-surface throughout evolution, they are interesting candidates for the production of biocomposites with novel and unique performance. The native bovine fetuin-A serves as ideal prototype for a biomineralization protein.

Furthermore, the combination of the prototypic fetuin-A and the reproducible process of CPP formation and transformation provides an excellent system for fundamental research and applications in the field of biomineralization.^{163–166}

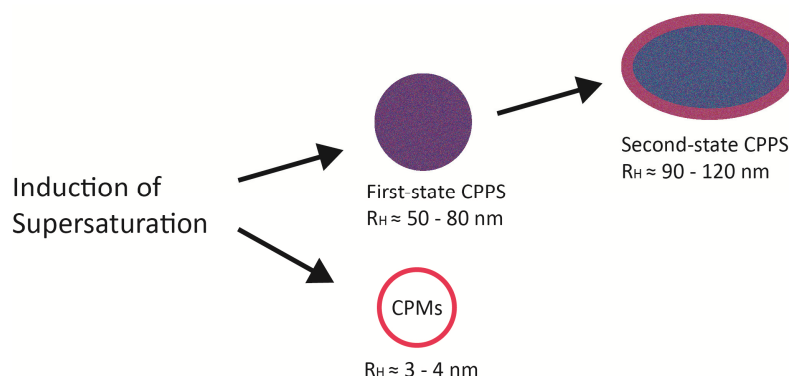


Figure 4.25: Stabilization of calcium phosphate in the presence of fetuin-A: simultaneous formation of Calciprotein Particles (CPPs) and Calciprotein Monomers (CPMs). Calciprotein complexes not drawn to scale.

The present study aims at further understanding the second-state CPP stability. More precisely, the ability of second-state CPPs to interact with free fetuin-A molecules is investigated. A combination of two-color fluorescence correlation spectroscopy (FCS) and dynamic light scattering (DLS) was employed to study whether fetuin-A bound to the CPP-surface exchanges with unbound, free fetuin-A in solution. These studies shall give new insight in the stability of the fetuin-A-CPP system *in vitro*.

While DLS provides information on the diffusion coefficient of the ensemble of particles forming the investigated system, FCS is based on single-molecule detection. Therefore, FCS is more sensitive to changes affecting not necessarily all species but only a minority of molecules. FCS provides the possibility to investigate a distinct particle fraction in a given environment by selective labeling. DLS measurements are used complementarily to monitor the impact of environmental changes affecting the entire investigated system rather than only one particle fraction. In our case, a combination of both methods is necessary to elucidate the occurring phenomena in the complex system of calcium phosphate stabilization in the presence of fetuin-A.

For investigating the process of fetuin-A exchange at the CPP surface, a two-color two-focus-FCS (two-color 2f-FCS) setup is used. With two-color FCS it is possible to simultaneously follow the individual diffusion characteristics of two differently labeled fluorescent species as well as their common diffusion when bound to the same particle. The technique was first described by Schwille et al. in 1997.¹⁶⁷ By labeling CPP-bound fetuin-A and free fetuin-A with different fluorescent labels it becomes possible to investigate fetuin-A exchange at the surface of second-state CPPs.

Previous *in vitro* studies have shown that the CPP formation is only one of the processes occurring in supersaturated mineral solutions.^{3,27,161} Thus, second-state CPPs are one of different species present in the solution.

Therefore, CPPs had to be separated from the rest of the solution to allow for their selective investigation. At the same time it was necessary to find a solution providing stability for the second-state CPPs and preventing their disaggregation due to equilibration processes. Hence, a complex separation process based on several steps of gel filtration chromatography was

developed in the context of the present work. Finally, we could monitor the exchange of CPP-bound fetuin-A and free fetuin-A in solution by means of two-color FCS and DLS.

4.4.2 Results and Discussion

4.4.2.1 Stability of fractionated second-state CPPs in different Solutions

For conducting experiments probing the exchange of free fetuin-A and CPP-bound fetuin-A it was necessary to use an environment, in which the fractionated second-state CPPs are stable. At the same time, an exchange of free fetuin-A and CPP-bound fetuin-A has to be possible. Hence, we separated the second-state CPP fraction from the rest of the solution in a first step and checked their stability using FCS.

For this purpose, CPPs were formed and transformed using the so-called inhibition mix. The inhibition mix consists of fetuin-A and buffer substances as well as Na_2HPO_4 and CaCl_2 necessary for CPP formation. The detailed procedure is described in the Experimental Section.

Fluorescently labeled CPPs are required for subsequent FCS measurements. This was achieved by using Alexa647-labeled fetuin-A for CPP formation. After CPP transformation into the second state, we obtained a solution containing second-state CPPs as well as CPMs and the remaining salts, mineral and protein. We named this solution CPP(2)-solution. All fetuin-A containing species carried the Alexa647-label. The CPP(2)-solution was fractionated using size exclusion chromatography. The second-state CPP fraction was separated from the CPP(2)-solution and collected.

On the one hand, we investigated the mere second-state CPP fraction (undiluted as received from gel filtration chromatography or diluted in water, respectively). On the other hand we investigated the stability of the second-state CPPs in different solutions containing buffer substances: (i) pure TBS, (ii) TBS containing 0,98 g/l fetuin-A and (iii) a CPP(2)-solution. For this purpose, after gel filtration chromatography, the fractionated second-state CPPs were collected in an empty collection tube or in a collection tube prefilled with one of the three mentioned solutions (collecting fluids, see Figure 4.26). All obtained solutions were investigated with FCS to determine the diffusion coefficient of the labeled fractionated second-state CPPs. This procedure allowed us to elucidate the impact of the respective solution on the stability of the second-state CPPs.

Under all tested conditions, stability of the second-state CPPs could only be observed when a CPP(2)-solution was prefilled in the collection tube. In all other cases, the obtained correlation functions showed a multiple-step decay indicating a broad range of diffusion coefficients and thus the presence of various particle sizes in the solution. This, however, impeded unambiguous data evaluation.

Previous measurements had already indicated the existence of an equilibrium between CPMs and second-state CPPs (see Figure 4.27). Therefore, we assume that in the present case the separated CPPs (partially) disaggregate into smaller particles, especially CPMs, or aggregate to larger entities.

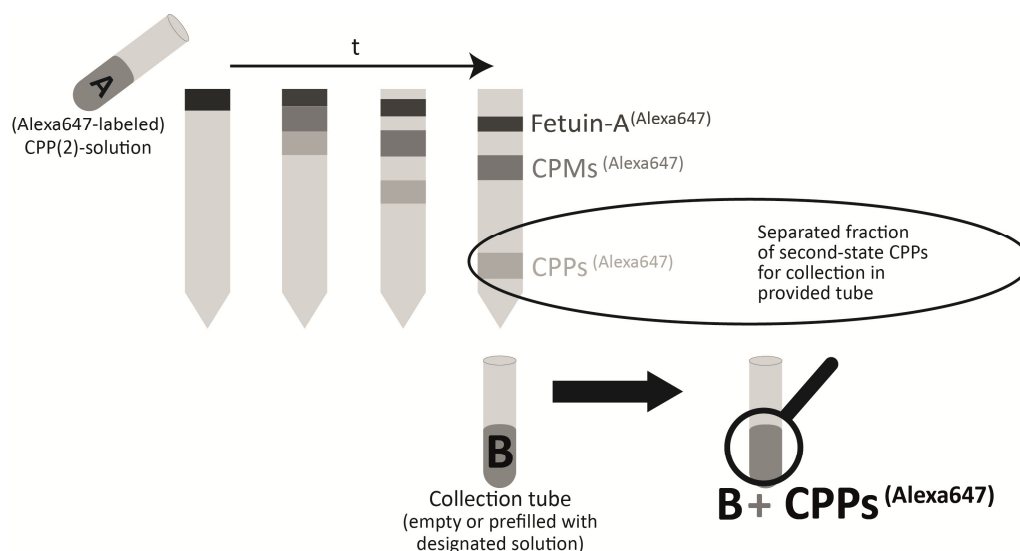


Figure 4.26: Separation of the fractionated second-state CPPs from the CPP(2)-solution (A) using gel filtration chromatography. For further investigations, the separated second-state CPP fraction was collected in a collecting tube (B). Depending on the respective experiment, we used an empty tube or a collecting fluid (water; TBS buffer; fetuin-A containing TBS buffer; unlabeled, unfractionated CPP(2)-solution) for the collection of fractionated second-state CPPs.

Experiments were usually performed some hours after separation of the second-state CPPs. Hence, we assume that the equilibrium between CPPs and CPMs establishes in a time range of minutes to hours.

Our findings suggest aggregation and disaggregation of separated second-state CPPs in water as well as in TBS with and without fetuin-A. Thus, water as well as TBS (with and without additional fetuin-A) is not suited for stabilizing the second-state CPPs against aggregation and disaggregation.

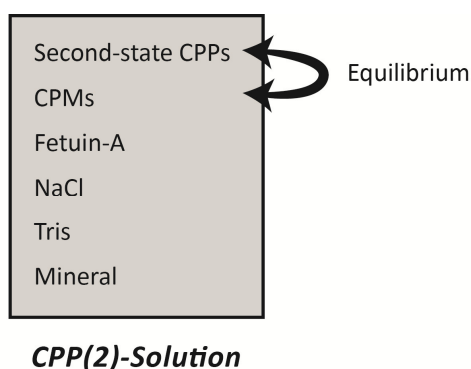


Figure 4.27: The establishment of an equilibrium between CPPs and CPMs is one reason for the instability of the fractionated second-state CPPs in water.

However, a CPP(2)-solution prepared under the same conditions but with unlabeled fetuin-A was able to stabilize the fractionated second-state CPPs. FCS measurements of the CPP(2)-solution containing the Alexa647-labeled fractionated second-state CPPs in a 1:1 ratio resulted in distinct correlation functions as shown in Figure 4.28. Fitting these functions provided a mean diffusion coefficient of $D = (3.1 \pm 0.6) \mu\text{m}^2\text{s}^{-1}$ corresponding to a hydrodynamic radius of $R_H = (79.9 \pm 16.2) \text{nm}$. This is in very good agreement with 3D-DLS-measurements of the same sample: where a hydrodynamic radius of $R_H = (78.9 \pm 2.6) \text{nm}$

was obtained. Fractionated second-state CPPs can thus be stabilized by collecting them in a CPP(2)-solution.

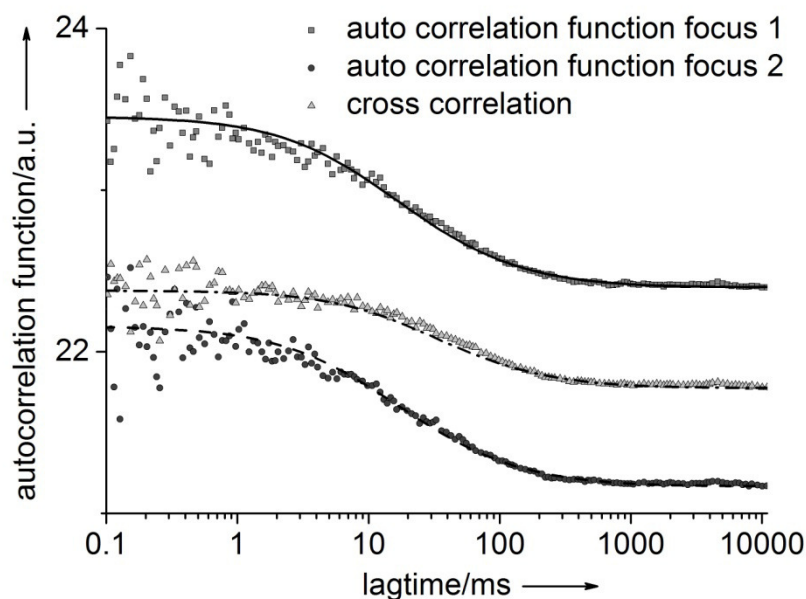


Figure 4.28: Two-focus correlation functions of labeled second-state CPPs in an unlabeled CPP(2)-solution; symbols: auto- and cross-correlation functions from FCS measurement, (dashed) lines: fitted functions. Fitting provides the diffusion coefficient of the labeled species.

4.4.2.2 Temporal Stability of second-state CPPs in a native CPP(2)-Solution

The goal of the present contribution is to probe the exchange of free fetuin-A and CPP-bound fetuin-A. For this exchange experiment, both species need to be stable for at least several hours in order to offer a preferably large period of interaction time to enable exchange.

To the best of our knowledge, the present contribution is the first to investigate the long-term stability of fractionated second-state CPPs. However, data on the stability of the unfractionated CPP(2)-solution are available revealing long-term stability of the CPP(2)-solution.^{5,148}

In the previous section, we showed that the fractionated second-state CPPs are at least short-time stable if collected in a CPP(2)-solution after separation by gel filtration chromatography. Based on the published 3D-DLS data dealing with the CPP(2)-solution and our findings concerning the short-term stability of fractionated second state CPPs we expect the fractionated second-state CPPs to be likewise long-term stable when collected in a CPP(2)-solution prepared under the same conditions.

For the investigations on the long-term stability, fractionated second-state CPPs were collected in a CPP(2)-solution after separation by gel filtration chromatography as described. Labeled fractionated second-state CPPs were collected in an unlabeled CPP(2)-solution for FCS measurements, while for DLS measurements all components were unlabeled. The diffusion coefficient was determined on at least three consecutive days using both FCS and 3D-DLS.

Both methods showed that the diffusion coefficients stayed constant over the whole observation time (see Figure 4.29) revealing long-term stability of the fractionated second-state CPPs in the CPP(2)-solution. The diffusion coefficients derived from both methods were

comparable. This demonstrates that the whole investigated system consisting of the fractionated second-state CPPs and the CPP(2)-solution is stable with time. Thus, the fractionated second-state CPPs collected in a CPP(2)-solution exhibit the required long-term stability to perform further investigations on the interaction between CPPs and free fetuin-A.

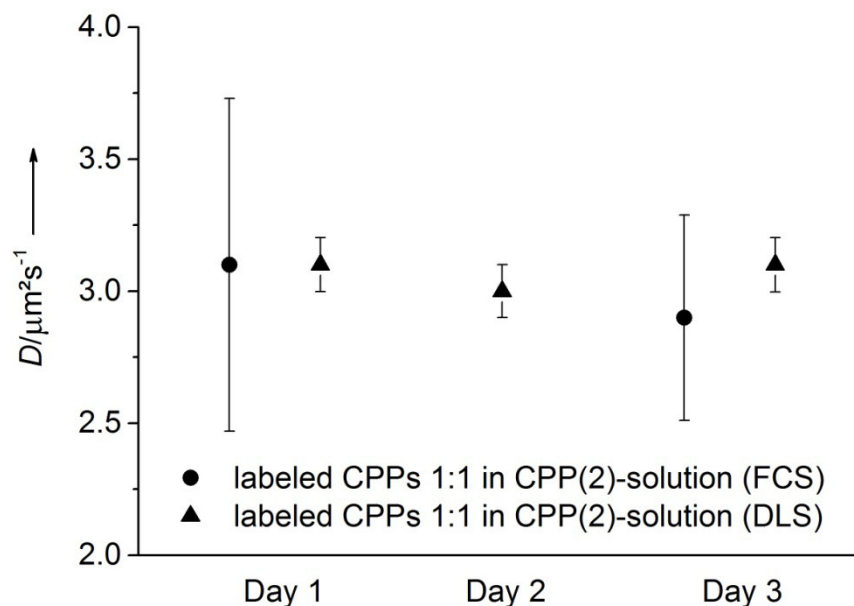


Figure 4.29: Diffusion coefficients of second-state CPPs in CPP(2)-solution observed at three consecutive days.

4.4.2.3 Temporal Stability of a CPP(2)-Solution containing additional free Fetuin-A

For conducting experiments probing the exchange of free fetuin-A and CPP-bound fetuin-A it is necessary to establish an environment providing stability to all components. We have shown above, that stability of fractionated second-state CPPs can be ensured by providing a CPP(2)-solution as environment. In addition to the second-state CPPs, free fetuin-A is necessary to prove a possible exchange with the CPP-bound fetuin-A. Thus, we tested the stability of the CPP(2)-solution in the presence of additional free fetuin-A using 3D-DLS.

For that purpose, a CPP(2)-solution was prepared as described above employing unlabeled fetuin-A. Afterwards, we added free, unlabeled fetuin-A (1 g/l). We studied the obtained solution as well as a 1:10 dilution thereof to check for a possible influence of dilution on particle size and stability. Diffusion coefficients were measured at five consecutive days to obtain information on the long-term stability of the solution. The results shown in Figure 4.30 demonstrate that the diffusion coefficient was unaffected by the addition of free fetuin-A to the CPP(2)-solution.

With 3D-DLS we determine the mean diffusion coefficient of the particles in solution. In the present case we basically see the diffusion coefficient of the second-state CPPs contained in the CPP(2)-solution. A time-independent stable diffusion coefficient thus shows that the second-state CPPs are unaffected by the presence of additional free fetuin-A. Obviously, the size of the particles stays constant revealing that no additional fetuin-A sticks to the CPP surface. Hence, formation of a fetuin-A multilayer on the CPP surface does not occur. The mean diffusion coefficient of the whole solution does not change significantly so that we can assume that none of the particles present in the CPP(2)-solution is affected by the presence of additional fetuin-A.

A subsequent dilution of the mixture also did not affect the solution stability. These findings showed that CPP(2)-solution containing additional free fetuin-A can be used as environment for further investigations on the interaction of free fetuin-A and second-state CPPs.

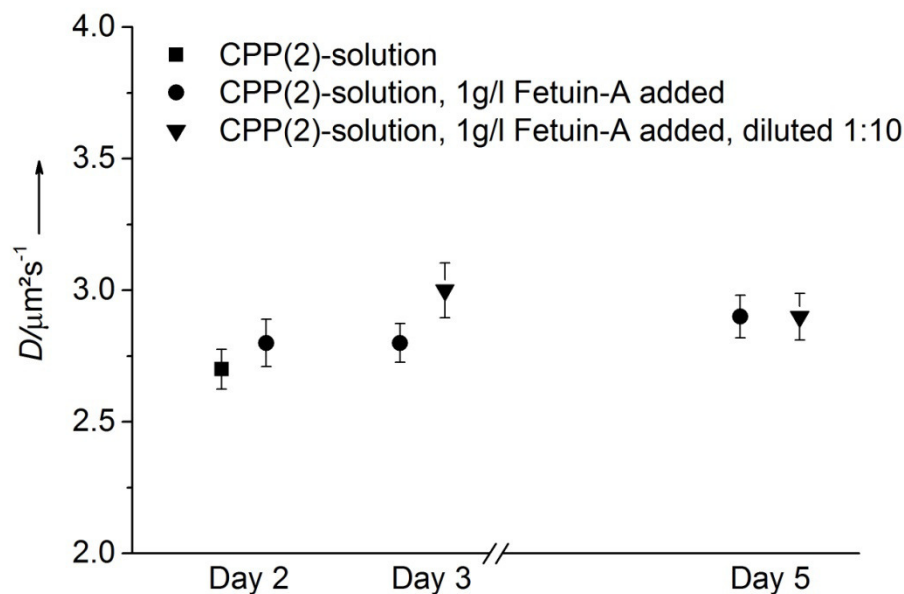


Figure 4.30: Diffusion coefficients of a pure, native CPP(2)-solution and a CPP(2)-solution containing additional 1g/l fetuin-A were determined with 3D-DLS at five consecutive days. Neither addition of fetuin-A nor subsequent dilution affected the diffusion coefficient significantly.

4.4.2.4 Preparing a Solution for the Investigation of the Exchangeability of free and CPP-bound Fetuin-A

In the next step, we combined the fractionated second-state CPPs, CPP(2)-solution and free fetuin-A in order to establish stability to all components necessary for further exchange experiments.

We prepared two inhibition mixes as described in the Experimental Section. We used (i) unlabeled fetuin-A for one inhibition mix leading to a CPP(2)-solution containing unlabeled species (fetuin-A, CPPs, CPMs) and (ii) Alexa647-labeled fetuin-A was used for the second mix to prepare a CPP(2)-solution containing Alexa647-labeled species (fetuin-A, CPPs, CPMs). The gel filtration chromatography column was loaded with the Alexa647-labeled CPP(2)-solution.

The unlabeled CPP(2)-solution was used as collecting fluid for collecting the Alexa647-labeled, fractionated second-state CPPs from gel filtration chromatography. Before collection of the fractionated second-state CPPs we added 1 g/l Alexa488-labeled fetuin-A to the provided CPP(2)-solution. The procedure is shown in Figure 4.31. Finally, we obtained a CPP(2)-solution containing Alexa488-labeled free fetuin-A as well as Alexa647-labeled second-state CPPs. We named this mixture the interaction-solution: the unlabeled CPP(2)-solution stabilizes the separated second-state CPPs, while the additional free Alexa488-labeled fetuin-A serves as potential exchange partner for the Alexa647-labeled fetuin-A bound to the CPP-surface.

The interaction-solution was kept at room temperature for three hours and afterwards stored in the fridge over night (altogether 20 h exchange time). Therewith, we ensured a

time frame, in which an exchange of bound fetuin-A and free fetuin-A could have occurred. In that case, CPPs should carry both Alexa-labels afterwards.

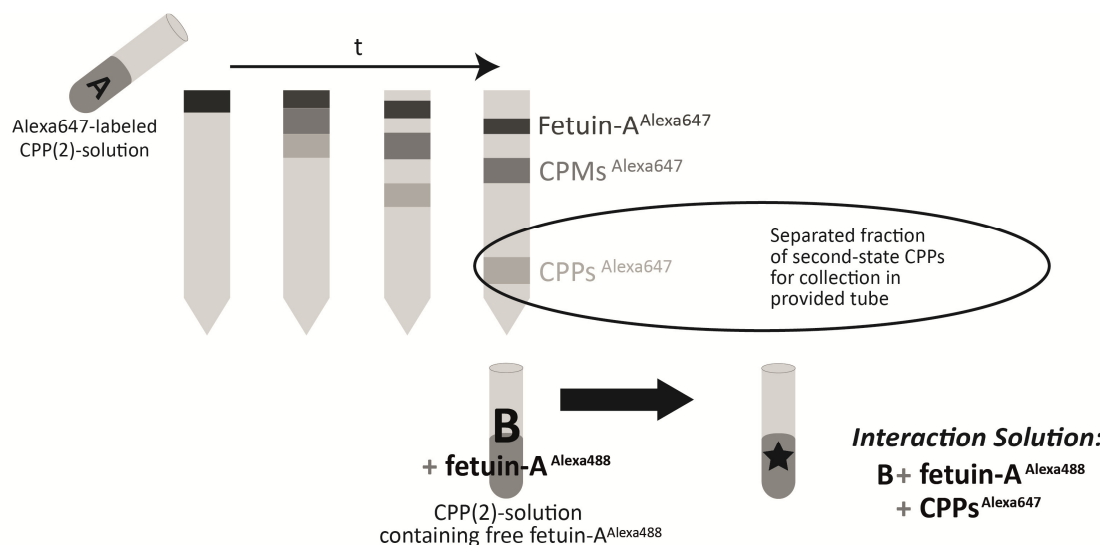


Figure 4.31: Separation of the fraction of second-state CPPs from the Alexa647-labeled CPP(2)-solution (A) using liquid chromatography. For further investigations, the separated second-state CPP fraction was collected in a vessel containing unlabeled, unfractionated CPP(2)-solution and additional Alexa488-labeled free fetuin-A (B).

The interaction-solution was investigated with FCS after 20 h exchange time. We tried one-color experiments as well as two-color experiments. These measurements revealed a broad distribution of diffusion coefficients rather than one distinct diffusion coefficient. This already hints at an exchange occurring in the solution.

The exchange is not only limited to the Alexa488-labeled fetuin-A, but labeled fetuin-A can also exchange with unlabeled fetuin-A bound to the CPPs present in the CPP(2)-solution. If this exchange occurs, fetuin-A can be expected to also exchange with the CPMs contained in the CPP(2)-solution. This leads to a variety of variously labeled particles in different sizes present in the final solution after the exchange time. Particles affected by fetuin-A exchange can be CPPs as well as CPMs. Thus, both particle types can carry Alexa488-label, Alexa647-label or both labels, respectively. The particular amount of bound labeled fetuin-A can vary from particle to particle. Additionally, Alexa488-labeled fetuin-A as well as Alexa647-labeled, free fetuin-A is present in the solution. The free Alexa647-labeled fetuin-A goes into solution after exchange with free fetuin-A. None of the concentrations is directly accessible which renders the determination of a distinct diffusion coefficient rather impossible.

In the present study we are interested in the CPP fraction. The exchange can be definitely proven if second-state CPPs carry both types of Alexa-label.

From our previous measurements we know that fractionated second-state CPPs are stable in a CPP(2)-solution. In consideration of this knowledge, we separated the second-state CPPs from the rest of the interaction-solution by gel filtration chromatography and collected the fractionated second-state CPPs in a freshly prepared, unlabeled CPP(2)-solution. We called this final mixture the investigation-solution (see Figure 4.32). If an exchange of free fetuin-A and CPP-bound fetuin-A occurred during the exchange time, the fractionated second-state CPPs now carry the Alexa647-label as well as the Alexa488-label.

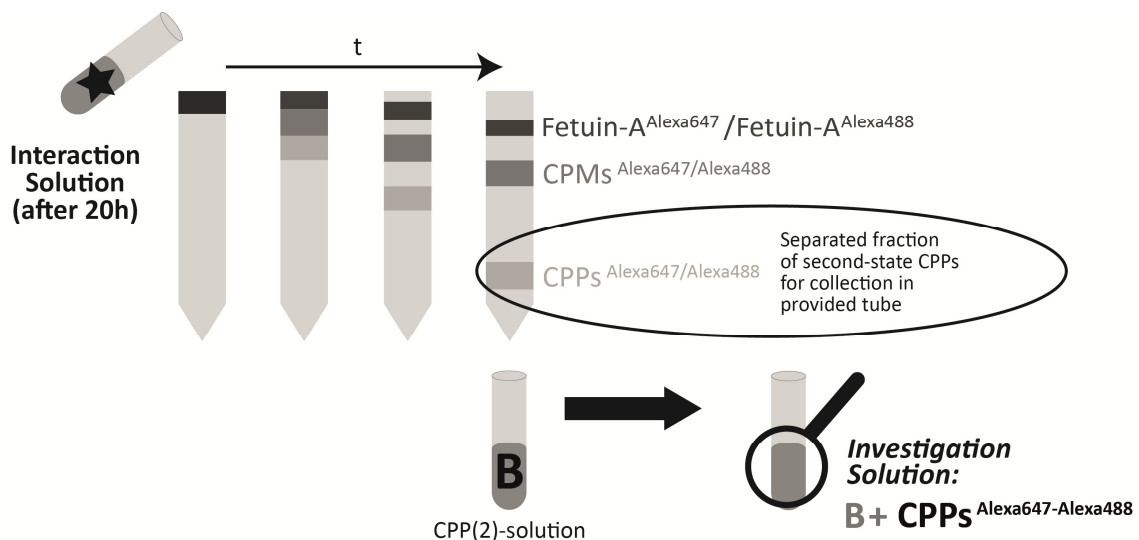


Figure 4.32: Separation of the fraction of second-state CPPs after 20 h interaction time from the CPP(2)-solution containing Alexa488- and Alexa647-label (Interaction-solution) using liquid chromatography. For further investigations, the separated second-state CPP fraction was collected in a vessel containing unlabeled, unfractionated CPP(2)-solution (B).

4.4.2.5 Exchange of Fetuin-A bound to the CPP-Surface with free Fetuin-A in Solution

Two-color FCS experiments were finally performed on the investigation-solution (compare Figure 4.32). The investigation-solution consisted of unlabeled CPP(2)-solution and the potentially doubly-labeled fractionated second-state CPPs.

In the case of the present contribution we expect the fractionated second-state CPPs to carry the Alexa647-label as well as the Alexa488-label. Thus, excitation with one of the two lasers should provide a correlation function in each case. The diffusion coefficient determined from the correlation functions of both excitation wavelengths should be the same as we expect to see only the labeled fractionated second-state CPPs. Furthermore, a cross-color correlation is possible for the case, that an exchange occurred and the fractionated second-state CPPs carry both labeled fetuin-A types.

An example for the correlation functions obtained at the particular excitation wavelengths is shown in Figure 4.33 together with the respective fits. The signal detected from both excitation wavelengths, respectively, can be autocorrelated for every single measurement. Fitting of the correlation functions provides the respective diffusion coefficient of the particles in solution.

For an excitation wavelength of $\lambda_1 = 637 \text{ nm}$, we obtained an average diffusion coefficient of $D_1 = (2.9 \pm 0.5) \mu\text{m}^2\text{s}^{-1}$ (corresponding hydrodynamic radius $R_{H,1} = (89.2 \pm 20.2) \text{ nm}$). Data evaluation for an excitation wavelength of $\lambda_2 = 470 \text{ nm}$ provided a diffusion coefficient of $D_2 = (2.7 \pm 0.5) \mu\text{m}^2\text{s}^{-1}$ (hydrodynamic radius $R_H = (95.0 \pm 18.4) \text{ nm}$).

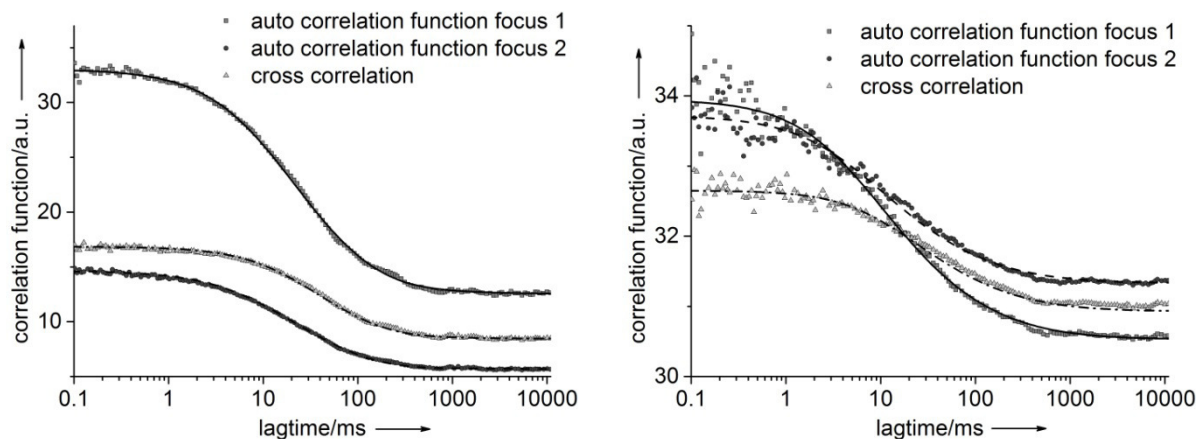


Figure 4.33: Two-focus correlation functions of labeled second-state CPPs in an unlabeled CPP(2)-solution for two-color-excitation (left: $\lambda_{\text{ex}} = 637 \text{ nm}$, right: $\lambda_{\text{ex}} = 470 \text{ nm}$); symbols: auto- and cross-correlation functions from FCS measurement, (dashed) lines: fitted functions. Fitting provides the diffusion coefficient of the labeled species.

In addition to the correlation functions for each color, we obtained a cross- correlation for both colors as shown in Figure 4.34. Hence, we concluded that Alexa488-labeled fetuin-A has bound to second-state CPPs during exchange time.

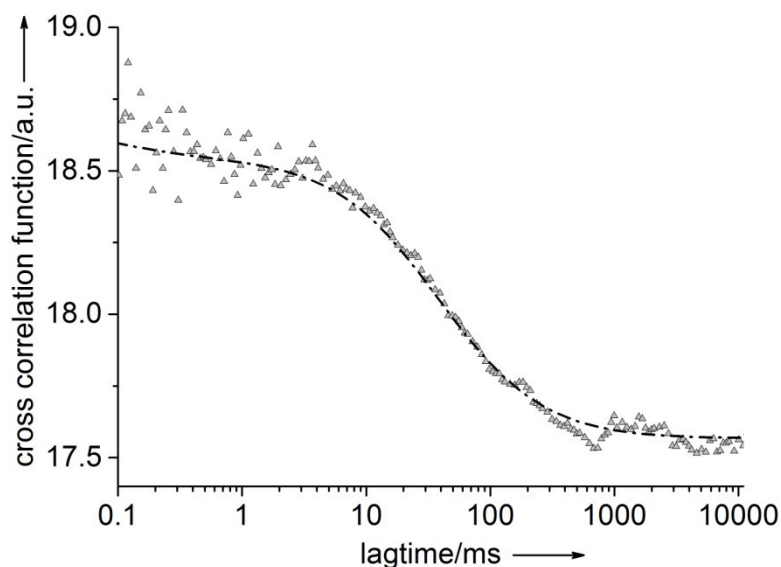


Figure 4.34: Two-color cross correlation function of fractionated second-state CPPs after exchange time. The fact that a cross correlation is possible reveals that an exchange of free fetuin-A with CPP-bound fetuin-A occurred.

3D-DLS measurements yield similar diffusion coefficients (see Supporting Information, Figure 6.4). Thus, the particle size before and after interaction time is the same. Fetuin-A does not form a multilayer at the CPP surface which would have resulted in an increasing CPP radius.

Hence, the two-color cross correlation function rather results from the exchange of CPP-bound fetuin-A with free fetuin-A. Alexa647-labeled fetuin-A bound to the second state CPPs' surface was obviously partly replaced by free Alexa488-labeled fetuin-A during exchange

time. Due to this exchange we obtained fractionated second-state CPPs carrying Alexa647-labeled fetuin-A and Alexa488-labeled fetuin-A at the same time (see also section 6.6.3).

The decay in the correlation function is weaker for the Alexa488-label than for the Alexa647-label also influencing the cross correlation. In the first step, CPPs consisted of mineral and Alexa647-labeled fetuin-A. Alexa647-labeled fetuin-A was partly replaced by Alexa488-labeled fetuin-A from the solution. The fetuin-A exchange is due to equilibration and thus time-dependent. Full equilibration was obviously not yet achieved so that the fractionated second state CPPs carry a bigger amount of Alexa647-labeled fetuin-A than Alexa488-labeled fetuin-A. Additionally, the exchange is not only limited to the labeled species. In fact, the unlabeled species contained in the stabilizing CPP(2)-solution also contribute to equilibration. Hence, differently labeled CPMs and free fetuin-A as already seen in the interaction-solution occur with proceeding time additional to the labeled CPPs. This was also seen in FCS, where diffusion coefficients became less distinct with increasing time (data not shown).

However, the occurrence of two-color cross correlation can only be explained by an exchange of fetuin-A bound to second state CPPs with free fetuin-A in solution. Hence, our experiments unambiguously prove this exchange for the first time.

4.4.3 Summary and Conclusion

We used a combined approach of two-color 2f-FCS and 3D-DLS to elucidate the fundamentals of mineral stabilization in the presence of fetuin-A. In this context, we especially investigated the exchange of free fetuin-A and fetuin-A bound to second-state CPPs. The stability of the fractionated second-state CPPs was tested in different environments in order to find the optimum conditions for the exchange experiments.

Stability of the fractionated second-state CPPs could only be maintained by providing a CPP(2)-solution. An extra addition of free fetuin-A to the CPP(2)-solution did not affect the diffusion coefficient.

Our investigations on the long-term stability revealed that the fractionated second state CPPs are stable for at least three days when collected in a CPP(2)-solution but not when collected in water or TBS (with and without fetuin-A).

The present study is the first one to unambiguously prove the exchange of free fetuin-A with fetuin-A bound to the surface of second-state CPPs. This behavior is based on the equilibrium of free and CPP-bound fetuin-A. However, the results also show the difficulty in effective separation and stabilization of the investigated second-state CPP fraction for the time of experiments.

The results of the present study need to be considered when performing future in vitro and in vivo studies on the fetuin-A-CPP-system. Particularly the findings concerning the occurring equilibria are of great importance as it has to be considered that different equilibration phenomena can occur during examination.

Several studies have proven the affinity of proteins to adsorb onto different surfaces (including mineral).¹⁶⁸⁻¹⁷³ A high surface activity is also assumed in case of fetuin-A as FCS measurements revealed its adsorption onto different materials in the context of the present

work (data not shown). Nevertheless, we could monitor the fetuin-A exchange within the scope of the CPP-fetuin-A-system. This shows the occurrence of fetuin-A desorption in equilibrium. Thus, we assume that our findings from the fetuin-A-CPP-system can be transferred to other protein-mineral systems. In those systems, equilibration phenomena will always have to be considered. When changes in the composition of an investigated system are performed, it is always necessary to check the different routes for equilibration in order to reliably interpret obtained data. Thus, the work presented here will greatly influence further research in the field of biomineralization. Additionally, research focusing on the directed formation of mineral particles in the presence of proteins or similarly behaving additives will have to be done under consideration of the described equilibration effects.

4.4.4 Experimental Section

4.4.4.1 Two-Focus Fluorescence Correlation Spectroscopy (2f-FCS)

We used two-color 2f-FCS to determine the diffusion coefficient of the second-state CPPs and to investigate the interaction of free and CPP-bound fetuin-A.^{53,174} A setup with two laterally shifted but overlapping foci with identical shape provides the basis for 2f-FCS-measurement. The shift perpendicular to the optical axis is generated by insertion of a Nomarski prism into the excitation light path of a fluorescence confocal microscope. Absolute values for the diffusion coefficient can then be calculated by measuring the autocorrelation function (ACF) for each detection volume and the cross correlation function between both volumes (CCF) with subsequent analysis of the CCF decay delay compared to the ACF decay. Thus, the exact distance between both detection volume centers has to be known. As explicitly described in the work of Dertinger and Pacheco⁵³ the diffusion-related part of the ACF and CCF is given by:

$$\tilde{g}(t, \delta, \nu) = \frac{c}{4} \sqrt{\frac{\pi}{Dt}} \int dz_1 \int dz_2 \frac{\kappa(z_1)\kappa(z_2)}{8Dt + \omega^2(z_1) + \omega^2(z_2)} \exp\left[-\frac{(z_2 - z_1)^2}{4Dt} - \frac{2\delta^2}{8Dt + \omega^2(z_1) + \omega^2(z_2)}\right] \quad (4.6)$$

In equation (4.6), t is the correlation lag-time, δ is the lateral distance between the foci, z_1 and z_2 are factors proportional to the overall excitation intensity and detection efficiency in each focus, c is the concentration of the fluorescent particles and D is their diffusion coefficient.

The functions $\omega(z)$ and $\kappa(z)$ are defined as follows:

$$\omega(z) = \omega_0 \left[1 + \left(\frac{\lambda_{ex} z}{\pi \omega_0^2 n} \right)^2 \right]^{\frac{1}{2}} \quad (4.7)$$

and

$$\kappa(z) = 2 \int_0^a \frac{d\rho\rho}{R^2(z)} \exp\left(-\frac{2\rho^2}{R^2(z)}\right) = 1 - \exp\left(-\frac{2a^2}{R^2(z)}\right) \quad (4.8)$$

with

$$R(z) = R_0 \left[1 + \left(\frac{\lambda_{em} z}{\pi R_0^2 n} \right)^2 \right]^{\frac{1}{2}} \quad (4.9)$$

where λ_{ex} and λ_{em} are excitation and emission wavelengths, n is the refractive index of the investigated sample, a is the radius of the confocal pinhole and ω_0 and R_0 are fit parameters.

By setting δ in equation (4.6) to zero and replacing $z_{1,2}$ by either z_1^2 or z_2^2 , respectively calculation of the ACF for each focus becomes possible. The integration step has to be carried out numerically. Fitting the experimental data is performed globally for both ACFs and the CCF. As fitting parameters $z_1 c^{1/2}$, $z_2 c^{1/2}$, ω_0 , R_0 and D are used. The lateral distance between the two foci δ is a constant for every setup. A detailed description of the technical setup is given in.^{53,175,176}

Every measurement runs for 10 or 15 minutes depending on the sample type. The colloidal particles discussed in this contribution have hydrodynamic radii below 200 nm. Specific particle size effects on the correlation function can thus be neglected.¹⁷⁷

FCS experiments were performed using two lasers with excitation wavelengths of $\lambda_1 = 637$ nm and $\lambda_2 = 470$ nm. Measurements were repeated minimum 50 times per sample and color to achieve better statistics. The resulting correlation functions were fitted. The diffusion coefficients obtained from fitting were averaged and the hydrodynamic radius of the particles was calculated.

4.4.4.2 Three dimensional cross correlation Dynamic Light Scattering (3D-DLS)

Standard CPP mineralization mixes become turbid with particle transformation from the first to the second-state. Sample turbidity prevents particle characterization by standard dynamic light scattering methods. Therefore we used a 3D cross correlation dynamic light scattering (3D-DLS) setup for the determination of the hydrodynamic radii. All measurements were performed using a standard light scattering device (LS instruments, Fribourg, Switzerland) with He-Ne-laser (JDS Uniphase, KOHERAS GmbH, 632.8 nm, 25 mW, Type LGTC 685-35), two avalanche photodiodes (Perkin Elmer, Type SPCM-AQR-13-FC) and an ALV 7002 correlator (ALV GmbH, Langen, Germany). The scattered light was detected at an angle of 90°. Temperature stability was ensured by an external thermostat equipped with a Pt-100 temperature sensor. Single measurements run for two minutes. Every diffusion coefficient was calculated from at least two measurements. Hydrodynamic radii were calculated using the Stokes-Einstein relation. This method provides the size of a sphere moving with the same characteristics as the scattering particle. In the present study, we investigated second-state CPPs. In this state, the particle size is stable over time. For simplicity, the ellipsoidal shape of the second-state CPPs was neglected as we determined only relative changes.

4.4.4.3 Sample Preparation

Fetuin-A Preparation

Lyophilized bovine fetuin-A (Sigma, F2379)¹⁷ was dissolved in Tris-buffered saline (TBS), centrifuged (4°C, 10000 g, 10 min) and applied onto a Superdex 200 Hi-load16/60 column (4°C; Amersham/GE Healthcare). The protein monomer fractions were collected and

concentrated using ultrafiltration (4°C; Centripreps, Millipore, molecular weight cut-off of 30 kDa). The fetuin-A concentration was assayed photometrically, assuming an extinction coefficient of $\epsilon^{1\%}(280\text{ nm})=4,5^{123}$. Aliquots of purified protein were frozen in liquid nitrogen and stored at -20°C until use. All solutions were prepared with ultrapure water (Lichrosolv®).

Fetuin-A Labeling

The fetuin-A was labeled using amine-reactive Alexa Fluor carboxylic acid, succinimidyl ester (Life Technologies GmbH, Alexa Fluor 488: A20000, Alexa Fluor 647: A20006). The labeling was performed following the standard labeling procedure for amine-reactive probes. After labeling, fetuin-A was separated from unreacted dye performing four rinsing steps with TBS on Zeba™ Desalt Spin Columns (Thermo Fisher Scientific Inc.).

The concentration of the labeled fetuin-A was again assayed photometrically.

Formation and Transformation of CPPs, Separation of second-state CPPs

A standard inhibition mix (see Figure 4.35) was used for the formation of CPPs. It contained fetuin-A (1 mg/ml, purified as described above), Tris (50 mM), NaCl (140 mM), Na₂HPO₄ (6 mM) and CaCl₂ (10 mM). For FCS measurements all used solution were prepared with ultrapure water. CaCl₂ was always added as last component; CaCl₂ addition starts the process of CPP formation. All stock solutions were filtered (0,45 μm pore size) before use. Reaction mixtures were prepared in 1 ml-volumes to ensure perfectly homogenous mixing of all components. If more than 1 ml of total volume was necessary, several 1 ml reaction mixtures were prepared. The mixtures were incubated for 1 h at 37°C to ensure CPP transformation into second-state. This procedure finally led to a solution containing second-state CPPs, CPMs, fetuin-A, buffer substances and mineral. We named this solution CPP(2)-solution (see Figure 4.35).

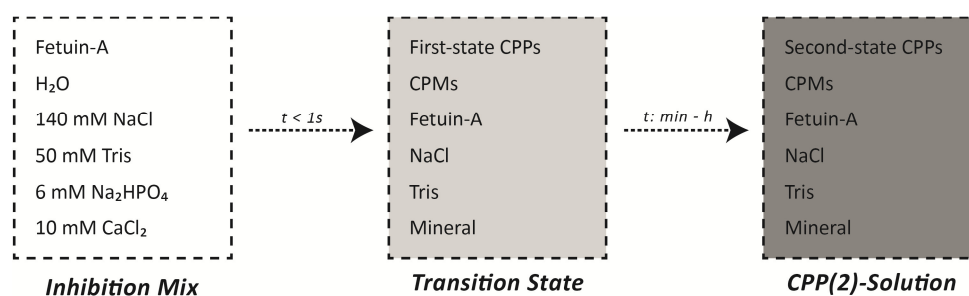


Figure 4.35: The inhibition mix was used for CPP formation. Upon addition of CaCl₂ as last component, CPPs form instantaneously (formation time < 1 s²⁶). Via this metastable transition state, first-state CPPs transform into second-state CPPs. The transformation time is temperature-dependent.¹⁴⁸ CPMs form simultaneously.²⁷ The CPP(2)-solution contains CPMs as well as second-state CPPs and the remaining fetuin-A, salts and mineral.

In addition to the CPP(2)-solution, we needed separated second-state CPPs. For that purpose, the CPP(2)-solution can be fractionated using size exclusion chromatography. The fractionated second-state CPPs were collected in an empty collecting tube or a collecting tube containing the designated solution after chromatography (see Figure 4.26).

If the second-state CPPs were used for FCS investigation, they were formed using Alexa647-labelled fetuin-A instead of unlabeled fetuin-A.

5 Conclusions

5.1 Summary

The mineral stabilization by fetuin-A represents a model system for biomineralization research. Research in this field combines the interests of scientists of several disciplines. While the composition of the CPPs belongs to the fields of biology and chemistry, their occurrence is especially important in the field of medicine. The investigation methods can range from typical chemical or biological methods up to physical methods as described in the present work. This shows that the addressed problems typically require an interdisciplinary approach. The interdisciplinarity is also reflected in the present work as all topics described in the previous chapters were addressed in different multidisciplinary collaborations including collaborations with biologists, physicists and medical scientists.

The main purpose of the present work was to obtain a more detailed knowledge on the processes underlying the calcium phosphate stabilization by fetuin-A. While one focus lay on structural investigations of the CPPs and the fetuin-A molecule itself, a second focus was set on investigations of the interaction of the CPPs and fetuin-A. Therefore, different approaches were used including in particular scattering experiments in the form of light-(DLS) and X-ray scattering (SAXS) and fluorescence correlation spectroscopy (FCS). DLS was primarily used to investigate the influence of different parameters (temperature, fetuin-A- and mineral concentration) on the CPP transformation time and the CPP radius in first and second state. Furthermore, DLS measurements served as reference measurements for the FCS study on the interaction behavior of fetuin-A and second-state CPPs. The dynamic exchange of free fetuin-A with fetuin-A bound to second-state CPPs was unambiguously proven with those measurements. In contrast, SAXS measurements revealed structural details of the monomeric fetuin-A in solution and uncovered details concerning the composition of a CPP-solution in the different states.

Chapter 4.1 dealt with the investigation of the influence of different parameters on CPP size and transformation time. We found that changes in the concentration of fetuin-A and mineral both affected CPP size and transformation time. While the transformation time increased with increasing fetuin-A concentration, it decreased with increasing mineral concentration. A higher protein to mineral ratio thus increases the transformation time and with that the time-dependent stability of the first-state CPPs. The hydrodynamic radii were slightly smaller for increased concentrations of fetuin-A and mineral. The difference in size was considerably small so that we assume that variations in the concentration of fetuin-A and mineral only caused minor structural changes in the CPPs.

Variations in the temperature significantly affected the transformation time as expected. In contrast, a significant size effect was only determinable for secondary CPPs under low supersaturation (LS) conditions. The temperature of the stock solutions before mixing did not affect the CPP size. Those findings indicate that the processes of CPP formation and transformation are two distinct, independent processes. It additionally suggests that the mechanisms themselves remain unaltered upon variations in the reaction parameters.

The data collected at different temperatures have been used for a kinetic analysis according to the Arrhenius law. It was found that the activation energy E_a for the transformation

tended to be lower under LS than under HS (high supersaturation) conditions. This can be attributed to the presence of less ordered CPPs in the case of HS conditions compared to LS conditions. In consequence, CPP transformation into the second state may be accompanied by more extensive structural rearrangements. This, in turn, leads to a higher activation energy under HS conditions.

Furthermore, the dynamic light scattering studies revealed no secondary effects like CPP aggregation or similar. Under all tested conditions, the process is reproducible and the particles are stable for some hours to days as expected from previous studies.⁵

Altogether, the performed light-scattering study provided elementary insights into the principles of calcium phosphate stabilization by fetuin-A. The findings were especially utilized for the subsequent SAXS measurements dealing with the structural changes during CPP transition (compare chapter 4.3) as they permitted to choose the right conditions (fetuin-A and mineral concentration, temperature) in order to obtain best possible time-resolution for the measurements. Furthermore, those findings are important for future research e.g. in order to optimize the stability of organic-mineral colloids in the framework of the design and synthesis of organic-inorganic hybrid materials similar to what has been shown in the work of Böker et al.⁹⁷. Additionally, knowledge of the underlying principles of protein-mineral interaction and colloid stabilization is necessary for clinical approaches, like diagnostics and therapies for calcification-sensitive patients. Due to the fact that the investigated system can be regarded as model system, we assume that the findings can also be transferred to similar protein-mineral systems. Furthermore, the findings are relevant for research and applications in the field of bionanotechnology.

Chapter 4.2 included the results obtained from fetuin-A solution measurements at the EMBL X33 BioSAXS beamline at DESY, Hamburg. Those measurements provided the first 3D low-resolution structure of the native monomeric fetuin-A in solution. Reliable structure information was received including the alignment of the fetuin-A substructures, the domains D1-D3, although the plurality of glycosylations present in the case of fetuin-A complicated data evaluation. In this context, the location of selected fetuin-A regions on the outside of the native molecule as suggested by earlier studies by Willi Jahnen-Dechent et al. was verified. The measurements additionally revealed that fetuin-A tends to form aggregates. Thus, careful purification was necessary. Furthermore, freezing of the fetuin-A solution should be avoided to avoid aggregation. SAXS measurements of fetuin-A in mineral presence revealed no changes in the characteristics of the SAXS curves indicating that the mineral uptake occurs without structural changes within the fetuin-A molecule.

The received model provides the required information to further elucidate details of mineral binding to the fetuin-A molecule. It will thus help to clarify the fundamentals of CPP formation. Furthermore, it can help throughout the elucidation of details concerning the binding of further molecule types such as lipids, lectin or proteinase.

SAXS was also used to obtain structural information on the CPPs in first and second state and during transformation as described in chapter 4.3. For that purpose, SAXS curves of the CPPs were recorded time-dependently. Time-resolution was chosen best possible by selection of the optimum parameters according to their influence on transformation time as evaluated using DLS in chapter 4.1. The received scattering data were fitted using the *Size Distribution*

Program developed and applied in the group of Prof. Klemradt on the one hand and the analysis software provided by the NIST based on the software IGOR Pro on the other hand.

None of the approaches provided reliable information on the occurring particle sizes and their distribution although data could be fitted in both cases. Hence, it is not possible to explicitly describe the time-dependent developing of particle sizes and polydispersities on the basis of the received scattering data. Available fitting routines are not yet sufficient for the elucidation of the fundamentals of transition due to the fact that the size distribution of the particles present in the CPP-solution and their respective polydispersity seems to play an important role. In the present case, SAXS was chosen for the investigations on the transition process instead of SANS measurements performed by Heiss et al. earlier.^{4,27} SANS offers the possibility of selectively investigating particle fractions in a solution containing different species when contrast variation experiments are performed. A disadvantage of this method is its worse time resolution compared to SAXS. Hence, SAXS was chosen in the present case to explicitly investigate the transition state. However, the high proportion of small structures as well as small particles and/or aggregates composed of protein and/or mineral obviously influences the characteristics of the form factor so dramatically, that the exact solution composition and the time-dependent developing of particle sizes and polydispersities, respectively, is not accessible on the basis of the received scattering data.

However, a continuous change of the scattering curves was observable. Hence, it can be concluded that the transition from first to second state is a continuous process rather than an abrupt change. However, it remains to be clarified, whether the occurrence of smaller structures is only due to the transformation process as it is additionally conceivable, that a distinct polydispersity of particles is present at all times.

It can be concluded that the proportion of occurring CPMs and possibly further small particles such as mineral-protein-aggregates with different sizes is non-negligible for the collection and especially the interpretation of SAXS data. It has to be clarified in which amount those smaller structures are present in the CPP-solution before a detailed data evaluation is possible. Furthermore, it has to be clarified in which amount their composition and proportion can vary as they obviously contribute considerably to the characteristics of the experimental scattering data. Additionally, it has to be checked whether the small structures received from fitting correspond exclusively to smaller particles or whether they can (also) result from internal CPP structure.

Data indicate a rather oblate shape than the prolate shape supposed from previous electron micrographs. The present study for the first time considers the q^{-2} decay of the scattering curve for low q -values indicating the presence of oblate ellipsoids, although the characteristics of the scattering curves are comparable to the characteristics of previous scattering measurements.

Due to the fact that the measurements under static conditions were not sufficient for an explicit description of the CPP sizes and morphologies in the different states, CPP samples were additionally measured under flow conditions. Those measurements showed time-dependent anisotropy changes in the scattering pattern of the CPP sample. It could be shown that the calculation of difference scattering patterns is very promising in order to obtain reliable data on the anisotropy development of the CPPs during transformation. Further data evaluation will be performed in the context of a PhD thesis in the group of Prof.

Klemradt at RWTH Aachen University. The elucidation of the morphology changes will be necessary to clarify the process of CPP transformation. Subsequently, this knowledge can be utilized in order to clarify the mechanism of mineral stabilization by fetuin-A.

Finally, chapter 4.4 showed the combined approach using FCS and DLS for the investigation of the stability of second-state CPPs. Two-color FCS unambiguously revealed the dynamic exchange of fetuin-A bound to second-state CPPs with free fetuin-A in solution although fetuin-A is assumed to exhibit high surface affinity.

For the measurements, fractionation and stabilization of the second-state CPPs was necessary. For that purpose, an elaborated procedure of purification, separation and stabilization steps was developed, in which gel filtration chromatography plays a central role. In this context, the stability of fractionated second-state CPPs was checked in different environments. It was found that their stability was only maintained by providing a CPP(2)-solution as environment. Adding additional free fetuin-A to that solution did not affect the diffusion coefficient. Concurrently, the long-term stability of that solution was checked revealing that the fractionated second-state CPPs are stable for at least three days when collected in a CPP(2)-solution but not when collected in water or TBS (with and without fetuin-A).

In this context it was also shown that the mechanism of mineral stabilization by fetuin-A is based on the formation of different equilibria in the system. One existing equilibrium is the equilibrium between free fetuin-A and fetuin-A bound to the CPPs. At the same time, an equilibrium exists between CPPs and CPMs. A third equilibrium, namely between free fetuin-A and fetuin-A bound to CPMs, is assumed on the basis of those findings. This implicates an additional exchange of free fetuin-A and CPM-bound fetuin-A. This exchange could not be shown so far as measurements of the fractionated CPMs were not possible due to CPM instability when separated from the rest of the CPP(2)-solution.

The equilibria and the related exchange of molecules have to be considered for the evaluation of *in vivo* studies using fluorescently labeled fetuin-A for CPP investigations. Especially in the case when CPPs need to be localized in the body by fluorescence measurements, it has to be unmistakably ensured, that fluorescence arises from CPPs and not from CPMs or free fetuin-A to avoid misinterpretations.

Moreover, equilibration phenomena and protein exchange is also conceivable for similar protein-mineral complexes. Hence, the relevance of our findings is not restricted to the CPPs. It can rather be assumed that the results can be transferred to related systems in the fields of biomineralization and protein-based directed colloid formation. If changes in the composition of such systems are performed, the different routes for equilibration always have to be checked in order to reliably interpret the obtained data. At the same time, the procedure of purification, separation and stabilization developed in the present work can be transferred to similar systems in order to achieve selective measurability of the desired fraction of particles.

5.2 Outlook

Two different approaches are necessary for the elucidation of the exact process of mineral stabilization by fetuin-A. On the one hand, the fetuin-A molecule has to be elucidated in more detail, while the second focus has to lie on the CPPs. Especially the process of transformation has to be clarified more explicitly.

In case of the fetuin-A molecule it is necessary to calculate the domain models of bovine fetuin-A in order to obtain a consistent data set of theoretical and experimental data of the same species. Especially domain D3, which is derived from homology modeling based on the cystatin structure by now, needs further refinement. At the same time, SAXS data analysis is under continuous development. Improvements in the interpretation of SAXS data from glycosylated proteins will help to further improve the fetuin-A model. With those preliminary works it will be possible to calculate a consistent 3D-model of the monomeric fetuin-A in solution. With this knowledge, further binding- and interaction studies will be feasible. Those studies are not restricted to fetuin-A-mineral interaction but can also include interactions with other molecules like lipids, lectin or proteinase. Hence, the fetuin-A model will be the basis for further research on the activity and impact of fetuin-A. In this context, SAXS experiments investigating the fetuin-A structure in mineral presence have to be redone using the better purified monomeric fetuin-A as described in section 4.2.2.2. Up to now, those experiments have been performed using the usually purified fetuin-A which tends to form aggregates. Therefore, the obtained results have to be verified.

In case of CPP research, the next step has to be the detailed evaluation of the SAXS data recorded at different times. A detailed understanding of the time-dependent structural changes will be inevitable to clarify the stabilization process in detail. As a start, it is necessary to illuminate the exact solution composition and to understand which types of particles are in principle present. A possible approach for that purpose can be a combination of gel filtration chromatography and fast SAXS measurement. Fast SAXS measurements at biological samples are possible at the new BioSAXS beamline P12 at the PETRA III storage ring at DESY, Hamburg, which is run by the Biological Small-Angle Scattering Group at the European Molecular Biology Laboratory (EMBL). A fractionation of the CPP-solution with direct subsequent SAXS measurement of the particular fractions can help to elucidate which particle types are present in the CPP-solution. However it has to be checked how the best concentrations for SAXS measurements can be achieved. Possibly, the CPP-solution has to be diluted directly before fractionation. Such preliminary works can be done e.g. at a laboratory SAXS machine even when it is not directly coupled to a gel filtration chromatography setup. However, measurements have to be performed as prompt as possible after fractionation as the fractions are not long-term stable when separated from the rest of the solution (compare chapter 4.4).

For test measurements, a CPP(2)-solution can be used as it is known that this solution is long-term stable for at least some days. After finding the right conditions, the experiments can be performed at the synchrotron.

The measurements can be extended to CPP-solutions in different states (first state and especially the transformation state at different times). A subsequent combination of the SAXS-data of the particular components present in the CPP-solution at different times will help to understand the exact time-dependent transformation process. This will finally lead to

a detailed understanding of the CPP transformation and simultaneously helps to explain the process of mineral stabilization by fetuin-A.

A simplified approach to start with can be to separate the second-state CPPs from the rest of the CPP-solution and record the scattering curves of the remaining solution. The obtained scattering data can be subtracted from the scattering curves of the entire CPP-solution in order to obtain the mere CPP scattering. If this can be done for different CPP states, a detailed time-dependent analysis of the morphological change of the CPPs from first to second state is possible.

At the same time, the measurement of the CPP-solution under flow conditions is an extremely promising approach. In particular the method of calculating difference scattering patterns reveals time-dependent anisotropy changes in the CPP-solution. From the development of anisotropy it is possible to track the morphological changes of the CPPs during transformation. Thus, a detailed evaluation of the existing scattering patterns will be an important step in order to understand the mechanism of mineral stabilization by fetuin-A. This data evaluation is performed in the context of a PhD thesis in the group of Prof. Klemradt (Mark Servos, PhD thesis, in progress).

FCS can be used for further investigations on the stability of the particles present in the CPP(2)-solution. The previously occurring intermediate states are not long-term stable, so that FCS measurements of those states are difficult. Possibly, an adequate procedure of purification, separation and stabilization similar to the one described in the present work can be found which makes FCS measurements feasible also in these states. A first step aiming in this direction could be the stabilization of the CPM fraction which was not successful so far. For that purpose, the CPM fraction can be collected in different solutions similar to the approach described in chapter 4.4. If a stabilization of the CPM fraction is successful, the exchange of free fetuin-A and CPM-bound fetuin-A, which was assumed here, can be confirmed.

Another interesting point, which has not been dealt with in the present work, is the kinetics of the different equilibria. The time scale of the fetuin-A exchange at the surface of the second-state CPPs can be uncovered by employing fluorescently labeled fetuin-A. Two different approaches are conceivable.

Fluorescently labeled second-state CPPs can be fractionated using gel filtration chromatography and stabilized in a CPP(2)-solution containing only unlabeled species. Due to equilibration, the amount of labeled free fetuin-A in solution will increase with time. Simultaneously, the amount of labeled CPMs will increase due to fetuin-A exchange not only with CPPs but also with CPMs. For determining the degree of labeled fetuin-A that has detached from the CPPs in a defined time, the solution can be centrifuged. CPPs need to be separated from the rest of the solution by choosing the correct centrifugation velocity. Subsequently, the fluorescence intensity can be determined in the supernatant and be used to calculate the amount of labeled fetuin-A detached from the CPPs. If this measurement is repeated for different times and different initial concentrations of fetuin-A and mineral, the kinetics of equilibration of fetuin-A exchange can be elucidated.

However, it has to be ensured that centrifugation has no influence on fetuin-A detachment when applying this procedure. For that purpose, the fluorescence intensity of the fractions separated from the CPP(2)-solution via gel filtration chromatography can be determined

separately and compared to the fluorescence intensity of pellet and supernatant after centrifugation. Furthermore it has to be ensured that the fluorescence intensity in the supernatant is caused by fetuin-A and not by free dye. This can be checked using FCS to determine the diffusion coefficient of the particles present in the supernatant. Thus, falsification by the measurement of free dye can be eliminated or at least be strongly reduced.

Apart from particle separation by centrifugation, the CPP(2)-solution containing labeled second-state CPPs can also be completely fractionated by gel filtration chromatography after different times. A direct subsequent determination of the fluorescence intensity in the obtained fractions will also contribute to the elucidation of the kinetics of fetuin-A exchange in the investigated system.

The measurement of free fetuin-A in solution using FCS was not yet successful (see section 6.6.1). For the determination of the fetuin-A diffusion coefficient measurements can be redone using anti-adsorption coatings for the measurement cells. Before that, the adsorption behavior of fetuin-A onto different (and differently coated) materials has to be investigated to find a surface with preferably little fetuin-A adsorption. For that purpose it is possible to try coatings such as poly(ethylene glycol) which have already shown to prevent protein adsorption in similar cases (compare section 6.6.1). Hence, this approach can also be tried for the measurement of fetuin-A.

With that procedure, the determination of a reference value for the fetuin-A diffusion coefficient can become possible. An even simpler approach could be to measure the labeled free fetuin-A in a CPP(2)-solution without further labeled species using FCS. From the development of the routine for CPP stabilization it is known that a fetuin-A addition to the CPP(2)-solution does not change the average diffusion coefficient of the solution. Thus it can be assumed that fetuin-A is stable in that environment. The diffusion coefficient of fetuin-A should then be determinable. However, FCS measurements have to be performed relatively direct after mixture of labeled fetuin-A and the CPP(2)-solution to avoid disturbance in the FCS signal by labeled particles occurring because of fetuin-A exchange due to equilibration.

Furthermore, FCS studies can be extended to investigations on the interaction of fetuin-A with different molecule species. On the one hand, the diffusion coefficient of a particle usually decreases upon binding of another particle which can be monitored in FCS. On the other hand, two-color experiments as performed in the present work are feasible. Such measurements can be performed to prove fetuin-A binding to selected molecules such as mineral, lipids, lectin or proteinase. Therefore, the species of interest and the fetuin-A molecule have to be labeled using dyes with different excitation/emission wavelengths. The occurrence of molecule binding can be proven if a cross-correlation signal is detectable (compare section 4.4.2.5). In particular, the fetuin-A mineral interaction can be elucidated in more detail. In combination with SAXS studies on the fetuin-A molecule in mineral environment as described before, this will help to clarify the exact process of mineral stabilization by fetuin-A.

6 Appendix

6.1 CPP Preparation

6.1.1 Fetuin-A Preparation

For CPP formation, purified fetuin-A is necessary. The purification was performed by Steffen Gräber in the group of Prof. Jahnen-Dechent at RWTH Aachen University.

For purification, lyophilized bovine fetuin-A¹⁷ (Sigma, F2379) was dissolved in TBS, centrifuged (4°C, 10000 g, 10 min.) and applied onto a Superdex 200 Hi-load16/60 column (4°C; Amersham/GE Healthcare). The protein monomer fractions were collected and concentrated using ultrafiltration (4°C; Centripreps, Millipore, molecular weight cut-off of 30 kDa). The fetuin-A concentration was assayed photometrically, assuming an extinction coefficient of $\epsilon^{1\%}(280\text{ nm})=4,5$.¹²³ Aliquots of purified protein were frozen in liquid nitrogen and stored at -20°C until use.

6.1.2 Formation and Transformation of CPPs

Usual CPP formation is performed on the basis of a so-called *inhibition mix*. It contains fetuin-A in the desired concentration (purified as described above), Tris (50 mM), NaCl (140 mM), Na₂HPO₄ and CaCl₂ (see Table 6.1). Concerning the mineral concentration it was distinguished between low supersaturation (LS, 3 mM PO₄³⁻, 5 mM CaCl₂) and high supersaturation (HS, 6 mM PO₄³⁻, 10 mM CaCl₂).

Table 6.1: Ingredients of the Inhibition Mix.

	Fetuin-A [μM]	NaCl [mM]	Tris [mM]	Na ₂ HPO ₄ [mM]	CaCl ₂ [mM]
HS (high supersaturation)	desired concentration, between 13.5 and 75	140	50	6	10
LS (low supersaturation)				3	5

All stock solutions were filtered (0.45 μm pore size) before use. The CaCl₂ was always added as last component; CaCl₂ addition starts the process of CPP formation so that first-state (primary) CPPs are immediately present. CPMs form simultaneously.²⁷ The first-state CPPs transform into second-state (secondary) CPPs time-dependently. This finally leads to a solution containing second-state CPPs, CPMs, fetuin-A, buffer substances and mineral. We named this solution CPP(2)-solution. The process is schematically shown in Figure 4.35.

6.2 Formation and Stability Kinetics of Calcium Phosphate–Fetuin-A colloidal Particles probed by time-resolved Dynamic Light Scattering - Supplemental

6.2.1 CPP Size Analysis

Mineral sedimentation easily occurs in solutions that are supersaturated with regard to calcium and phosphate ions. The serum protein fetuin-A is able to inhibit this process transiently. It has been shown previously that the inhibition is associated with the formation of fetuin-A – mineral colloids, denoted as calciprotein particles (CPP). After a lag period initial (primary) CPPs (CPP1) rapidly transform to larger secondary CPPs (CPP2). We termed this process “ripening” in analogy to Ostwald ripening.

The data of all time-resolved DLS measurements are compiled in Table 6.2 and Table 6.3. Figure 6.1 represents a graphical illustration of the CPP sizes.

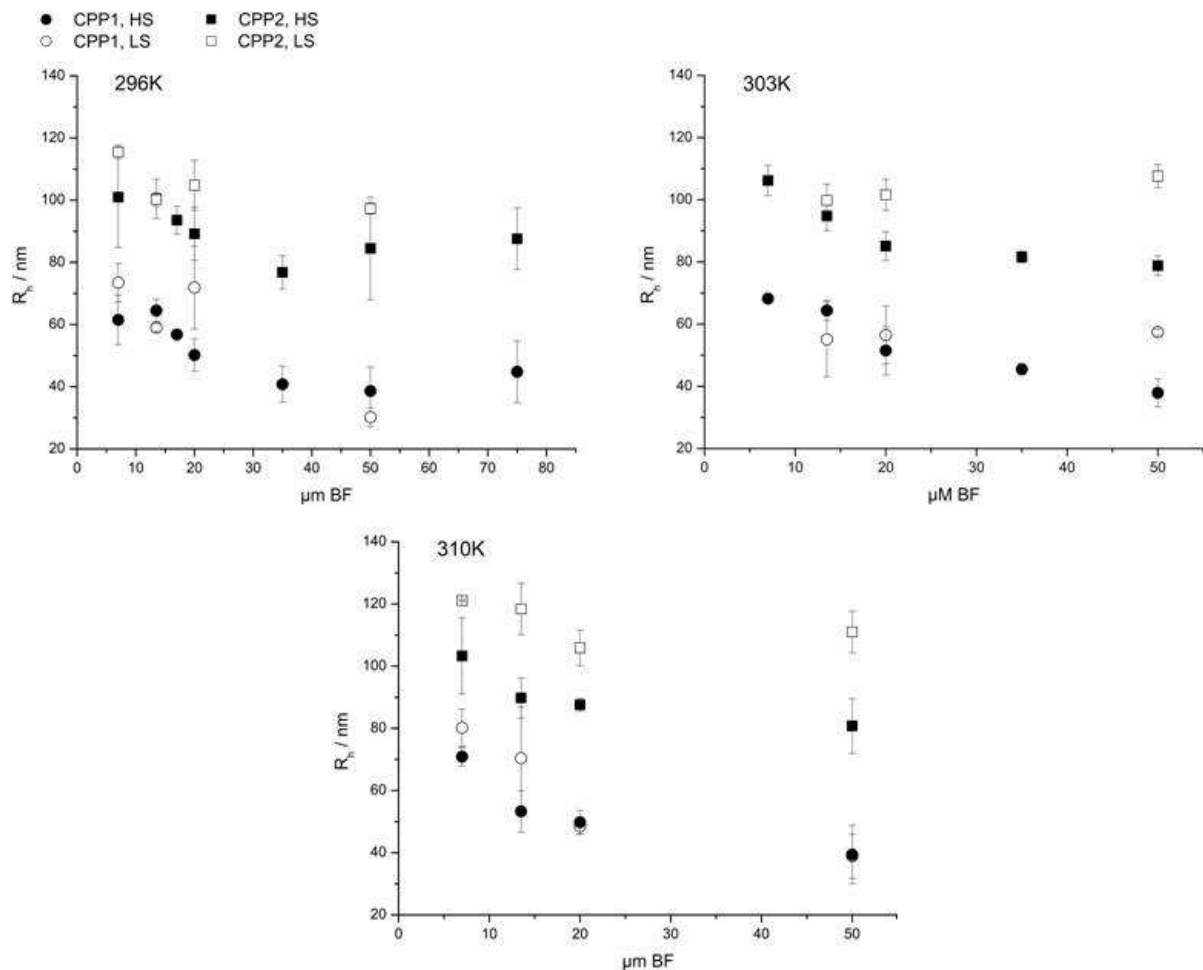


Figure 6.1: Bovine fetuin-A (BF) concentration-dependent plot of CPP sizes at three temperatures and two mineral ion concentrations. HS indicates high supersaturation conditions: 10 mM CaCl_2 and 6 mM Na_2HPO_4 , LS indicates low supersaturation conditions: 5 mM CaCl_2 and 3 mM Na_2HPO_4 . The hydrodynamic radii of primary CPPs (CPP1) range from 40 to 70 nm whereas the secondary CPPs (CPP2) range from 80 to 120 nm.

Under low and high mineral ion supersaturation (LS, HS; see methods) conditions, an increase in fetuin-A concentration led to smaller primary and secondary CPPs. Moreover, LS conditions produced slightly larger particles than high mineral ion supersaturation (HS)

conditions. Under LS conditions, the two-way analysis of variance (ANOVA) also revealed a statistically significant fetuin-A concentration – temperature interaction regarding CPP1 size. Regarding CPP2, the statistical analysis revealed in addition to the fetuin-A effect that higher temperatures resulted in larger particles. Under HS conditions, no temperature effect was found. Hence in this case, CPP ripening is apparently governed by mineral ion supersaturation outweighing the temperature effect.

6.2.2 DLS Data

Table 6.2: Comprehensive presentation of the hydrodynamic radii obtained from DLS measurements. For comparison, the radii in brackets were taken from ⁵. For each group, i.e. LS - HS conditions, CPP1 - CPP2, we performed a two-way analysis of variance (ANOVA using Graphpad Prism Software) of the hydrodynamic radius R_H with a significance level of $p < 0.05$. The effects of fetuin-A concentration, temperature and mineral ion supersaturation are compiled in Table 4.3.

	R_H (CPP1) [nm]			R_H (CPP2) [nm]		
LS						
T / K	296	303	310	296	303	310
7	73.5±6.2		80.2±6.0	115.5±2.2		121.1±0.2
13.5	59±1.2	55.1±12.3	70.4±16.5	102.6±1.7	99.8±5.3	118.4±8.2
20	68.8±12.5	56.5±9.3	48.5±2.6	103.1±7.3	101.6±5	105.9±5.7
50	30.2±3	50.2±12.3	38.9±7.1	97±1.8	108.7±3.3	111±6.6
HS						
T / K	296	303	310	296	303	310
BF / μM						
7	61.5±8 (63±6)	68.17±1.2	70.9±3	101±16.2 (103±13)	106.17±4.9	103.3±12.3
13.5	64.5±3.6	64.4±3.3	53.3±6.6	100.4±6.3	94.8±4.7	89.8±6.5
20	50.2±5.2 (44±6)	51.5±7.8	49.8±3.8	89.2±5.3 (80±5)	85.1±4.6	87.6±2.1
35	40.8±5.8	45.5±1.8	46.7±6.8	76.8±5.3	81.6±1.8	86.0±2.7
50	38.6±7.7 (38±9)	37.9±4.5	39.4±9.4	84.5±16.5 (72±8)	78.8±3.1	80.8±8.8

Table 6.3: Comprehensive presentation of the transition times obtained from DLS measurements. The effects of fetuin-A concentration, temperature and mineral ion supersaturation are compiled in Table 4.3.

	t_{trans} [min]					
	LS			HS		
T / K	296	303	310	296	303	310
7	717±151		75±6	332±23	118±15	44±12
13.5	778±130	471±67	138±39	455±5	180	55±11
20	720±67	420.±226	174±23	396±47	178±22	60±12
35				595±103	256±42	78±15
50	1111±51	463±33	200±42	475±34	202±3	73±2

6.3 Determination of Fetuin-A Shape and Structure - Supplemental

Ab initio modeling was performed on the basis of the experimental data by Clement Blanchet at EMBL, Hamburg. Experimental data and fit showed good agreement for all investigated fetuin-A concentrations. An exemplary result for 10.12 g/l fetuin-A is shown in Figure 6.2.

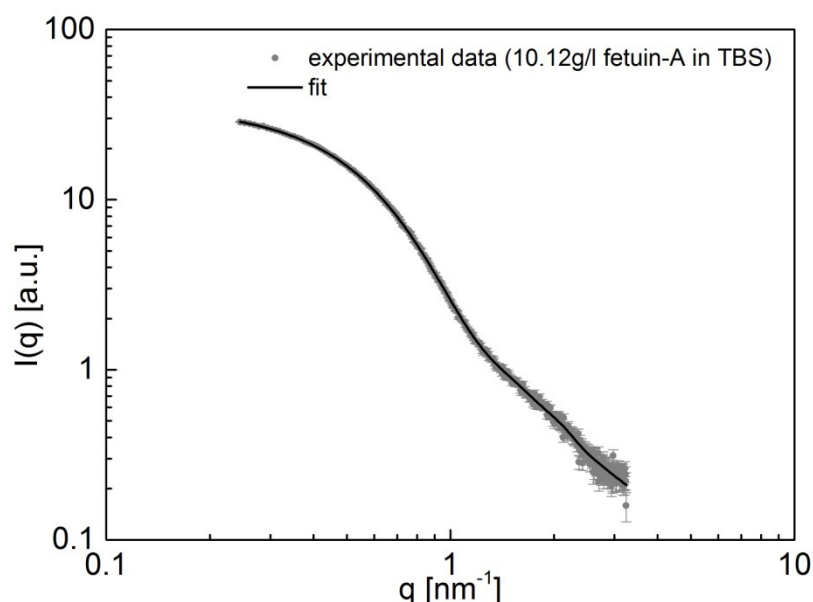


Figure 6.2: Exemplary experimental data of 10.12 g/l fetuin-A in TBS with respective fit. For ideal fit results, data points were omitted both at low and at high q -values. The volume computed from the curve corresponds to a molecular weight of 70-80 kDa, which is significantly higher than assumed for fetuin-A, although the fit matches the experimental data well.

Despite the good fit quality, the volume computed from the curves corresponds to molecular weights of around 70-80 kDa. This is significantly above the molecular weight of approximately 50 kDa determined for fetuin-A in earlier studies using ultracentrifugation and sedimentation studies.^{17,18}

6.4 Influence of X-Ray Exposure on Fetuin-A SAXS Curve

A fetuin-A sample was checked for radiation damage at HASYLAB beamline B1 of the DORIS III ring at Deutsches Elektronen-Synchrotron (DESY) in Hamburg. Therefore, scattering curves of 35 μM fetuin-A in TBS before and after beam exposure of 180 min were compared. The result is shown in Figure 6.3. The scattering pattern does not change with X-ray irradiation. Obviously, radiation damage does not occur or, more likely, occurs but is very weak. In the case of the CPP measurements, fetuin-A is, in case of doubt, rather protected by the mineral, so that radiation damages should be even weaker. Hence, we assumed that CPP measurements are possible without strong influence of radiation damages and that the transformation process is not strongly influenced. Therefore, CPP samples were measured as planned.

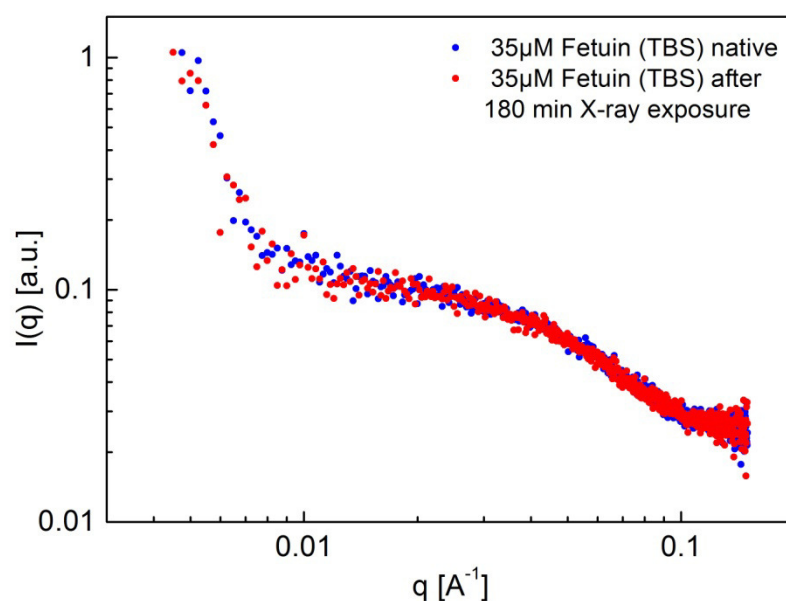


Figure 6.3: Scattering curves of 35 μM fetuin-A in TBS collected before and after X-ray exposure of 180 min. The characteristics of the SAXS curve do not change with X-ray irradiation.

6.5 Dynamic Exchange of Fetuin-A with colloidal Calciprotein Particles studied by means of two-color two-focus Fluorescence Correlation Spectroscopy - Supplemental

6.5.1 Additional Studies on the Stability of fractionated second-state CPPs

In case of the CPP(2)-solution we furthermore collected the pure separated second-state CPP fraction after liquid chromatography and mixed it with the CPP(2)-solution a certain time later. This time range varied from several minutes to hours.

Limited stability was achieved when mixing the second-state CPP fraction with the CPP(2)-solution a distinct time after CPP separation.

We obtained different results when we collected the pure labeled second-state CPPs from the liquid chromatography column and mixed them with the CPP(2)-solution in different ratios a certain time later. The longer the particles were stored without addition to the CPP(2)-solution, the more difficult it was to measure distinct diffusion coefficients with FCS.

These findings were independent of the ratio of both solutions. DLS-measurements showed a higher polydispersity for the particles mixed with the CPP(2)-solution a distinct time after separation.

The earlier this equilibrium-establishing system is mixed with the stabilizing CPP(2)-solution the less labeled CPPs have already disaggregated, so that we can still measure their diffusion coefficient rather accurately. Obviously, the state of equilibration established in the solution containing solely separated second-state CPPs is sustained after addition to the CPP(2)-solution. If equilibrium is fully established in the solution containing solely second-state CPPs, no distinct diffusion coefficient is measurable after mixing with the original CPP(2)-solution.

6.5.2 Stability of the Intermediate Solutions after the single Purification Steps investigated with 3D-DLS

3D-DLS was used to check the stability of the investigation-solution and constituting solute mixtures. The constituting solutions were pure CPP(2)-solution, the CPP(2)-solution containing additional free fetuin-A, the CPP(2)-solution containing additional free fetuin-A and the separated second-state CPPs as well as a diluted version of the last-mentioned.

All combinations of CPP(2)-solution, free fetuin-A and second-state CPPs show diffusion coefficients in the same range and stability for at least three days (results shown in Figure 6.4). The values for the diffusion coefficient in pure CPP(2)-solution and in the solution containing the separated second-state CPPs after interaction time (investigation-solution) are similar. Based on these findings it can be concluded that all performed changes within the in vitro-system are comparable among each other.

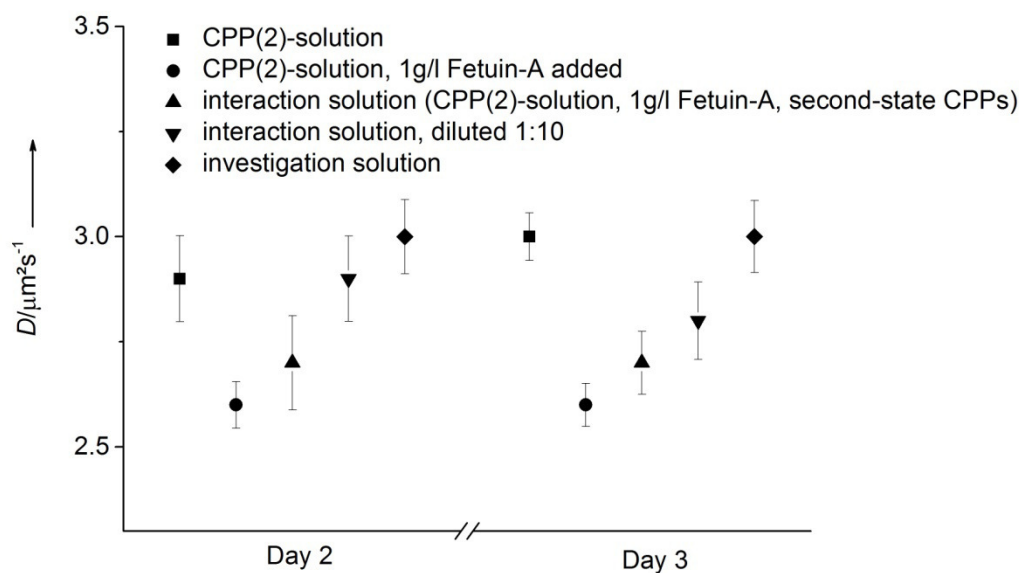


Figure 6.4: Diffusion coefficients of all intermediate solutions needed to receive the final investigation-solution and diffusion coefficient of the investigation-solution itself, determined with 3D-DLS at two consecutive days. The values are in the same range and show comparability of the used solutions.

6.6 Additional FCS Studies

6.6.1 FCS Measurements of pure Fetuin-A

Fetuin-A-labeling was achieved using amine-reactive Alexa Fluor 488 carboxylic acid, succinimidyl ester (Life Technologies GmbH, A20000) as described in section 4.4.4.3. The labeled fetuin-A was diluted in ultrapure TBS or ultrapure water, respectively, and two-focus FCS measurements were performed. However, the determination of the diffusion coefficient of pure, labeled fetuin-A was difficult. The larger part of FCS measurements did not result in correlation curves with evaluable decay. Some curves exhibited a decay but were very noisy. Usually, noise increased with increasing time. However, fitting of those curves was tried in order to obtain diffusion coefficients of the pure fetuin-A in solution. The correlation functions usually exhibited multiple-decay, so that the determination of a distinct diffusion coefficient was not possible. The obtained values rather ranged from $12 \mu\text{m}^2/\text{s}$ up to $700\text{--}800 \mu\text{m}^2/\text{s}$. The corresponding hydrodynamic radii thus varied from below 1 nm up to approximately 20 nm representing free dye as well as large aggregates. In some cases, the correlation functions exhibited a distinct decay and could be fitted using only one particle size as shown in Figure 6.5. However, the diffusion coefficients obtained in those cases resulted from free dye rather than from fetuin-A.

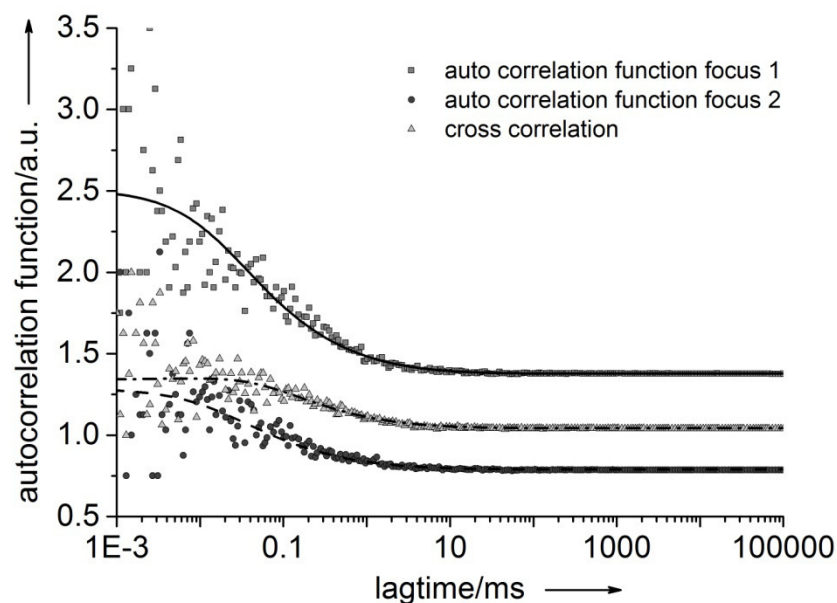


Figure 6.5: Two-focus correlation functions of Alexa488-labeled fetuin-A in ultrapure TBS. From data fitting a diffusion coefficient of $D = 377 \mu\text{m}^2/\text{s}$ was obtained corresponding to a hydrodynamic radius $R_H = 0.65 \text{ nm}$. This hydrodynamic radius can be assigned to free dye rather than to fetuin-A.

The increased noise with increasing time and the predominant measurability of the pure dye diffusion coefficient can have different reasons. On the one hand it is possible that the problems are caused by fetuin-A sticking to the surfaces of the sample cell. The surface adsorption reduces the ratio of labeled fetuin-A to free dye in solution leading to an increased probability of measuring free dye rather than labeled fetuin-A. Furthermore, fetuin-A adsorption to the sample cell can result in a dissociation of fetuin-A and free dye leading to an increased amount of free dye being present in the solution.

We tested our hypothesis by incubating the cover slides in a fetuin-A solution prior to the measurement. The measurements performed subsequently revealed diffusion coefficients in the range expected for fetuin-A. An exemplary correlation function is shown in Figure 6.6. However, the determined values varied strongly from measurement to measurement and the correlation functions became more noisy with time. This shows the strong influence of fetuin-A surface adsorption on the obtained results. While the surface of the cover slide was obviously saturated with fetuin-A, the stainless steel surface of the measurement cell was not. Thus, we assume that the adsorption of labeled fetuin-A to that surface gradually increased with time, which led to an increasing measurability of free dye rather than fetuin-A again. In the course of this process, correlation functions became more noisy.

Altogether it was not possible to obtain a distinct reference diffusion coefficient for pure fetuin-A in solution using FCS. However, we showed the high adsorption affinity of pure fetuin-A in ultrapure TBS or water. Due to our results we assume that fetuin-A sticks to the cover glass as well as to the stainless steel of the sample cell.

The high affinity of proteins to adsorb onto different surfaces is widely known so that this finding was not unexpected. The adsorption behavior and different possibilities for the prevention of protein adsorption - especially in the case of bovine serum albumin on stainless steel - have extensively been studied.¹⁷⁸⁻¹⁸⁰ It might be helpful to try different surfaces/different coatings to find a surface with preferably little fetuin-A adsorption for further measurements. Especially poly(ethylene glycol) coatings turned out to be very promising in the prevention of protein adsorption.^{181,182} Hence, this coating could also be tested for further investigations on fetuin-A.

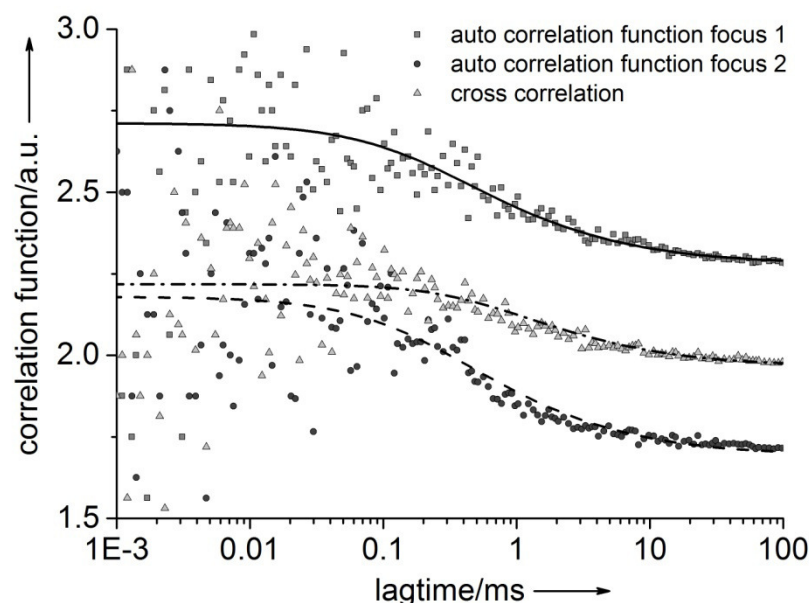


Figure 6.6: Two-focus correlation functions of Alexa488-labeled fetuin-A in ultrapure TBS. The used coverslide was incubated in an unlabeled fetuin-A solution prior to the measurement. From data fitting a diffusion coefficient of $D = 55 \mu\text{m}^2/\text{s}$ was obtained corresponding to an hydrodynamic radius $R_H = 4.4 \text{ nm}$.

6.6.2 Fractionated second-state CPPs are not stable in Water

The stability of fractionated second-state CPPs collected in ultrapure water in different concentrations was studied with FCS. Typical FCS data are shown in Figure 6.7. The

correlation functions showed a multiple-step decay indicating that the solution contains variously sized particles. We assume that this is because of equilibration phenomena occurring in the solution as the noise increases with time. Hence, we concluded that fractionated second-state CPPs are not stable in water.

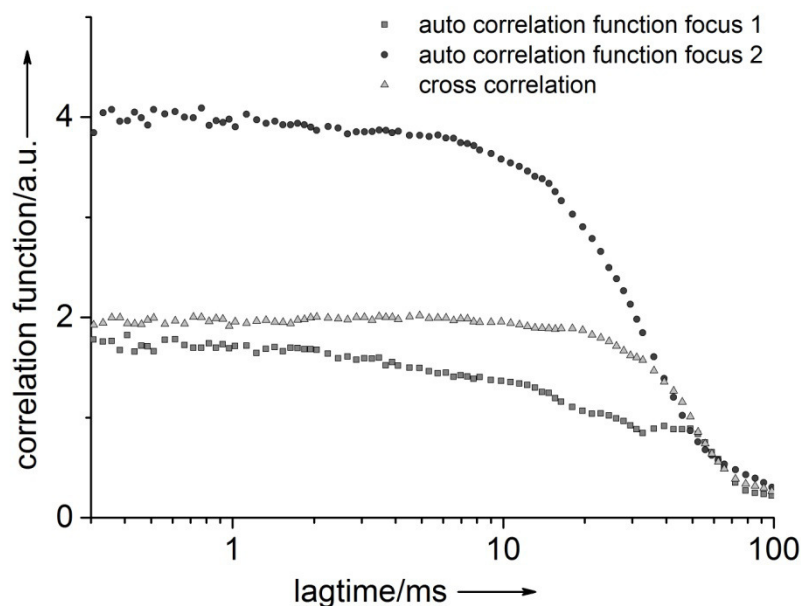


Figure 6.7: Two-focus correlation functions of labeled second-state CPPs in ultrapure water. The multiple-step decay hints at particles with various diffusion coefficients being present in the solution.

6.6.3 Two-color FCS Measurements of fractionated second-state CPPs

Fitting of the two-color cross correlation function (Figure 4.34) was only possible when choosing a dual triplet diffusion in the fit routine. One of the two obtained diffusion coefficients was always in the range expected for the second-state CPPs while the second diffusion coefficient was either very small or very high with values above $500 \mu\text{m}^2/\text{s}$. Obviously, in addition to the second-state CPPs, free dye and larger aggregates are always present. However, the signal of the fractionated second-state CPPs was predominant in all cases. Averaging the diffusion coefficients obtained for the second-state CPP fraction from the cross-color correlation fits results in $D = (2.4 \pm 0.4) \mu\text{m}^2/\text{s}$ (hydrodynamic radius $R_H = (103.1 \pm 17.9) \text{ nm}$) which corresponds to the values obtained from 3D-DLS (Figure 6.4).

6.7 Inoculation of Inhibition Mix with CPP(2)-Solution

The influence of the presence of second-state CPPs on CPP formation and transformation was investigated by means of 3D-DLS. Therefore a CPP(2)-solution was prepared as described in section 6.1.2. Afterwards, different volumes of CPP(2)-solution were added to the inhibition mix (see section 6.1.2). Normally, the inhibition mix is prepared by mixing water, Tris, NaCl, Na_2HPO_4 and CaCl_2 in the mentioned order to form CPPs. For the inoculation experiments, CPP(2)-solution was added to the inhibition mix either prior to or after the addition of CaCl_2 . The typical inhibition mix had a volume of $500 \mu\text{l}$. The amounts of added CPP(2)-solution varied from $2 \mu\text{l}$ up to $200 \mu\text{l}$. The time-dependent development of the hydrodynamic radii was followed using 3D-DLS.

Up to now, those experiments revealed no distinct trend for the impact of the addition of different amounts of CPP(2)-solution to the inhibition mix. However, it looks as if the addition of the CPP(2)-solution prior to CaCl_2 led to a direct transformation of the CPPs into second-state CPPs as 3D-DLS experiments revealed a direct increase in hydrodynamic radius (see Figure 6.8).

The determined hydrodynamic radii in second state were usually higher compared to the values determined for the second state without inoculation of the sample. However, CPPs were not in all cases stable but precipitates could be seen in different samples. Up to now, it was not possible to find a correlation between the ratio of CPP(2)-solution and inhibition mix and the transformation time or particle size. Different fetuin-A concentrations and different ratios of CPP(2)-solution and inhibition mix have been tested. Nevertheless, it is necessary to perform more experiments in order to get good statistics. Thus, it should be possible to uncover a general trend if a correlation between the different variables is existent.

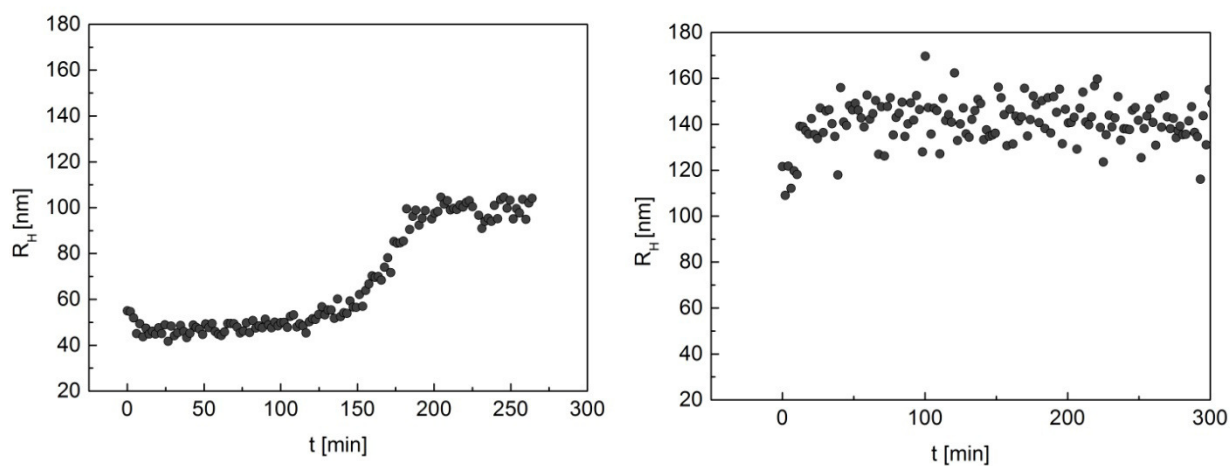


Figure 6.8: Left: Time-dependent evolution of CPP radius after preparation of inhibition mix (20 μM fetuin-A, LS (see section 6.1.2)). Right: Time-dependent evolution of CPP radius after inoculation of inhibition mix with 17 vol.-% CPP(2)-solution. Both measurements were performed at 37°C.

6.8 Evolution of pH-value during CPP Transformation

The pH-value was followed during CPP-transformation. This experiment revealed a decrease from an initial pH of approximately 7.4 down to a pH of 6.7 which occurs simultaneously to the increase in hydrodynamic radius. An exemplary result is shown in Figure 6.9.

A similar pH-effect has been shown in the context of calcium phosphate mineralization research in the presence of poly(ethylene imine) (LPEI).¹⁸³ We assume that the explanation given in that context can be transferred to the CPP system as described in the following.

It is known that CPP transformation is accompanied by a change in the mineral phase: while first-state CPPs consist of an amorphous protein-mineral phase, second-state CPPs exhibit an OCP core surrounded by a fetuin-A monolayer.⁴ According to Shkilnyy et al.¹⁸³, protons are released during phase transition. In the case of the CPPs, fetuin-A thus serves as proton acceptor. According to the explanation given for the particles formed in the presence of LPEI, CPP transformation is driven by the precipitation of OCP. This process leads to a proton release into solution. Thus, fetuin-A is protonated, which shifts the equilibrium towards the formation of OCP. For further understanding of the underlying process, studies with varying

fetuin-A and mineral content can be performed. Those studies will also need to include investigations on the time-dependent change in mineral phase as shown in the work of Shkilnyy et al.¹⁸³ Such investigations can help to further elucidate the principles underlying the directive process of CPP transformation in the future.

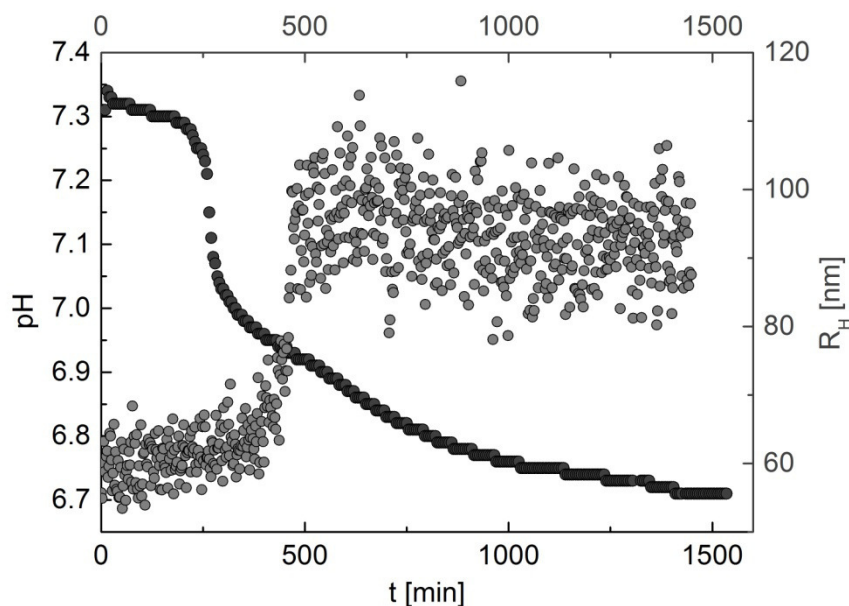


Figure 6.9: Time-dependent change in pH (black) and hydrodynamic radius (grey) of a CPP sample (13.5 μ M fetuin-A, HS). Measurements were performed at 23°C.

6.9 Development of a nanoparticle-based Test measuring overall Propensity for Calcification in Serum

In a collaborative research project, a test was developed by Andreas Pasch et al. which provides the possibility to measure the propensity for calcification in serum samples.¹⁶² It is applicable for hemodialysis patients as well as for healthy people and allows the identification of the individual risk for vascular calcifications and with that an increased risk for heart disease. This test found great attention as can be seen by the press release published by the American Society of Nephrology.¹⁸⁴

In principle, the test is based on a time-dependent measurement of the sample turbidity, which is applicable as solution turbidity increases with CPP transformation from first into second state. The phenomenon of particle formation and transformation known from the CPP fetuin-A system can also be observed in the presence of serum.

It is known that in vivo first-state CPPs occur in pathologic environments^{185–187} reflecting an imminent or active ongoing calcification¹⁶². In reverse, this means for the nephelometry measurements that a high CPP content and longer transition times correspond to a high residual capacity of the serum to form CPPs. This implies an intact humoral defense against calcification.¹⁶² According to that, the transition time can be used as a measure for the calcification propensity which is increased when decreased transition times are observed.

In the context of the present PhD thesis, 3D-DLS measurements were performed to investigate the delay in particle transformation of non-serum-containing reference samples as well as samples containing patient sera. Those measurements considerably contributed to

the explanation of the nephelometry measurements as they revealed distinct sizes of the particles present in the investigated solutions. Thus, it could be shown that the observed changes in the nephelometry signal are related to an increase in the hydrodynamic radius of the particles as known from the CPP fetuin-A system. Thus, it was possible to definitely show that the particles generating the signal in nephelometry are comparable with the known CPPs. The development as well as the test itself are described in more detail in the respective publication.¹⁶²

6.10 Abbreviations

°C	centigrade
ε	extinction coefficient
μl	microliter
μm	micrometer
μM	micromolar
2f-FCS	two-focus fluorescence correlation spectroscopy
3D-DLS	three dimensional cross correlation dynamic light scattering
Å	angstrom
AFM	atomic force microscopy
ANOVA	analysis of variance
BF	bovine fetuin-A
BSA	bovine serum albumin
cm	centimeter
CPM	calciprotein monomer
CPP	calciprotein particle
DESY	Deutsches Elektronen-Synchrotron
DLS	dynamic light scattering
e.g.	for example
EMBL	European Molecular Biology Laboratory
et al.	et alii (and others)
FCS	fluorescence correlation spectroscopy
g	gram
HASYLAB	Hamburger Synchrotronstrahlungslabor
HS	high supersaturation (6 mM PO ₄ ³⁻ , 10 mM CaCl ₂)
i.e.	it est (that is)
K	Kelvin
kDa	kilo Dalton
LPEI	poly(ethylene imine)
LS	low supersaturation (3 mM PO ₄ ³⁻ , 5 mM CaCl ₂)
MDF	molecule detection function
mg	milligram

min	minute
ml	milliliter
mM	millimolar
NIST	National Institute of Standards and Technology
nm	nanometer
NMR	nuclear magnetic resonance spectroscopy
OCP	octacalcium phosphate
PETRA	Positron Elektron Tandem Ring Anlage
PDDF	pair distance distribution function
PDI	polydispersity index
RDG theory	Rayleigh-Debye-Gans theory
s	second
SANS	small-angle neutron scattering
SAXS	small-angle X-Ray scattering
SLD	scattering length density
SLS	static light scattering
SPAD	single photon avalanche detector
TBS	Tris-buffered saline
TEM	transmission electron microscopy
ToF-SIMS	time of flight secondary ion mass spectrometry
Tris	Tris(hydroxymethyl)-aminomethan
USANS	ultra small angle neutron scattering

7 References

1. Pedersen, K. O.: Fetuin, a New Globulin Isolated from Serum. *Nature, Letters to the Editors* 154, 575 (1944).
2. Schäfer, C., Heiss, A., Schwarz, A., Westenfeld, R., Ketteler, M., Floege, J., Müller-Esterl, W., Schinke, T. & Jahnen-Dechent, W.: The serum protein α_2 – Heremans-Schmid glycoprotein / fetuin-A is a systemically acting inhibitor of ectopic calcification. *Journal of Clinical Investigation* 112, 357–366 (2003).
3. Heiss, A., DuChesne, A., Denecke, B., Grötzinger, J., Yamamoto, K., Renné, T. & Jahnen-Dechent, W.: Structural basis of calcification inhibition by alpha 2-HS glycoprotein/fetuin-A. Formation of colloidal calciprotein particles. *The Journal of Biological Chemistry* 278, 13333–13341 (2003).
4. Heiss, A., Jahnen-Dechent, W., Endo, H. & Schwahn, D.: Structural dynamics of a colloidal protein-mineral complex bestowing on calcium phosphate a high solubility in biological fluids. *Biointerphases* 2, 16–20 (2007).
5. Heiss, A., Eckert, T., Aretz, A., Richtering, W., van Dorp, W., Schäfer, C. & Jahnen-Dechent, W.: Hierarchical role of fetuin-A and acidic serum proteins in the formation and stabilization of calcium phosphate particles. *The Journal of Biological Chemistry* 283, 14815–14825 (2008).
6. Wiese, S. C.: Characterisation of Calciprotein Particles (CPPs). Diploma Thesis, RWTH Aachen University (2008).
7. Jahnen-Dechent, W., Heiss, A., Schäfer, C. & Ketteler, M.: Fetuin-a regulation of calcified matrix metabolism. *Circulation Research* 108, 1494–1509 (2011).
8. Lee, C., Bongcam-Rudloff, E., Sollner, C., Jahnen-Dechent, W. & Claesson-Welsh, L.: Type 3 cystatins; fetuins, kininogen and histidine-rich glycoprotein. *Frontiers in Bioscience* Volume, 2911 (2009).
9. Heremans, J. F. & Lambin, P.: *Les globulines sériques du système gamma: leur nature et leur pathologie*. (Editions Arscia: Paris, 1960).
10. Schmid, K. & Bürgi, W.: Preparation and properties of the human plasma Ba- α_2 -glycoproteins. *Biochimica et Biophysica Acta* 47, 440–453 (1961).
11. Terkelsen, O. B. F., Jahnen-Dechent, W., Nielsen, H., Moos, T., Fink, E., Nawratil, P., Müller-Esterl, W. & Møllgård, K.: Rat fetuin: distribution of protein and mRNA in embryonic and neonatal rat tissues. *Anatomy and Embryology* 197, 125–133 (1998).
12. Suzuki, M., Shimokawa, H., Takagi, Y. & Sasaki, S.: Calcium-binding properties of fetuin in fetal bovine serum. *Journal of Experimental Zoology* 270, 501–507 (1994).

13. Häusler, M., Schäfer, C., Osterwinter, C. & Jahnen-Dechent, W.: The physiologic development of fetuin-a serum concentrations in children. *Pediatric research* 66, 660–664 (2009).
14. Triffitt, J. T., Gebauer, U., Ashton, B. A., Owen, M. E. & Reynolds, J. J.: Origin of plasma α 2HS-glycoprotein and its accumulation in bone. *Nature* 262, 226–227 (1976).
15. Takagi, Y., Shimokawa, H., Suzuki, M., Nagai, H. & Sasoki, S.: Immunohistochemical localization of α 2HS glycoprotein in dentinHS glycoprotein in dentin. *Calcified Tissue International* 47, 40–45 (1990).
16. Schinke, T., Amendt, C., Trindl, A., Pöschke, O., Müller-Esterl, W. & Jahnen-Dechent, W.: The Serum Protein alpha2 -HS Glycoprotein / Fetuin Inhibits Apatite Formation in Vitro and in Mineralizing Calvaria Cells. *The Journal of Biological Chemistry* 271, 20789–20796 (1996).
17. Pedersen, K. O.: Ultracentrifugal and electrophoretic Studies on Fetuin. *Journal of Physical Chemistry* 51, 164–171 (1947).
18. Spiro, R. G.: Studies on Fetuin, a Glycoprotein of Fetal Serum: I. Isolation, chemical composition, and physicochemical properties. *The Journal of Biological Chemistry* 235, 2860–2869 (1960).
19. Spiro, R. G. & Bhoyroo, V. D.: Structure of the O-Glucosidically Linked Carbohydrates of Fetuin. *The Journal of Biological Chemistry* 249, 5704–5717 (1974).
20. Baenziger, J. U. & Fiete, D.: Structure of the complex oligosaccharides of fetuin. *The Journal of Biological Chemistry* 254, 789–795 (1979).
21. Jahnen-Dechent, W., Trindl, A., Godovac-Zimmermann, J. & Müller-Esterl, W.: Posttranslational Processing of Human α 2-HS Glycoprotein (Human Fetuin). *European Journal of Biochemistry* 226, 59–69 (2008).
22. Triffitt, J. T., Owen, M. E., Ashton, B. A. & Wilson, J. M.: Plasma disappearance of rabbit α 2 HS-glycoprotein and its uptake by bone tissue. *Calcified Tissue Research* 26, 155–161 (1978).
23. Young, J. D. & Martel, J.: The rise and fall of nanobacteria. *Scientific American Magazine* (2010).
24. Young, J. D., Martel, J., Young, L., Wu, C.-Y., Young, A. & Young, D.: Putative nanobacteria represent physiological remnants and culture by-products of normal calcium homeostasis. *PloS one* 4, e4417 (2009).
25. Young, J. D., Martel, J., Young, D., Young, A., Hung, C.-M., Young, L., Chao, Y.-J., Young, J. & Wu, C.-Y.: Characterization of granulations of calcium and apatite in serum as pleomorphic mineralo-protein complexes and as precursors of putative nanobacteria. *PloS one* 4, e5421 (2009).

26. Rochette, C. N., Rosenfeldt, S., Heiss, A., Narayanan, T., Ballauff, M. & Jahn-Dechent, W.: A shielding topology stabilizes the early stage protein-mineral complexes of fetuin-A and calcium phosphate: a time-resolved small-angle X-ray study. *ChemBioChem* 10, 735–740 (2009).
27. Heiss, A., Pipich, V., Jahn-Dechent, W. & Schwahn, D.: Fetuin-A is a mineral carrier protein: small angle neutron scattering provides new insight on Fetuin-A controlled calcification inhibition. *Biophysical Journal* 99, 3986–3995 (2010).
28. Posner, A. S. & Betts, F. Synthetic Amorphous Calcium Phosphate and Its Relation to Bone Mineral Structure. *Accounts of Chemical Research* 8, 273-281 (1975).
29. Onuma, K. & Ito, A. Cluster Growth Model for Hydroxyapatite. *Chemistry of Materials* 10, 3346–3351 (1998).
30. Herrmann, M.: Pathology of Ectopic Calcification in Fetuin-A Deficient Mice : Compensatory Gene Regulation and Mineralized Matrix Metabolism. PhD Thesis, RWTH Aachen University (2012).
31. Henson, P. M. & Hume, D. A.: Apoptotic cell removal in development and tissue homeostasis. *Trends in Immunology* 27, 244–250 (2006).
32. Pusey, P. N.: Introduction to Scattering Experiments. In: Lindner, P, Zemb, T.: *Neutrons, X-rays and Light: Scattering Methods Applied to Soft Condensed Matter*. Elsevier Science B.V., Amsterdam, 3–21 (2002).
- 32a. The figure was published in Lindner, P, Zemb, T.: *Neutrons, X-rays and Light: Scattering Methods Applied to Soft Condensed Matter* by Pusey, P. N.: Introduction to Scattering Experiments, 3-21, Copyright Elsevier Science B.V. (2002).
33. Pedersen, J. S.: Instrumentation for Small-Angle X-ray and Neutron Scattering and Instrumental Smearing Effects. . In: Lindner, P, Zemb, T.: *Neutrons, X-rays and Light: Scattering Methods Applied to Soft Condensed Matter*. Elsevier Science B.V., Amsterdam, 127–144 (2002).
34. Glatter, O.: Static Light Scattering of Large Systems. . In: Lindner, P, Zemb, T.: *Neutrons, X-rays and Light: Scattering Methods Applied to Soft Condensed Matter*. Elsevier Science B.V., Amsterdam, 171–201 (2002).
35. Eckert, T.: Untersuchungen zur Glasübergangsdynamik kolloidaler Systeme mit extrem kurzreichweitigen attraktiven Wechselwirkungen. PhD Thesis, Johannes Gutenberg-Universität Mainz (2004).
36. Pusey, P. N.: Dynamic Light Scattering. In: Lindner, P, Zemb, T.: *Neutrons, X-rays and Light: Scattering Methods Applied to Soft Condensed Matter*. Elsevier Science B.V., Amsterdam, 203–220 (2002).

37. Provencher, S. W.: A constrained regularization method for inverting data represented by linear algebraic of integral equations. *Computer Physics Communications* 27, 213–227 (1982).
38. Urban, C. & Schurtenberger, P.: Characterization of Turbid Colloidal Suspensions Using Light Scattering Techniques Combined with Cross-Correlation Methods. *Journal of Colloid and Interface Science* 207, 150–158 (1998).
39. Glatter, O., Hofer, M., Jorde, C. & Eigner, W.-D.: Interpretation of elastic light-scattering data in real space. *Journal of Colloid and Interface Science* 105, 577–586 (1985).
40. Glatter, O.: The Inverse Scattering Problem in Small-Angle Scattering. In: Lindner, P, Zemb, T.: *Neutrons, X-rays and Light: Scattering Methods Applied to Soft Condensed Matter*. Elsevier Science B.V., Amsterdam, 73–102 (2002).
- 40a. The original figure was published in Lindner, P, Zemb, T.: *Neutrons, X-rays and Light: Scattering Methods Applied to Soft Condensed Matter* by Glatter, O.: The Inverse Scattering Problem in Small-Angle Scattering, 73-102, Copyright Elsevier Science B.V. (2002).
41. Lakowicz, J. R.: *Principles of Fluorescence Spectroscopy*. 3rd Edition (Springer: New York, 2006).
42. Eggeling, C., Widengren, J., Rigler, R. & Seidel, C. A.: Photobleaching of Fluorescent Dyes under Conditions Used for Single-Molecule Detection: Evidence of Two-Step Photolysis. *Analytical Chemistry* 70, 2651–2659 (1998).
43. Eggeling, C., Volkmer, A. & Seidel, C. A. M.: Molecular photobleaching kinetics of Rhodamine 6G by one- and two-photon induced confocal fluorescence microscopy. *ChemPhysChem* 6, 791–804 (2005).
44. Nishimura, G. & Kinjo, M.: Systematic error in fluorescence correlation measurements identified by a simple saturation model of fluorescence. *Analytical Chemistry* 76, 1963–1970 (2004).
45. Schwille, P. & Haustein, E.: Fluorescence Correlation Spectroscopy - An Introduction to its Concepts and Applications at <http://www.biophysics.org/Portals/1/PDFs/Education/schwille.pdf>, accessed 19/06/2013, 13:34.
46. Enderlein, J., Gregor, I., Patra, D. & Fitter, J.: Art and Artefacts of Fluorescence Correlation Spectroscopy. *Current Pharmaceutical Biotechnology* 5, 155–161 (2004).
47. Nagy, A., Wu, J. & Berland, K. M.: Observation volumes and gamma-factors in two-photon fluorescence fluctuation spectroscopy. *Biophysical Journal* 89, 2077–2090 (2005).

48. Nagy, A., Wu, J. & Berland, K. M.: Characterizing observation volumes and the role of excitation saturation in one-photon fluorescence fluctuation spectroscopy. *Journal of Biomedical Optics* 10, 44015 (2005).
49. Schwille, P., Kummer, S., Heikal, A. A., Moerner, W. E. & Webb, W. W.: Fluorescence correlation spectroscopy reveals fast optical excitation-driven intramolecular dynamics of yellow fluorescent proteins. *Proceedings of the National Academy of Sciences* 97, 151–156 (2000).
50. Chattopadhyay, K., Saffarian, S., Elson, E. L. & Frieden, C.: Measuring unfolding of proteins in the presence of denaturant using fluorescence correlation spectroscopy. *Biophysical Journal* 88, 1413–1422 (2005).
51. Müller, C. B.: Applications of Two Focus Fluorescence Correlation Spectroscopy in Colloid and Polymer Science. PhD Thesis, RWTH Aachen University (2008).
52. Dertinger, T., Ewers, B., Krämer, B., Koberling, F., von der Hocht, Iris & Enderlein, J.: Dual-Focus Fluorescence Correlation Spectroscopy at http://www.picoquant.com/technotes/appnote_2ffcs.pdf, accessed 19/06/2013, 14:22.
53. Dertinger, T., Pacheco, V., von der Hocht, I., Hartmann, R., Gregor, I. & Enderlein, J.: Two-focus fluorescence correlation spectroscopy: a new tool for accurate and absolute diffusion measurements. *ChemPhysChem* 8, 433–443 (2007).
- 53a. Dertinger, T., Pacheco, V., von der Hocht, I., Hartmann, R., Gregor, I. & Enderlein, J.: Two-focus fluorescence correlation spectroscopy: a new tool for accurate and absolute diffusion measurements. *ChemPhysChem* 8, 433–443 (2007), © Wiley-VCH Verlag GmbH & Co. KGaA, Weinheim.
54. Eanes, E. D., Gillessen, I. H. & Posner, A. S.: Intermediate States in the Precipitation of Hydroxyapatite. *Nature* 208, 365–367 (1965).
55. Eanes, E. D. & Meyer, J. L.: The maturation of crystalline calcium phosphates in aqueous suspensions at physiologic pH. *Calcified Tissue Research* 23, 259–269 (1977).
56. Boskey, A. L. & Posner, A. S.: Conversion of Amorphous Calcium Phosphate to Microcrystalline Hydroxyapatite. A pH-Dependent, Solution-Mediated, Solid-Solid Conversion. *The Journal of Physical Chemistry* 77, 2313–2317 (1973).
57. Fan, Y., Sun, Z. & Moradian-Oldak, J.: Controlled remineralization of enamel in the presence of amelogenin and fluoride. *Biomaterials* 30, 478–483 (2009).
58. Sokolova, V., Knuschke, T., Kovtun, A., Buer, J., Epple, M. & Westendorf, A. M.: The use of calcium phosphate nanoparticles encapsulating Toll-like receptor ligands and the antigen hemagglutinin to induce dendritic cell maturation and T cell activation. *Biomaterials* 31, 5627–5633 (2010).

59. Welzel, T., Radtke, I., Meyer-Zaika, W., Heumann, R. & Epple, M.: Transfection of cells with custom-made calcium phosphate nanoparticles coated with DNA. *Journal of Materials Chemistry* 14, 2213 (2004).
60. Kester, M., Heakal, Y., Fox, T., Sharma, A., Robertson, G. P., Morgan, T. T., Altinoğlu, E. İ., Tabaković, A., Parette, M. R., Rouse, S. M., Ruiz-Velasco, V. & Adair, J. H.: Calcium Phosphate Nanocomposite Particles for In Vitro Imaging and Encapsulated Chemotherapeutic Drug Delivery to Cancer Cells. *Nano Letters* 8, 4116–4121 (2008).
61. Jutz, G. & Böker, A.: Bio-inorganic microcapsules from templating protein- and bionanoparticle-stabilized Pickering emulsions. *Journal of Materials Chemistry* 20, 4299 (2010).
62. Marchin, S., Putaux, J.-L., Pignon, F. & Léonil, J.: Effects of the environmental factors on the casein micelle structure studied by cryo transmission electron microscopy and small-angle x-ray scattering/ultrasmall-angle x-ray scattering. *The Journal of Chemical Physics* 126, 045101 (2007).
63. Margesin, R., Neuner, G. & Storey, K. B.: Cold-loving microbes, plants, and animals—fundamental and applied aspects. *Naturwissenschaften* 94, 77–99 (2006).
64. Blumenthal, N. C., Betts, F. & Posner, A. S.: Effect of carbonate and biological macromolecules on formation and properties of hydroxyapatite. *Calcified Tissue Research* 18, 81–90 (1975).
65. Sikirić, M. D. & Füredi-Milhofer, H.: The influence of surface active molecules on the crystallization of biominerals in solution. *Advances in Colloid and Interface Science* 128-130, 135–158 (2006).
66. Wang, L. & Nancollas, G. H.: Pathways to biomineralization and biodegradation of calcium phosphates: the thermodynamic and kinetic controls. *Dalton Transactions* 15, 2665–2672 (2009).doi:10.1039/b815887h
67. Holt, C., Sørensen, E. S. & Clegg, R. A.: Role of calcium phosphate nanoclusters in the control of calcification. *The FEBS Journal* 276, 2308–2323 (2009).
68. Ketteler, M., Bongartz, P., Westenfeld, R., Wildberger, J. E., Mahnken, A. H., Böhm, R., Metzger, T., Wanner, C., Jahnke-Dechent, W. & Floege, J.: Association of low fetuin-A (AHSG) concentrations in serum with cardiovascular mortality in patients on dialysis: a cross-sectional study. *The Lancet* 361, 827–833 (2003).
69. Hermans, M. M. H., Brandenburg, V., Ketteler, M., Kooman, J. P., van der Sande, F. M., Boeschoten, E. W., Leunissen, K. M. L., Krediet, R. T. & Dekker, F. W.: Association of serum fetuin-A levels with mortality in dialysis patients. *Kidney International* 72, 202–207 (2007).
70. Price, P. a & Lim, J. E.: The inhibition of calcium phosphate precipitation by fetuin is accompanied by the formation of a fetuin-mineral complex. *The Journal of Biological Chemistry* 278, 22144–22152 (2003).

71. Ostwald, W.: Studien über die Bildung und Umwandlung fester Körper. *Zeitschrift für Physikalische Chemie* 22, 289–330 (1897).
72. Price, P. A., Thomas, G. R., Pardini, A. W., Figueira, W. F., Caputo, J. M. & Williamson, M. K.: Discovery of a High Molecular Weight Complex of Calcium, Phosphate, Fetuin, and Matrix gamma -Carboxyglutamic Acid Protein in the Serum of Etidronate-treated Rats. *Journal of Biological Chemistry* 277, 3926–3934 (2001).
73. Matsui, I., Hamano, T., Mikami, S., Fujii, N., Takabatake, Y., Nagasawa, Y., Kawada, N., Ito, T., Rakugi, H., Imai, E. & Isaka, Y.: Fully phosphorylated fetuin-A forms a mineral complex in the serum of rats with adenine-induced renal failure. *Kidney International* 75, 915–928 (2009).
74. Termine, J. D. & Eanes, E. D.: Calcium phosphate deposition from balanced salt solutions. *Calcified Tissue Research* 15, 81–84 (1974).
75. Sandin, K., Kloo, L., Nevsten, P., Wallenberg, R. L. & Olsson, L.-F.: Formation of carbonated apatite particles from a supersaturated inorganic blood serum model. *Journal of Materials Science: Materials in Medicine* 20, 1677–1687 (2009).
76. He, G., Dahl, T., Veis, A. & George, A.: Nucleation of apatite crystals in vitro by self-assembled dentin matrix protein 1. *Nature Materials* 2, 552–558 (2003).
77. Beniash, E., Simmer, J. P. & Margolis, H. C.: The effect of recombinant mouse amelogenins on the formation and organization of hydroxyapatite crystals in vitro. *Journal of Structural Biology* 149, 182–190 (2005).
78. Gajjeraman, S., Narayanan, K., Hao, J., Qin, C. & George, A.: Matrix macromolecules in hard tissues control the nucleation and hierarchical assembly of hydroxyapatite. *The Journal of Biological Chemistry* 282, 1193–1204 (2007).
79. Tao, J., Pan, H., Zeng, Y., Xu, X. & Tang, R.: Roles of Amorphous Calcium Phosphate and Biological Additives in the Assembly of Hydroxyapatite Nanoparticles. *The Journal of Physical Chemistry B* 111, 13410–13418 (2007).
80. Tsuji, T., Onuma, K., Yamamoto, A., Iijima, M. & Shiba, K.: Direct transformation from amorphous to crystalline calcium phosphate facilitated by motif-programmed artificial proteins. *Proceedings of the National Academy of Sciences* 105, 16866–16870 (2008).
81. Bertoni, E., Bigi, A., Falini, G., Panzavolta, S. & Roveri, N.: Hydroxyapatite/polyacrylic acid nanocrystals. *Journal of Materials Chemistry* 9, 779–782 (1999).
82. Antonietti, M., Breulmann, M., Göltner, C. G., Cölfen, H., Wong, K. K. W., Walsh, D. & Mann, S.: Inorganic/Organic Mesostructures with Complex Architectures: Precipitation of Calcium Phosphate in the Presence of Double-Hydrophilic Block Copolymers. *Chemistry - A European Journal* 4, 2493–2500 (1998).

83. Urch, H., Vallet-Regi, M., Ruiz, L., Gonzalez-Calbet, J. M. & Epple, M.: Calcium phosphate nanoparticles with adjustable dispersability and crystallinity. *Journal of Materials Chemistry* 19, 2166 (2009).
84. Garnett, J. & Dieppe, P.: The effects of serum and human albumin on calcium hydroxyapatite crystal growth. *The Biochemical Journal* 266, 863–868 (1990).
85. Romberg, R. W., Werness, P. G., Riggs, B. L. & Mann, K. G.: Inhibition of hydroxyapatite crystal growth by bone-specific and other calcium-binding proteins. *Biochemistry* 25, 1176–1180 (1986).
86. Tomson, M. B. & Nancollas, G. H.: Mineralization Kinetics: A Constant Composition Approach. *Science* 200, 1059–1060 (1978).
87. Hunter, G. K., Hauschka, P. V., Poole, A. R., Rosenberg, L. C. & Goldberg, H. A.: Nucleation and inhibition of hydroxyapatite formation by mineralized tissue proteins. *The Biochemical Journal* 317, 59–64 (1996).
88. Hunter, G. K. & Goldberg, H. A.: Nucleation of Hydroxyapatite by Bone Sialoprotein. *Proceedings of the National Academy of Sciences* 90, 8562–8565 (1993).
89. Silverman, L. & Boskey, A. L.: Diffusion systems for evaluation of biomineralization. *Calcified Tissue International* 75, 494–501 (2004).
90. Spiro, R. G.: Demonstration of a Single Peptide Chain in the Glycoprotein Fetuin: Terminal Amino Acid Analyses and Studies of the Oxidized and Reduced Alkylated Preparations. *Journal of Biological Chemistry* 238, 644–649 (1963).
91. Neuman, W. & Neuman, M. W.: The Chemical Dynamics of Bone Mineral. *The American Journal of the Medical Sciences* 238, (1959).
92. Salimi, M. H., Heughebaert, J. C. & Nancollas, G. H.: Crystal growth of calcium phosphates in the presence of magnesium ions. *Langmuir* 1, 119–122 (1985).
93. Overbeck, E. & Sinn, C.: Three-dimensional dynamic light scattering. *Journal of Modern Optics* 46, 303–326 (1999).
94. Schätzel, K.: Suppression of Multiple Scattering by Photon Cross-correlation Techniques. *Journal of Modern Optics* 38, 1849–1865 (1991).
95. Liu, C., Huang, Y., Shen, W. & Cui, J.: Kinetics of hydroxyapatite precipitation at pH 10 to 11. *Biomaterials* 22, 301–306 (2001).
96. Wang, C., Lascu, I. & Giartosio, A.: Bovine serum fetuin is unfolded through a molten globule state. *Biochemistry* 37, 8457–8464 (1998).
97. Böker, A., He, J., Emrick, T. & Russell, T. P.: Self-assembly of nanoparticles at interfaces. *Soft Matter* 3, 1231–1248 (2007).

98. Ix, J. H., Shlipak, M. G., Brandenburg, V. M., Ali, S., Ketteler, M. & Whooley, M. A.: Association between human fetuin-A and the metabolic syndrome: data from the Heart and Soul Study. *Circulation* 113, 1760–1767 (2006).
99. Weikert, C., Stefan, N., Schulze, M. B., Pischon, T., Berger, K., Joost, H.-G., Haring, H.-U., Boeing, H. & Fritsche, A.: Plasma Fetuin-A Levels and the Risk of Myocardial Infarction and Ischemic Stroke. *Circulation* 118, 2555–2562 (2008).
100. Stefan, N., Fritsche, A., Weikert, C., Boeing, H., Joost, H.-G., Häring, H.-U. & Schulze, M. B.: Plasma fetuin-A levels and the risk of type 2 diabetes. *Diabetes* 57, 2762–2767 (2008).
101. Fisher, E., Stefan, N., Saar, K., Drohan, D., Schulze, M. B., Fritsche, A., Joost, H.-G., Häring, H.-U., Hubner, N., Boeing, H. & Weikert, C.: Association of AHSR gene polymorphisms with fetuin-A plasma levels and cardiovascular diseases in the EPIC-Potsdam study. *Circulation: Cardiovascular Genetics* 2, 607–613 (2009).
102. Dziegielewska, K. M. & Andersen, N. A.: The Fetal Glycoprotein, Fetuin, counteracts III-Effects of the Bacterial Endotoxin, Lipopolysaccharide, in Pregnancy. *Biology of the Neonate* 74, 372–375 (1998).
103. Ombrellino, M., Wang, H., Yang, H., Zhang, M., Vishnubhakat, J., Frazier, A., Scher, L. A., Friedman, S. G. & Tracey, K. J.: Fetuin, A Negative Acute Phase Protein, Attenuates Tnf Synthesis and the Innate Inflammatory Response to Carrageenan. *Shock* 15, 181–185 (2001).
104. Wang, H., Li, W., Zhu, S., Li, J., D'Amore, J., Ward, M. F., Yang, H., Wu, R., Jahnen-Dechent, W., Tracey, K. J., Wang, P. & Sama, A. E.: Peripheral administration of fetuin-A attenuates early cerebral ischemic injury in rats. *Journal of Cerebral Blood Flow & Metabolism* 30, 493–504 (2009).
105. Li, W., Zhu, S., Li, J., Huang, Y., Zhou, R., Fan, X., Yang, H., Gong, X., Eissa, N. T., Jahnen-Dechent, W., Wang, P., Tracey, K. J., Sama, A. E. & Wang, H.: A hepatic protein, fetuin-A, occupies a protective role in lethal systemic inflammation. *PLoS one* 6, e16945 (2011).
106. Chertov, O. Y., Ermolaeva, M. V., Satpaev, D. K., Saschenko, L. P., Kabanova, O. D., Lukanidin, E. M., Lukjanova, T. I., Redchenko, I. V., Blishchenko, L. Yu. & Gnuchev, N. V.: Inhibitory effect of calf fetuin on the cytotoxic activity of LAK cell-derived factors and tumor necrosis factor. *Immunology Letters* 42, 97–100 (1994).
107. Terkeltaub, R. A., Santoro, D. A., Mandel, G. & Mandel, N.: Serum and plasma inhibit neutrophil stimulation by hydroxyapatite crystals. evidence that serum α 2-HS glycoprotein is a potent and specific crystal-bound inhibitor. *Arthritis & Rheumatism* 31, 1081–1089 (1988).

108. Green, E. D., Adelt, G., Baenziger, J. U., Wilson, S. & Van Halbeek, H.: The Asparagine-linked Oligosaccharides on Bovine Fetuin. *The Journal of Biological Chemistry* 263, 18253–18268 (1988).
109. Carr, S. A., Huddleston, M. J. & Bean, M. F.: Selective identification and differentiation of N- and O-linked oligosaccharides in glycoproteins by liquid chromatography-mass spectrometry. *Protein Science* 2, 183–196 (1993).
110. Hägglund, P., Bunkenborg, J., Elortza, F., Jensen, O. N. & Roepstorff, P.: A New Strategy for Identification of N-Glycosylated Proteins and Unambiguous Assignment of Their Glycosylation Sites Using HILIC Enrichment and Partial Deglycosylation. *Journal of Proteome Research* 3, 556–566 (2004).
111. Heiss, W.-A.: Zur molekularen Topologie der Bindung natürlicher und rekombinanter Varianten von α_2 -HS-Glycoprotein/ Fetuin an Hydroxylapatit. PhD Thesis, RWTH Aachen University (2002).
112. Svergun, D. I.: Restoring low resolution structure of biological macromolecules from solution scattering using simulated annealing. *Biophysical Journal* 76, 2879–2886 (1999).
113. Svergun, D. I., Petoukhov, M. V & Koch, M. H. J.: Determination of Domain Structure of Proteins from X-Ray Solution Scattering. *Biophysical Journal* 80, 2946–2953 (2001).
114. Petoukhov, M. V., Konarev, P. V., Kikhney, A. G. & Svergun, D. I.: ATSAS 2.1 – towards automated and web-supported small-angle scattering data analysis. *Journal of Applied Crystallography* 40, 223–228 (2007).
115. Franke, D. & Svergun, D. I.: DAMMIF , a program for rapid ab-initio shape determination in small-angle scattering. *Journal of Applied Crystallography* 42, 342–346 (2009).
116. Mertens, H. D. T. & Svergun, D.: I. Structural characterization of proteins and complexes using small-angle X-ray solution scattering. *Journal of Structural Biology* 172, 128–141 (2010).
117. Bernocco, S., Steiglitz, B. M., Svergun, D. I., Petoukhov, M. V., Ruggiero, F., Ricard-Blum, S., Ebel, C., Geourjon, C., Deleage, G., Font, B., Eichenberger, D., Greenspan, D. S. & Hulmes, D. J. S.: Low resolution structure determination shows procollagen C-proteinase enhancer to be an elongated multidomain glycoprotein. *The Journal of Biological Chemistry* 278, 7199–7205 (2003).
118. Gherardi, E., Sandin, S., Petoukhov, M. V., Finch, J., Youles, M. E., Ofverstedt, L.-G., Miguel, R. N., Blundell, T. L., Vande Woude, G. F., Skoglund, U. & Svergun, D. I.: Structural basis of hepatocyte growth factor/scatter factor and MET signalling. *Proceedings of the National Academy of Sciences of the United States of America* 103, 4046–4051 (2006).

119. Sokolova, A. V., Kreplak, L., Wedig, T., Mücke, N., Svergun, D. I., Herrmann, H., Aebi, U. & Strelkov, S. V.: Monitoring intermediate filament assembly by small-angle x-ray scattering reveals the molecular architecture of assembly intermediates. *Proceedings of the National Academy of Sciences of the United States of America* 103, 16206–16211 (2006).
120. Høiberg-Nielsen, R., Tofteng Shelton, A. P., Sørensen, K. K., Roessle, M., Svergun, D. I., Thulstrup, P. W., Jensen, K. J. & Arleth, L.: 3- Instead of 4-helix formation in a de novo designed protein in solution revealed by small-angle X-ray scattering. *ChemBioChem* 9, 2663–2672 (2008).
121. Prischi, F., Konarev, P. V., Iannuzzi, C., Pastore, C., Adinolfi, S., Martin, S. R., Svergun, D. I. & Pastore, A.: Structural bases for the interaction of frataxin with the central components of iron-sulphur cluster assembly. *Nature Communications* 1, 95 (2010).
122. Petoukhov, M. V & Svergun, D. I.: Global rigid body modeling of macromolecular complexes against small-angle scattering data. *Biophysical Journal* 89, 1237–1250 (2005).
123. Murray, A. C., Oikawa, K. & Kay, C. M.: Circular dichroism studies on native fetuin and some of its derivatives. *Biochimica et Biophysica Acta (BBA) - Protein Structure* 175, 331–338 (1969).
124. Mylonas, E. & Svergun, D. I.: Accuracy of molecular mass determination of proteins in solution by small-angle X-ray scattering. *Journal of Applied Crystallography* 40, 245–249 (2007).
125. Konarev, P. V., Volkov, V. V., Sokolova, A. V., Koch, M. H. J. & Svergun, D. I.: PRIMUS : a Windows PC-based system for small-angle scattering data analysis. *Journal of Applied Crystallography* 36, 1277–1282 (2003).
126. Svergun, D. I.: Determination of the regularization parameter in indirect-transform methods using perceptual criteria. *Journal of Applied Crystallography* 25, 495–503 (1992).
127. Volkov, V. V. & Svergun, D. I.: Uniqueness of ab initio shape determination in small-angle scattering. *Journal of Applied Crystallography* 36, 860–864 (2003).
128. Alpha-2-HS-glycoprotein - Bos taurus (Bovine) at <http://www.uniprot.org/uniprot/P12763>, accessed 25/06/2013, 14:05.
129. Alpha-2-HS-glycoprotein - Mus musculus (Mouse) at <http://www.uniprot.org/uniprot/P29699>, accessed 25/06/2013, 14:06.
130. Alpha-2-HS-glycoprotein - Homo sapiens (Human) at <http://www.uniprot.org/uniprot/P02765>, accessed 25/06/2013, 14:11.

131. Pisano, A., Jardine, D. R., Packer, N. H., Redmond, J. W., Williams, K. L., Gooley, A. A., Farnsworth, V., Carson, W. & Cartier, P.: Identifying sites of glycosylation in proteins. *Techniques in Glycobiology* 299–320 (1996).
132. Yet, M. G., Chin, C. C. & Wold, F. The covalent structure of individual N-linked glycopeptides from ovomucoid and asialofetuin. *Journal of Biological Chemistry* 263, 111–117 (1988).
133. Bernhard, O. K., Kapp, E. A. & Simpson, R. J.: Enhanced analysis of the mouse plasma proteome using cysteine-containing tryptic glycopeptides. *Journal of Proteome Research* 6, 987–95 (2007).
134. Ghesquière, B., Van Damme, J., Martens, L., Vandekerckhove, J. & Gevaert, K.: Proteome-wide characterization of N-glycosylation events by diagonal chromatography. *Journal of Proteome Research* 5, 2438–2447 (2006).
135. Halim, A., Nilsson, J., Rüetschi, U., Hesse, C. & Larson, G.: Human urinary glycoproteomics; attachment site specific analysis of N- and O-linked glycosylations by CID and ECD. *Molecular & Cellular Proteomics* 11, M111.013649 (2012).
136. Kumbla, L., Cayatte, A. & Subbiah, M.: Association of a lipoprotein-like particle with bovine fetuin. *FASEB Journal* 3, 2075–2080 (1989).
137. Cayatte, A., Kumbla, L. & Subbiah, M.: Marked acceleration of exogenous fatty acid incorporation into cellular triglycerides by fetuin. *The Journal of Biological Chemistry* 265, 5883–5888 (1990).
138. Kumbla, L., Bhadra, S. & Subbiah, M.: Multifunctional role for fetuin (fetal protein) in lipid transport. *FASEB Journal* 5, 2971–2975 (1991).
139. Cawley, D. B., Simpson, D. L. & Herschman, H. R.: Asialoglycoprotein Receptor Mediates the Toxic Effects of an Asialofetuin-Diphtheria Toxin Fragment A Conjugate on Cultured Rat Hepatocytes. *Proceedings of the National Academy of Sciences* 78, 3383–3387 (1981).
140. Chong, P. & Klein, M.: Single-step purification of pertussis toxin and its subunits by heat-treated fetuin-Sepharose affinity chromatography. *Biochemistry and Cell Biology* 67, 387–391 (1989).
141. Skelton, S. K. & Wong, K. H.: Simple, efficient purification of filamentous hemagglutinin and pertussis toxin from *Bordetella pertussis* by hydrophobic and affinity interaction. *Journal of Clinical Microbiology* 28, 1062–1065 (1990).
142. Grossbard, M. L., Lambert, J. M., Goldmacher, V. S., Blattler, W. A. & Nadler, L. M.: Correlation between in Vivo Toxicity and Preclinical in Vitro Parameters for the Immunotoxin Anti-B4-blocked Ricin. *Cancer Research* 52, 4200–4207 (1992).

143. Tajirian, T., Dennis, J. W. & Swallow, C. J.: Regulation of human monocyte proMMP-9 production by fetuin, an endogenous TGF- β antagonist. *Journal of Cellular Physiology* 185, 174–183 (2000).
144. Leite-Browning, M. L., McCawley, L. J., Choi, O. H., Matrisian, L. M. & Ochieng, J.: Interactions of α 2-HS-glycoprotein (fetuin) with MMP-3 and murine squamous cell carcinoma cells. *International Journal of Oncology* 21, 965–971 (2002).
145. Leite-Browning, M. L., McCawley, L. J., Jahnen-Dechent, W., King, L. E., Matrisian, L. M. & Ochieng, J.: Alpha 2-HS glycoprotein (fetuin-A) modulates murine skin tumorigenesis. *International Journal of Oncology* 25, 319–324 (2004).
146. Mellgren, R. L. & Huang, X.: Fetuin A stabilizes m-calpain and facilitates plasma membrane repair. *The Journal of Biological Chemistry* 282, 35868–35877 (2007).
147. Hedrich, J., Lottaz, D., Meyer, K., Yiallourous, I., Jahnen-Dechent, W., Stöcker, W., Becker-Pauly, C.: Fetuin-A and cystatin C are endogenous inhibitors of human meprin metalloproteases. *Biochemistry* 49, 8599–8607 (2010).
148. Wald, J., Wiese, S., Eckert, T., Jahnen-Dechent, W., Richtering, W. & Heiss, A.: Formation and stability kinetics of calcium phosphate–fetuin-A colloidal particles probed by time-resolved dynamic light scattering. *Soft Matter* 7, 2869 (2011).
149. De Castro, O.: Untersuchung der Struktur und des Umwandlungsmechanismus von kolloidalen Calciprotein-Partikeln mittels Röntgen-Kleinwinkelstreuung. Master Thesis, RWTH Aachen University (2012).
150. Spurk, J. & Aksel, N.: *Strömungslehre: Einführung in die Theorie der Strömungen*. 8. Auflage (Springer: Heidelberg, 2010).
151. Günther, A.: Hydrodynamische Eigenschaften von magnetischen Nickelnanostäben in kolloidaler Suspension. PhD Thesis, Universität des Saarlandes, Saarbrücken (2011).
152. Bernstein, O. & Shapiro, M.: Direct determination of the orientation distribution function of cylindrical particles immersed in laminar and turbulent shear flows. *Journal of Aerosol Science* 25, 113–136 (1994).
153. Dubin, S. B., Clark, N. A. & Benedek, G. B.: Measurement of the Rotational Diffusion Coefficient of Lysozyme by Depolarized Light Scattering: Configuration of Lysozyme in Solution. *The Journal of Chemical Physics* 54, 5158 (1971).
154. King, T. A., Knox, A. & McAdam, J. D. G.: Translational and Rotational Diffusion of Tobacco Mosaic Virus from Polarized and Depolarized Light Scattering. *Biopolymers* 12, 1917–1926 (1973).
155. Bauer, D. R., Vrauman, J. I. & Pecora, R.: Depolarized light scattering from liquids. *Annual Review of Physical Chemistry* 27, 443–463 (1976).

156. Meyer, S.: Bestimmung der Größenverteilungsfunktionen von Teilchen mit sphärischen Geometrien mittels Röntgenkleinwinkelstreuung. Diploma Thesis, RWTH Aachen University (2010).
157. Servos, M.: Bestimmung der Größenverteilung von Partikeln unterschiedlicher Geometrien aus Röntgen-Kleinwinkelstreuendaten. Diploma Thesis, RWTH Aachen University (2011).
158. Kline, S. R.: Reduction and analysis of SANS and USANS data using IGOR Pro. *Journal of Applied Crystallography* 39, 895–900 (2006).
159. Merritt, M. & Zhang, Y.: Interior-Point Gradient Method for Large-Scale Totally Nonnegative Least Squares Problems. *Journal of Optimization Theory and Applications* 126, 191–202 (2005).
160. SLD Calculator at <sld-calculator.appspot.com>, accessed 13/06/2013, 10:57.
161. Price, P. a, Nguyen, T. M. T. & Williamson, M. K.: Biochemical characterization of the serum fetuin-mineral complex. *The Journal of Biological Chemistry* 278, 22153–22160 (2003).
162. Pasch, A., Farese, S., Gräber, S., Wald, J., Richtering, W., Floege, J. & Jahnen-Dechent, W.: Nanoparticle-based test measures overall propensity for calcification in serum. *Journal of the American Society of Nephrology* 23, 1744–1752 (2012).
163. Pedraza, C. E., Chien, Y.-C. & McKee, M. D.: Calcium oxalate crystals in fetal bovine serum: implications for cell culture, phagocytosis and biomineralization studies in vitro. *Journal of Cellular Biochemistry* 103, 1379–1393 (2008).
164. Weiner, S.: Biomineralization: a structural perspective. *Journal of structural biology* 163, 229–234 (2008).
165. Schulz, A., Wang, H., Van Rijn, P. & Böker, A.: Synthetic inorganic materials by mimicking biomineralization processes using native and non-native protein functions. *Journal of Materials Chemistry* 21, 18903 (2011).
166. Nudelman, F., Lausch, A. J., Sommerdijk, N. A. J. M. & Sone, E. D.: In vitro models of collagen biomineralization. *Journal of Structural Biology*, DOI: 10.1016/j.jsb.2013.04.003 (2013).
167. Schwille, P., Meyer-Almes, F. J. & Rigler, R.: Dual-color fluorescence cross-correlation spectroscopy for multicomponent diffusional analysis in solution. *Biophysical Journal* 72, 1878–1886 (1997).
168. Lhoest, J. B., Detrait, E., Van den Bosch de Aguilar, P. & Bertrand, P.: Fibronectin adsorption, conformation, and orientation on polystyrene substrates studied by radiolabeling, XPS, and ToF SIMS. *Journal of Biomedical Materials Research* 41, 95–103 (1998).

169. Giacomelli, C., Esplandiú, M., Ortiz, P., Avena, M. & De Pauli C. P.: Ellipsometric Study of Bovine Serum Albumin Adsorbed onto Ti/TiO(2) Electrodes. *Journal of Colloid and Interface Science* 218, 404–411 (1999).
170. Van Oss, C. J., Docoslis, A. & Giese, R. F.: Free energies of protein adsorption onto mineral particles — from the initial encounter to the onset of hysteresis. *Colloids and Surfaces B: Biointerfaces* 22, 285–300 (2001).
171. Combes, C. & Rey, C.: Adsorption of proteins and calcium phosphate materials bioactivity. *Biomaterials* 23, 2817–2823 (2002).
172. Höök, F., Vörös, J., Rodahl, M., Kurrat, R., Böni, P., Ramsden, J. J., Textor, M., Spencer, N. D., Tengvall, P., Gold, J. & Kasemo, B.: A comparative study of protein adsorption on titanium oxide surfaces using in situ ellipsometry, optical waveguide lightmode spectroscopy, and quartz crystal microbalance/dissipation. *Colloids and Surfaces B: Biointerfaces* 24, 155–170 (2002).
173. Müller, C., Wald, J., Hoth-Hannig, W., Umanskaya, N., Scholz, D., Hannig, M. & Ziegler, C.: Protein adhesion on dental surfaces—a combined surface analytical approach. *Analytical and Bioanalytical Chemistry* 400, 679–689 (2011).
174. Müller, C. B., Weiss, K., Loman, A., Enderlein, J. & Richtering, W.: Remote temperature measurements in femto-liter volumes using dual-focus-Fluorescence Correlation Spectroscopy. *Lab on a Chip* 9, 1248–1253 (2009).
175. Müller, C. B. & Richtering, W.: Sealed and temperature-controlled sample cell for inverted and confocal microscopes and fluorescence correlation spectroscopy. *Colloid and Polymer Science* 286, 1215–1222 (2008).
176. Müller, C. B., Loman, A., Pacheco, V., Koberling, F., Willbold, D., Richtering, W. & Enderlein, J.: Precise measurement of diffusion by multi-color dual-focus fluorescence correlation spectroscopy. *Europhysics Letters* 83, 46001 (2008).
177. Müller, C. B., Loman, A., Richtering, W. & Enderlein, J.: Dual-focus fluorescence correlation spectroscopy of colloidal solutions: influence of particle size. *The Journal of Physical Chemistry B* 112, 8236–8240 (2008).
178. Van Enkevort, H. J., Dass, D. V. & Langdon, A. G.: The adsorption of bovine serum albumin at the stainless-steel/aqueous solution interface. *Journal of Colloid and Interface Science* 98, 138–143 (1984).
179. Fukuzaki, S., Urano, H. & Nagata, K.: Adsorption of protein onto stainless-steel surfaces. *Journal of Fermentation and Bioengineering* 80, 6–11 (1995).
180. Omanovic, S. & Roscoe, S. G.: Electrochemical Studies of the Adsorption Behavior of Bovine Serum Albumin on Stainless Steel. *Langmuir* 15, 8315–8321 (1999).

181. Zhang, F., Kang, E., Neoh, K., Wang, P. & Tan, K.: Surface modification of stainless steel by grafting of poly(ethylene glycol) for reduction in protein adsorption. *Biomaterials* 22, 1541–1548 (2001).
182. Wei, J., Ravn, D. B., Gram, L. & Kingshott, P.: Stainless steel modified with poly(ethylene glycol) can prevent protein adsorption but not bacterial adhesion. *Colloids and Surfaces B: Biointerfaces* 32, 275–291 (2003).
183. Shkilnyy, A., Schöne, S., Rumpelach, C., Uhlmann, A., Hedderich, A., Günter, C., Taubert, A.: Calcium phosphate mineralization with linear poly(ethylene imine): a time-resolved study. *Colloid and Polymer Science* 289, 881–888 (2011).
184. American Society of Nephrology, Press Release: New Blood Test Detects Potentially Deadly Calcium Deposits. (2012) at <<http://newswise.com/articles/new-blood-test-detects-potentially-deadly-calcium-deposits>>, accessed 19/07/2013 13:37.
185. Fraikin, J.-L., Teesalu, T., McKenney, C. M., Ruoslahti, E. & Cleland, A. N.: A high-throughput label-free nanoparticle analyser. *Nature Nanotechnology* 6, 308–313 (2011).
186. Smith, E. R., Ford, M. L., Tomlinson, L. A., Rajkumar, C., McMahon, L. P. & Holt, S. G.: Phosphorylated fetuin-A-containing calciprotein particles are associated with aortic stiffness and a procalcific milieu in patients with pre-dialysis CKD. *Nephrology Dialysis Transplantation* 27, 1957–1966 (2012).
187. Hamano, T., Matsui, I., Mikami, S., Tomida, K., Fujii, N., Imai, E., Rakugi, H. & Isaka, Y.: Fetuin-mineral complex reflects extraosseous calcification stress in CKD. *Journal of the American Society of Nephrology* 21, 1998–2007 (2010).

Acknowledgements

Ich möchte mich bei allen bedanken, die mich während meiner Promotion begleitet und unterstützt haben.

Mein besonderer Dank gilt Herrn Prof. Walter Richtering für das mir entgegengebrachte Vertrauen, seine Unterstützung, konstruktive wissenschaftliche Diskussionen und das kritische Lesen meiner Arbeit. Vielen Dank, dass ich sowohl national als auch international an verschiedenen wissenschaftlichen Konferenzen und Workshops teilnehmen konnte.

Weiterhin danke ich Herrn Prof. Willi Jahnen-Dechent für die gute Kooperation, seine Offenheit, seine stete Unterstützung und die Begutachtung dieser Arbeit.

Außerdem bedanke ich mich bei den aktuellen und ehemaligen Mitgliedern meines Arbeitskreises für die Hilfsbereitschaft, zahlreiche Diskussionen und die ein oder andere Ablenkung zwischendurch. Ein ganz großer Dank geht an Janine, die das Durchhalten auf vielfältige Weise jeden Tag sehr viel leichter gemacht hat! Danke an Andreas, insbesondere für viele wissenschaftliche Hilfestellungen und seine fachliche und moralische Unterstützung während der Messzeiten. Ich bedanke mich bei Thomas, von dem ich gerade am Anfang so einiges über Streuung gelernt habe. Vielen Dank an Ralph, der nicht nur bei der Wasseranlage das ein oder andere Mal helfend einspringen musste. Außerdem danke ich Herrn Huppertz für seine Hilfe, die unterschiedlichsten Geräte wieder in Gang zu setzen. Ein Dankeschön geht auch an die restlichen Mitglieder des IPCs, ohne deren Unterstützung manches deutlich schwieriger gewesen wäre.

Vielen Dank an Steffen, der mich mit Probenmaterial versorgt, meine Ideen kritisch hinterfragt und mir oftmals ganz spontan bei der Umsetzung meiner Ideen geholfen hat. Ich bedanke mich außerdem bei Willis Mädels, die mich immer herzlich in ihrem Labor aufgenommen haben und mir durch ihre hilfsbereite Art so manches erleichtert haben. Ein besonderer Dank geht an Anne, Marietta und Laura sowohl für die fachlichen Diskussionen, aber natürlich auch für die kurzweilige Zeit während der Gordon Konferenzen.

Weiterhin möchte ich mich beim AK Klemradt für die Kooperation bedanken. Vielen Dank an Olivier und Mark für die Zusammenarbeit insbesondere während der Messzeiten. Olivier danke ich besonders für sein riesiges Engagement während seiner Masterandenzeit und für viele kurzweilige, fachliche und nicht-fachliche Diskussionen insbesondere während endloser Stunden im Zug oder an der Beamline.

Thanks to Clement Blanchet (EMBL) for his support during beamtime and especially for his great help in data analysis and interpretation. Thanks for the rapid answers to all my (partially weird) questions.

Vielen Dank auch an alle, die mich durch das Korrekturlesen meiner Arbeit unterstützt haben.

Ein großer Dank geht natürlich an meine Mädels „aus Lautern“ und aus dem Taunus, die immer ein offenes Ohr für mich haben und mich während der Promotionszeit - jede auf ihre ganz eigene Art - immer unterstützt und, wenn nötig, abgelenkt haben.

Zu guter Letzt möchte ich mich herzlich bei meiner Familie bedanken, die mich immer unterstützt und an mich geglaubt hat und mich immer wieder ermutigt hat, auch wenn es mal nicht so gut lief. Ganz besonders danke ich meinem Freund Gereon, der in den letzten Jahren immer für mich da war und mich auch in kritischen Phasen ertragen und stets ermutigt hat - DANKE dafür!

Curriculum Vitae

PERSONAL DETAILS

JOHANNA WALD

Diplom-Biophysikerin

* 18. August 1985, Wiesbaden

Nationality: German

Family status: Single

EDUCATION

11/2009 - today PhD Student, RWTH Aachen University, supervisor: Prof. Dr. W. Richtering

09/2009 Diploma in Biophysics

12/2008 - 09/2009 Diploma Thesis, TU Kaiserslautern, supervisor: Prof. Dr. C. Ziegler

11/2004 - 09/2009 Diploma Studies in Biophysics, TU Kaiserslautern

06/2004 General Qualification for University Entrance (Abitur)

08/1995 - 06/2004 Christian-Wirth-Schule (Secondary School), Usingen